

ACOUSTIC GONIOMETRY: A SPATIO-TEMPORAL APPROACH

THÈSE N° 2408 (2001)

PRÉSENTÉE AU DÉPARTEMENT D'ÉLECTRICITÉ

ÉCOLE POLYTECHNIQUE FÉDÉRALE DE LAUSANNE

POUR L'OBTENTION DU GRADE DE DOCTEUR ÈS SCIENCES TECHNIQUES

PAR

Eric VAN LANCKER

Ingénieur civil électricien, Faculté Polytechnique de Mons, Belgique
de nationalité belge

acceptée sur proposition du jury:

Prof. M. Rossi, directeur de thèse
Prof. S. Prasad, rapporteur
M. R. Joannes, rapporteur
Prof. Ph. Robert, rapporteur
Dr J.-P. Thiran, rapporteur

Lausanne, EPFL
2002

Abstract

This work was motivated by the increasing need for acoustic localization systems. The various localization systems that were implemented during this PhD include localization of snow avalanches, artillery and supersonic aircraft in the infrasound domain, the localization of helicopters, civilian aircraft, speakers and auditorium reflections in the audio domain and the localization of chirps in the underwater ultrasound domain.

The “*goniometer*” is defined as an instrument that measures angles. An “*acoustic goniometer*” is therefore a system that measures the direction of arrival (DOA) of sounds, and thus estimates the source direction. A goniometer is made up of an antenna, composed of several sensors arranged in a particular geometry, and a calculation algorithm.

The successive implementations were designed around a common framework, based on a two-step spatio-temporal process. The temporal step tackles the problem of the Time Delay Estimation along the antenna baselines, whereas the second step introduces the antenna geometry, in order to estimate the Direction of Arrival *per se*. The multi-sources case, as well as the outlier’s rejection, is assured by a detection module, which uses the temporal and spatial properties of the propagation model. The performances of the TDE and the localization are studied as a function of every relevant parameter, in order to determine the optimal antenna to run the two-step process. The antenna design rules concern its geometry, its size and its orientation.

The results presented in the applications chapter give a realistic idea of the goniometry capacities. Its performances are largely competitive to those of other techniques. Up to now, the goniometry developed during this work, fulfilled all prior requirements. Moreover, the goniometry appeared to be, in many cases, in advance with regards to technological tools such as the sound pick-up, the CPU implementation or installation constraints.

The advice that could be given, when tackling a new antenna design, is firstly to visualize both spatial and temporal properties of the propagating waves and of the perturbing phenomena, and secondly to compare them to the goniometer characteristics.

This work has demonstrated that the best performances were achieved for the goniometry of a unique stationary compact source generating broadband low pass signals in a homogenous medium without wind and noise, performed with a wide symmetrical broad-side antenna.

Version abrégée

La demande croissante en systèmes de localisation acoustique est la motivation première de ce travail. Le large éventail de systèmes de localisation qui ont été réalisés durant la thèse, a permis de mener à bien la localisation d'avalanches, de tirs d'artillerie et d'avions supersoniques dans le domaine infrasonore, la localisation d'hélicoptères, d'avions civils, de locuteurs et de réflexions dans le domaine audio et enfin la localisation de rampes en fréquence dans le domaine aquatique ultrasonore.

Le « *goniomètre* » est un instrument qui mesure les angles. Par extension, un « *goniomètre acoustique* » est un système qui mesure la direction d'arrivée (DOA) des sons, et estime ainsi la direction de source. Le goniomètre se compose d'une antenne, constituée de plusieurs capteurs disposés dans une géométrie donnée, et d'un algorithme de calcul.

Les réalisations successives ont été développées autour d'un support commun, basé sur un processus spatio-temporel implémenté en deux étapes. L'étape temporelle traite le problème de l'estimation des différences de temps de propagation entre capteurs, tandis que la deuxième étape estime la direction d'arrivée en utilisant les propriétés spatiales de l'antenne. Un module de détection permet de gérer plusieurs sources en même temps, ainsi que de rejeter les observations aberrantes. Il utilise pour cela les propriétés temporelles et spatiales de l'antenne ainsi que du modèle de propagation.

Les performances de l'estimation des délais et de la localisation sont étudiées en fonction de chacun des paramètres significatifs, afin de déterminer l'antenne optimale couplée à l'algorithme proposé. Les règles de conception de l'antenne concernent sa géométrie, sa taille et son orientation.

Les résultats présentés dans le chapitre des applications donnent une idée réaliste des capacités de la goniométrie. Ses performances sont très concurrentielles par rapport aux autres techniques. Jusqu'ici, les goniomètres, développés pendant ce travail, ont toujours rempli leurs cahiers des charges.

Dans bien des cas, il est apparu que la goniométrie était en avance sur les autres technologies qui l'accompagnent, telles que la prise de son et l'implémentation des algorithmes et par rapport aux contraintes d'installation.

La démarche à suivre lors de la conception d'une nouvelle antenne, consiste premièrement, à bien visualiser les propriétés spatiales et temporelles des ondes de propagation et des perturbations, et deuxièmement, de les comparer aux caractéristiques du goniomètre.

Ce travail a démontré que la goniométrie offrait des performances optimales dans le cas de la localisation d'une seule source compacte, immobile, émettant des sons passe-bas large-bandes, dans un milieu homogène, sans bruit ni vent, au moyen d'une antenne symétrique, de grande dimension et orientée en configuration Broad-side.

Table of contents

1.1	Formulation of the problem	3
1.2	Background	4
1.2.1	Beamforming techniques	4
1.2.2	Subspace-based method direction finding.....	6
1.3	A two-step approach	7
2.1	Propagation model.....	9
2.2	Antenna	10
2.3	Conditioning module.....	12
2.4	Time delay estimators.....	13
2.4.1	Classical Cross-correlation.....	13
2.4.2	Generalized Cross-correlation.....	15
2.4.3	Correlator implementation	19
2.5	Localization.....	22
2.5.1	Wave vector and Direction of Arrival	22
2.5.2	Closed-form solution	24
2.6	Detection.....	25
2.6.1	Peak-picking step	25
2.6.2	Peaks recombination.....	25
2.6.3	Delay set validation.....	30
2.7	Extra modules.....	30
2.7.1	Integration in the goniometer design	30
2.7.2	Waking up module	30
2.7.3	Event build up.....	32
2.7.4	Classification	33
3.1	Detection & precision: overview of the sensitive parameters.....	34
3.2	TDE Performance.....	36
3.2.1	Emission – reception: signal characterization	36
3.2.2	Performance indexes.....	37
3.2.3	Cramer-Rao Lower Bound, anomalies and ambiguities	37
3.2.4	Correlators comparison and enhancement.....	39
3.2.5	Transmission: wave propagation influence.....	39
3.2.6	Wind effect on the SNR and coherence	43
3.3	Localization performance	47
3.3.1	Two sensor goniometry: influence of parameters	47
3.3.2	Antenna geometry and localization errors	50
3.3.3	Influence of the speed of sound estimation	51
3.3.4	Influence of the sensors position estimation	51
3.3.5	Influence of the Time Delay Estimation	52

3.3.6 Plane wave assumption.....	53
4.1 Beamforming - DOA approaches	60
4.2 Sensor number	60
4.3 Inter-sensors spacing.....	61
4.4 Antenna geometry	65
5.1 Preamble	68
5.2 Infrasound goniometry.....	68
5.2.1 Background	68
5.2.2 Foreground	69
5.2.3 Avalanche activity monitoring	71
5.2.4 Infrasound Monitoring.....	75
5.3 Goniometry for outdoor active noise control	76
5.3.1 Problem definition and background	76
5.3.2 Foreground	77
5.3.3 Signal extraction by spatial filtering	80
5.4 Spatial Echogram.....	82
5.4.1 Problem definition.....	82
5.4.2 Solution proposed	82
5.5 Underwater ultrasound localization.....	87
5.5.1 Problem definition.....	87
5.5.2 Foreground	87
7.1 CRLB.....	94
7.2 CPE (Ianniello)	95
7.3 Norm criterion in spatial domain	96
7.4 Speed of sound influence on 3D - DOA	97
7.5 Array performance indexes [4].....	98

Chapter 1

Introduction

1.1 Formulation of the problem

This work was motivated by the increasing need for acoustic localization systems. The various localization systems that were implemented during this PhD include localization of snow avalanches, artillery and supersonic aircraft in the infrasound domain, the localization of helicopters, civilian aircraft, speakers and hall reflections in the audio domain and the localization of chirps in the underwater ultrasound domain.

The “*goniometer*” is defined as an instrument that measures angles. An “*acoustic goniometer*” is therefore a system that measures the direction of arrival (DOA) of a sound wave, and thus estimates the source direction.

An acoustic goniometer is made up of an array of microphones, called antenna, arranged in a particular geometry, and a calculation algorithm. According to the classical definitions, *active* goniometry is used when the signal source is under control, while *passive* goniometry refers to the localization of unknown sources called noise sources. The basic goniometer design is established according to the application and adaptation of the Radar and Sonar techniques that have been extensively developed during the last century. Although Radar refers to electromagnetic waves and Sonar to the underwater acoustic equivalent, both deals with the problem of echo detection and estimation of the directions of arrival of signals impinging on an array of sensors.

However, the diversity of the applications implies specific designs. The operational context summarizes the relevant properties necessary to complete the goniometer design. For example, the medium is characterized by its acoustic properties and background noise, and the sound source is defined by its signal properties: type, spectrum and level. The distance separating the source from the

antenna (source range) relative to the antenna extension determines the propagation properties to consider: planar propagation for far sources, spherical propagation for close sources. If the source is inside the antenna, another approach is considered (referred to as Distributed Array).

When the acoustic source is moving, many aspects have to be considered: the analysis rate and the analysis window length can represent critical choices for reasonable source position updating. The configuration can involve one or several sources. The propagation can introduce multi-path distortion such as reverberation, which is equivalent to having many delayed replicas of the same acoustic event, generated in different places in space.

The approach chosen was to develop a basic goniometer that could handle each application. This simple starting point is then enhanced to obtain the most efficient localization system in relation to a given application.

The goal of this section is to give an overview of the different techniques that have been developed for source localization. Early systems were based on the conventional Delay & Sum beamforming algorithm, enhancements were introduced by the Filter & Sum algorithm, and finally by the Optimum beamforming. Then Sub-Spaced direction finding methods were introduced as Super-Resolution techniques. After the description of the advantages and limitations of the different methods, a two-step localization approach will be proposed in relation to the applications considered. A full description of the methods presented in section 1.2 can be found in the books [51] [55], [58] and [110].

1.2 *Background*

1.2.1 Beamforming techniques

The term beamforming is used to describe the ability of a system to perform a spatial filtering by “forming beams” in order to receive a signal radiating from a specific direction while attenuating signals from other locations. The basic idea is to “steer” the array in one direction and to calculate the output power. The steering locations, which result in maximum power, yield the DOA estimate. The pencil beam is obtained by forming a linear combination of the sensor outputs. The beamformer output y , function of the steering direction θ , is the weighted sum of the sensor output x_m

$$y_\theta[k] = \sum_{m=1}^M w_m(\theta) \cdot x_m[k] \tag{Eq 1.1}$$

where M is the sensor number, w_m is the complex weighting and k refers to the time index of the sampled signal. The overall block diagram of the beamformer is presented in Figure 1.1. Considering a source far from the array, the wave fronts are perpendicular to the direction of propagation referenced by the angle θ . Under this condition, the time delay of arrival between the sensors is a simple equation

relating the angle θ , the inter-element distance d and the speed of sound c . After being picked up and conditioned, the signals are digitized and introduced into the beamforming algorithm.

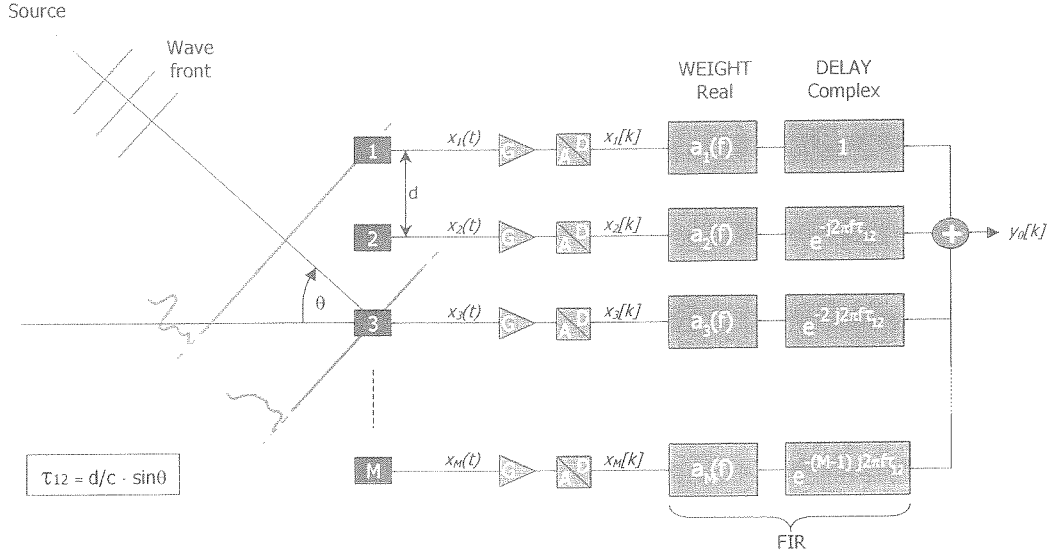


Figure 1.1 : Filter & Sum beamformer

In the basic case of a Uniform Linear Array (ULA) represented in Figure 1.2 (3-D space), the focalization in the direction θ is obtained by introducing the beamformer weightings

$$w_m(\theta) = a_m \cdot e^{j(m-1)\omega \frac{d}{c} \sin(\theta)}, \quad m \in [1..M] \quad \text{Eq 1.2}$$

where the complex weight appears as a phase term multiplied by the amplitude weights a_m . The sensor outputs are thus delayed in such a way that the signals impinging from the focalization direction given by θ are summed constructively (signals in phase) although the components coming from other directions are summed destructively (statically random phase). In the Delay & Sum algorithm, the amplitude weights are set to unity, while in the Filter & Sum algorithm, the weights are chosen to enhance the beamshape and reduce sidelobe levels. For example, the Dolph-Tchebyshev weighting forces the maximum level of the sidelobe as presented in Figure 1.3.

In order to increase the spatial filtering performances, the “Optimum beamformer” takes advantage of *a priori* information. According to the minimization cost function, the weighting vector is based on the reference signal (when the desired signal is known), on the SNR (when both signal and noise are known). If the locations of competing sources are known, a Multiple Sidelobe Canceller (MSC) is implemented to eliminate the unwanted contributions.

The “Adaptive beamforming” arrays uses weight vector adaptation algorithms such as the Least Mean Square (LMS) or the Recursive Mean Square (RLS) to converge on the optimal weight vector. These techniques are useful when there are a few discrete noise source directions that account for the acoustic interference.

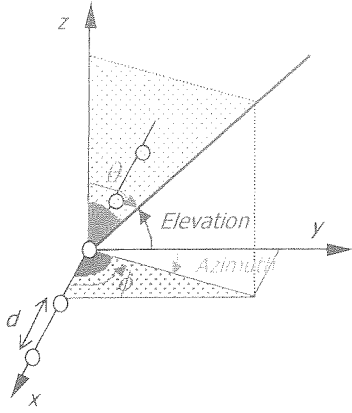


Figure 1.2 : Uniform Linear Array of five microphones with inter-element spacing d ; the steering direction is referenced by the angles (θ, ϕ) or the angles (Azimuth, Elevation)

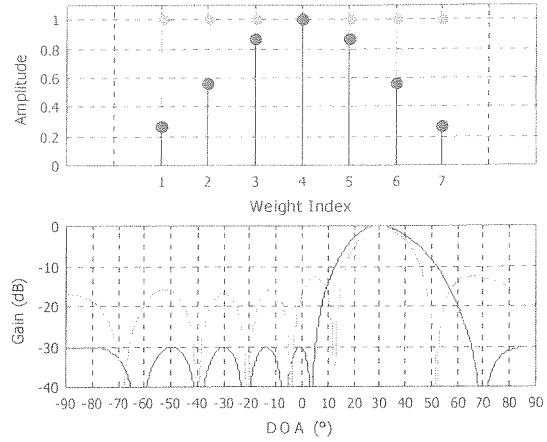


Figure 1.3 : Amplitude weight, Array response steered in the direction $\theta=30^\circ$ in case of Rectangular weighting (Delay & Sum algorithm : gray line) and Dolph-Tchebyshev (Filter & Sum algorithm : black line)

The “Matched Field beamforming” takes into account the spatial inhomogeneities and medium’s variation inducing each sensor to pick up different propagation directions and speed. The beamformer matches the measured field at the array, with replicas of the expected field for all sources locations. The replicas are determined by modeling the acoustic propagation for each sensor.

The general philosophy of beamforming techniques is to scan the space with an adequate spatial filtering in order to build the beamformer output map and to determine the DOA corresponding to its maxima. This processing is CPU costly and yields useless information in many applications. Another inconvenience is that the beamformers require array sizes that are comparable to the acoustic wavelength, as the method intrinsically implies a narrow band approach. These techniques are thus not adapted for large band signals (maximum band = 1 octave). Reasonable spatial resolution, related to the array aperture, is obtained to the detriment of the number of sensors. Solutions with hundreds of sensors are common. Yet, the advantages of the beamformer are that the theory is well known (extensive literature) and that dedicated DSPs can be found.

1.2.2 Subspace-based method direction finding

A second approach deals with the Subspace-based direction finding methods. These high-resolution methods are based on the calculation of the spatial covariance matrix given by

$$\hat{R} = \sum_{k=1}^K \bar{x}(k) \cdot \bar{x}^H(k) / K \quad \text{Eq 1.3}$$

where \bar{x} is the spatial signal vector composed of the samples recorded at the M sensors, k is the index of the snapshot and K is the number of snapshot considered. In the case of the *minimum variance* optimization algorithm, the principle is to find the DOA (ϕ, θ) that maximizes the array output power

$$P_{mv}(\phi, \theta) = \frac{1}{a^H(\phi, \theta) \cdot R^{-1} \cdot a(\phi, \theta)} \quad \text{Eq 1.4}$$

where a is the steering vector. This second order Statistics-Based method is purely spatial. Results are updated for each new sample. The signal to noise ratio is improved by performing a mean on the K snapshots of the frame. An initial estimation of the number of sources present is required.

Distinction is made between signal Sub-Space methods (Minimum Variance, Autoregressive, Subspace fitting, ESPRIT) and noise Sub-Space methods (Pisarenko, Music, Eigenvector). The main advantage of the subspace methods is the resolution. The drawbacks are those of a spatial approach. The spatial covariance matrix is calculated on a snapshot of the acoustic field at the array, thus the sensor number is critical to extract the information and to cover the working frequency band. The minimization of the array output power requires a 2D scanning in the case of a unique source. In a multi-sources configuration, the dimension of the space to scan is multiplied by the *a priori* number of sources increasing drastically the CPU load.

1.3 A two-step approach

The motivation to study and develop a spatio-temporal approach is driven by the need to overcome the drawbacks of the previous method. The spatio-temporal process is carried out by a two-step procedure as presented in Figure 1.4.

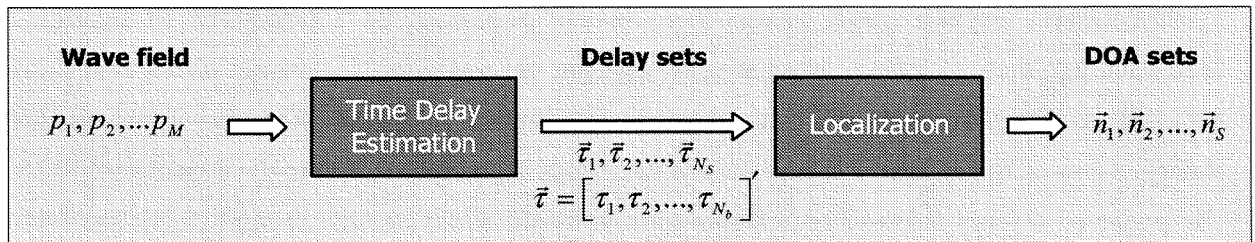


Figure 1.4 : Two-step procedure

The first step considers the estimation of time delay between the sensors taken two by two. The delays calculated for the appropriate N_b baselines (sensor pairs) feed the localization algorithm, which determines the best DOA. The multi-sources configuration is handled by a recombination module, which reorganizes the delays along each baseline into N_s delay vector $[N_b \times 1]$ corresponding to each source. The time delay estimation is a temporal process as it is based on the generalized cross-correlation techniques. On the other hand, the localization module introduces the antenna geometry and size, the speed of sound and is a spatial process.

The first advantage of this method is that the temporal process allows handling broadband signals. Secondly, it will be shown that four sensors forming three baselines are sufficient to manage the localization. Furthermore, computations are restricted to the minimum, as the sources scan is achieved by a one-dimension peak-picking procedure on the N_b baselines.

The time delay estimation study takes advantage of recent developments. G. C. Carter has edited "*a collection of key contributions ... in this fast-moving field*" [17] which regroups articles covering most aspects of the TDE. The methods considered can be classified as classical methods, generalized methods (Roth, SCOT, PHAT, ML, CPSP), adaptive methods (LMS), and Higher-Order Statistics-Based methods (Bi-spectrum, Cross-cumulants, Hologram). The classical and generalized methods were chosen and will be described in Chapter 2.

The Least Mean Square (LMS) adaptive method consists in calculating a Finite Impulse Response filter that automatically adapts its coefficients to minimize the mean square difference between two inputs. The FIR filter introduces a delay opposite to that existing between the two inputs. In the ideal situation, the filter weight corresponding to the true delay would be unity and all the other weights would be zero [83]. This adaptive method was rejected because of updating constraints and CPU load.

The Higher-Order Statistics-Based methods are based on the hypothesis that the signals are non-Gaussian processes. The principle is that even Order cumulant of Gaussian noise vanish. Higher-Order Statistics-Based methods (the cross-correlation function is a second-order method) were implemented in the MATLAB toolbox HOSA. Yet, the frame length required is prohibitive for most of the applications.

The localization of close range sources is commonly performed by a hyperbolic fit algorithm. Successive iterations in a least mean squares gradient descent search converges to the best DOA ([70],[92]). In [7], Brandstein solves the far-field case by searching the DOA that minimizes the distance between the measured delays set and the delays set corresponding to the investigated DOA. The proposed method is based on a closed-form solution, which consists in multiplying the delay vector by the inverse of the relative position matrix and by the speed of sound. The inherent far-field assumption is then discussed in terms of localization errors (section 3.3).

The objective of Chapter 3 is to estimate the performances of the two-step localization procedure. The qualities and inconveniences of the method will be highlighted by listing every relevant parameters of the goniometry and by studying their influence on the performances. The Chapter 4 gives rules for the antenna design, by drawing the lesson from the performance study, in order to build the most adequate antenna in relation with the method. In Chapter 5, the various applications, which were tackled during this work, will be presented with the care to emphasize the specificities of each configuration.

Chapter 2

Goniometer Modules

2.1 Propagation model

As a first approach, the propagation model considers free field conditions where the source is reduced to a perfect point far from the observation location. These hypotheses are expressed by

$$e_s \ll r \quad \text{Eq 2.1}$$

where e_s is the source extension and r the range defined as the distance separating the source from the observation location.

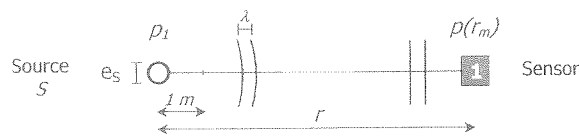


Figure 2.1 : Propagation model

For a propagating wave of constant frequency, the complex acoustic pressure waveform function $\underline{p}(r_m)$, observed at the sensor m , can be expressed as the source pressure \underline{p}_1 (defined at 1 m) divided by the range and multiplied by a propagation term ([51],[75]).

$$\underline{p}(r_m) = \frac{\underline{p}_1}{r_m} \cdot e^{-j(k_m \cdot r_m)} \quad \text{Eq 2.2}$$

where r_m is the range from the source, and k is the wavenumber. The equation Eq 2.2 can be interpreted as a spherical wave propagating outwards from the source (origin) calculated at a distance r_m . Using the relationship $k^2 = \omega^2 / c^2$, the propagation term can be simplified to

$$\underline{p}(r_m) = \frac{p_1}{r_m} \cdot e^{-j\omega(r_m/c)} \quad \text{Eq 2.3}$$

where ω is the wave temporal pulsation. The signal wavelength λ is related to the spatial-pulsation (wavenumber) by $\lambda = 2\pi / |\vec{k}|$. Moreover, if the goniometer extension is sufficiently small in comparison with the source range, it can be assumed that the attenuation coefficient is constant across the antenna, inducing

$$\underline{p}(r_m) = \frac{p_1}{r} \cdot e^{-j\omega(r_m/c)} \quad \text{Eq 2.4}$$

The pressures observed by the different antenna sensors differ only by their phase term. The sensor signals are reduced to a copy of the source signal, delayed by their respective propagation time. Yet, as all future developments will be performed in the time domain, the temporal counterpart of the previous equation will be preferred. The acoustic pressure signal $p_m(t)$ measured at the sensor m is the replica of the source signal $p_s(t)$ delayed by the propagation time $\tau_m = r_m / c$.

$$p_m(t) = \frac{p_s(t - \tau_m)}{r} \quad \text{Eq 2.5}$$

To simplify notation, the next section introduces the signal $s(t)$ which is defined as the acoustic pressure signal generated at the source location.

2.2 Antenna

The sensor array can monitor the propagation waves by spatially sampling the wave field in different locations. Assuming the results of the previous section, the following case is considered: a perfect point source S emits an acoustic signal $s(t)$, as shown in Figure 2.2, and a remote sensor array (microphones or hydrophones) captures the impinging signal after a propagation time τ_i . This delay corresponds to the distance r_i from the source to the sensor i , divided by the speed of sound c . The signal $x_i(t)$ recorded can be modeled as the replica of the source signal delayed by the propagation τ_i , attenuated by a factor α_i and contaminated by the noise component $n_i(t)$. The expression is given for the sensor pair 12 by

$$\begin{aligned} x_1(t) &= \alpha_1 \cdot s(t - \tau_{s1}) + n_1(t) \\ x_2(t) &= \alpha_2 \cdot s(t - \tau_{s2}) + n_2(t) \end{aligned} \quad \text{Eq 2.6}$$

The amplitude factor α_i takes into account the $1/r_i$ attenuation due to geometrical propagation, as predicted in Eq 2.4 (ideal case) and considers also the propagation loss due to medium absorption. The noise term refers to any component signal that is not generated by the source being considered. It can be separated into the sum of three terms

$$n(t) = n_I(t) + n_C(t) + n_R(t) \quad \text{Eq 2.7}$$

where $n_I(t)$ is the background noise, $n_C(t)$ is the interfering noise due to competing sources and $n_R(t)$ is “reflected” noise due to the arrival of indirect sounds. The first term corresponds to an incoherent noise (no spatial correlation), it can be produced by electronic noise or induced wind noise and can be statistically attenuated by adequate processing. The last two terms require due care to be taken because they generate coherent signals at the array sensors.

The difference of propagation time between the sensors 1 and 2 is defined by

$$\tau_{12} = \tau_{s2} - \tau_{s1} = \frac{\Delta r}{c} \quad \text{Eq 2.8}$$

where τ_{12} is named Time Delay of Arrival (TDOA) and $\Delta r = r_2 - r_1$ is the path length difference.

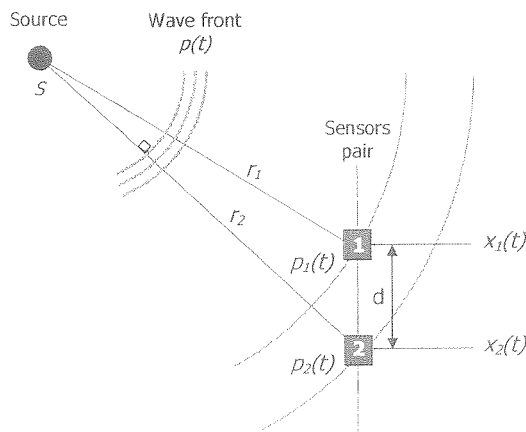


Figure 2.2 : Propagation model of the source wave - 2 sensors configuration

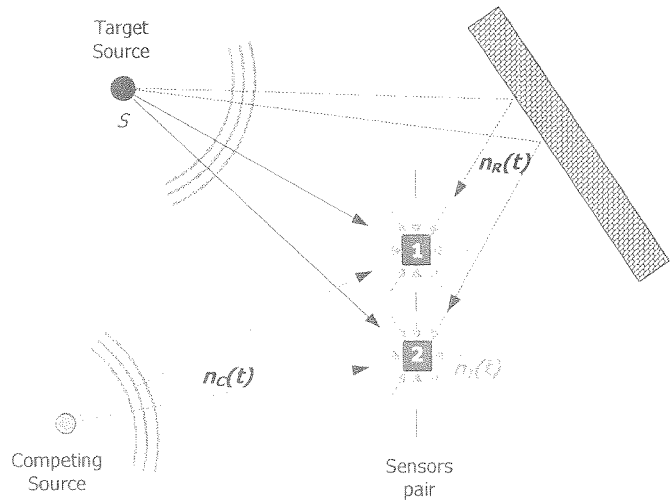


Figure 2.3 : Noise components

The antenna design, as well as the microphone choice or conception will be discussed in Chapter 4. As a first approach, the transducers are supposed to present flat responses over the bandwidth, to be paired in phase, to present perfectly omnidirectional directivity diagrams and to be sufficiently small with regard to the wavelength so as to avoid modifying the wave field.

2.3 Conditioning module

As the goniometry is carried out by calculating the TDOA between sensors, special care has to be taken with the phase when acquiring the signals. The different channels have to be paired in phase. Although amplitude disparities of a few dB do not have important consequences on the TDE, a difference of a few degrees in phase can cause DOA estimation errors of a few degrees.

The microphones will be chosen for their phase properties and their pairing. A flat amplitude response foreshadows phase responses without accidents. Smooth evolution of the phase will thus be preferred.

The amplification step is designed to bring the signal level up to the dynamic range of the A/D converter. In principle, the phase disparities between channels are an order of magnitude below those introduced by the microphones. Nevertheless, saturation can induce non-linearity and serious degradation in the goniometry. Indeed, the time delay estimation process is very sensitive to the coherence between the signals.

As well as the role of anti-aliasing filter, the filtering step is used to enhance the signal SNR. *A priori* information enables us to design a filter that attenuates the low SNR frequency bands. For example, a high pass filter will be used to reduce $1/f$ noise ($f_{-3dB} = 20$ Hz for audio applications). The signal level is thus reduced and the A/D dynamic range is adequately used to quantify highly relevant frequency band. Elliptic low-pass filters (8th Order, $f_{-3dB} = 0.45 F_s$) are widely used as anti-aliasing filters [58]. The phase disparities of the filters are mainly related to the precision of the electronic components and their drift with temperature.

The analog to digital conversion is performed either by multiple sigma/delta converters, synchronized by a single clock or by a unique high-speed converter with a multiplexer. Although the sigma/delta introduces a delay (approximately a fixed number of samples), the pairing is maintained when identical devices are used. To the contrary, the multiplexed converter induces a delay between channels as a unique converter processes the channels sequentially. This delay, called *skew*, can be compensated by software.

According to the frequency domain being considered, different technologies are involved. Professional audio (ADAT, Studer, Sonosax, Sony) , semi-professional (Frontier Design, RME, Turtle Beach) , data acquisition board (National Instrument) and home-made technologies were used to perform the conditioning. Au contraire

2.4 Time delay estimators

2.4.1 Classical Cross-correlation

A common method to determine the TDOA is to compute as a function of the delay τ , the cross-correlation function given by¹

$$R_{12}(\tau) = E \left[x_1(t) x_2(t-\tau) \right] = \int_{-\infty}^{\infty} x_1(t) x_2(t-\tau) dt \quad \text{Eq 2.9}$$

where $E[\cdot]$ denotes the expectation. The cross-correlation exhibits, for a given delay of propagation, how well the waveform $x_1(t)$ fits to $x_2(t-\tau)$. Thus, the delay that maximizes the cross-correlation corresponds to the expected TDOA τ_{12} .

In practice, the Time-domain cross-correlation function is computed from the cross-spectral density function using the inverse Fourier transform by the Wiener-Khintchine equality

$$R_{12}(\tau) = \int_{-\infty}^{\infty} G_{12}(f) e^{j2\pi f\tau} df \quad \text{Eq 2.10}$$

where $G_{12}(f)$ is the Cross-Power Spectral Density function (CSD). However, due to the finite observation time, Eq 2.10 can only be estimated for a given temporal window and becomes

$$\hat{R}_{12}(\tau) = \frac{1}{T} \int_0^T x_1(t) x_2(t-\tau) dt \quad \text{Eq 2.11}$$

where T is the observation time and the $(\hat{\cdot})$ superscript indicates an estimate. The value of T depends on the application. For example, in the presence of moving sources, the observation time will be chosen in such a way that the source has not moved “too much”, so that the hypothesis of a stationary process is satisfied. In such a case (still sources, constant propagation conditions), long sequences can be handled with respect to the hardware constraints (memory, refreshing rate).

Yet, the integration over a finite observation time has an undesirable effect: the cross-correlation presents a bias with the delay. Considering the sensor pair output 12, the finite length signals $x_i^w(t)$ $i=1,2$ can be written as the multiplication of the signal $x_i(t)$ by the rectangular weighting windows $w_R(t)$, the length of which corresponds to the desired observation time T

$$x_1^w(t) = x_1(t) \cdot w_R(t) \quad x_2^w(t) = x_2(t) \cdot w_R(t) \quad \text{Eq 2.12}$$

where $x_i^w(t)$ is the windowed version of $x_i(t)$. Thus the finite length estimation of the cross-correlation can be written as

¹ In the interest of clarity, the correlation formulation will be written in the continuous domain

$$\begin{aligned}
\hat{R}_{12}(\tau) &= E[x_1^w(t) x_2^w(t-\tau)] \\
&= E[x_1(t) w_R(t) x_2(t-\tau) w_R(t-\tau)] \\
&= E[x_1(t) x_2(t-\tau)] \cdot E[w_R(t) w_R(t-\tau)] \\
&= R_{12}(\tau) \cdot R_{ww}(\tau)
\end{aligned}
\tag{Eq 2.13}$$

where $R_{ww}(\tau)$ is the auto-correlation function of the rectangular window and is a triangular window centered at $\tau=0$. As R_{ww} is a function of τ , the finite length cross-correlation is biased. As expressed in Eq 2.13, the unbiased cross-correlation can be obtained by dividing the finite length cross-correlation by the window auto-correlation function. To explicit this relation, Figure 2.4 presents the case of two signals weighted by a 50 ms length rectangular window. The signal $x_2(t)$ is a Gaussian zero-mean white noise and $x_1(t)$ is chosen as the sum of two replica of $x_2(t)$ delayed of 5 and 30 ms respectively. In the top-right graphic, the biased cross-correlation exhibits two peaks of different energies. The window auto-correlation function represented by the triangular function can be seen as an envelope of the biased cross-correlation. When normalized by the triangular function, the amplitudes of the two cross-correlation peaks are equal as expected.

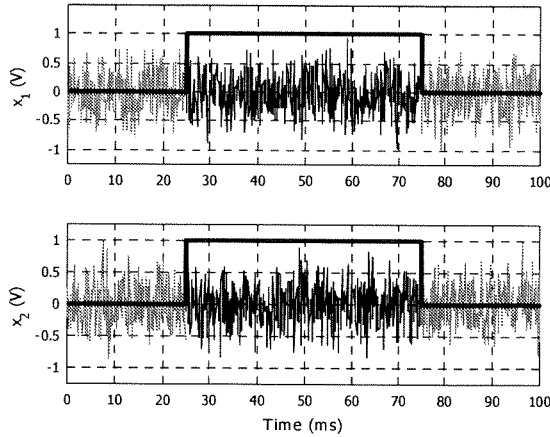


Figure 2.4 : Gaussian zero-mean white noises x_1 and x_2 weighted by a 50 ms rectangular window (centered at $t=50$ ms)

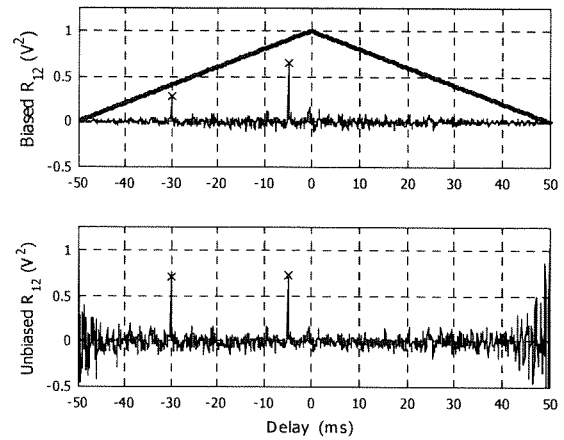


Figure 2.5 : Biased cross-correlation R_{12} and Normalized auto-correlation function of the rectangular window; Unbiased cross-correlation

In practice, the CSD function is estimated from the calculation of the spectra $X_1(f)$ and $X_2(f)$ through the Fourier Transform applied to windowed segment of $x_1(t)$ and $x_2(t)$ and is defined by

$$G_{12}(f) = X_1(f) \cdot X_2^*(f) \quad \text{with} \quad \begin{aligned} x_1(t) &\overset{F}{\leftrightarrow} X_1(f) \\ x_2(t) &\leftrightarrow X_2(f) \end{aligned}
\tag{Eq 2.14}$$

In order to understand how the delay information is extracted from the signals through successive calculations, the following simulation was performed. A Gaussian white noise signal was generated and low-pass filtered (Butterworth, 2nd order) to simulate the source emission. After duplication of this signal, the copy is delayed by 10 samples to simulate a TDOA of 1ms ($F_s = 10$ kHz) between the

two sensors. Then, the signals are corrupted by two different white noises to simulate additive incoherent noise according to the model presented in section 2.2. The amplitude of each contribution is chosen to obtain a SNR of 10dB. Figure 2.6 (top) exhibits the Power Spectral Density of each component. Two SNR regions are observed: below 2500 Hz, the SNR is positive and it becomes negative above 2500 Hz. Figure 2.7 presents the Cross-Power Spectral Density function. The amplitude informs us on the frequency bands of “coherent” energy between the two sensor signals. High CSD frequency bands are related to propagation across the antenna, as observed in the phase plot. Indeed, below 2.5 kHz, an almost linear behavior is observed. The delay can be directly obtained by calculating the “best” slope. In reality, a phase rotation ($\partial P=2\pi$) is accomplished between 500 and 1500 Hz ($\partial\omega=2\pi\cdot 10^3$), so that the TDOA is equal to $\partial P/\partial\omega=1$ ms, as confirmed by the cross-correlation. As the frequency increases, the SNR decreases and the phase linearity is degraded. Beyond 2.5 kHz, the SNR is so low that the phase becomes erratic.

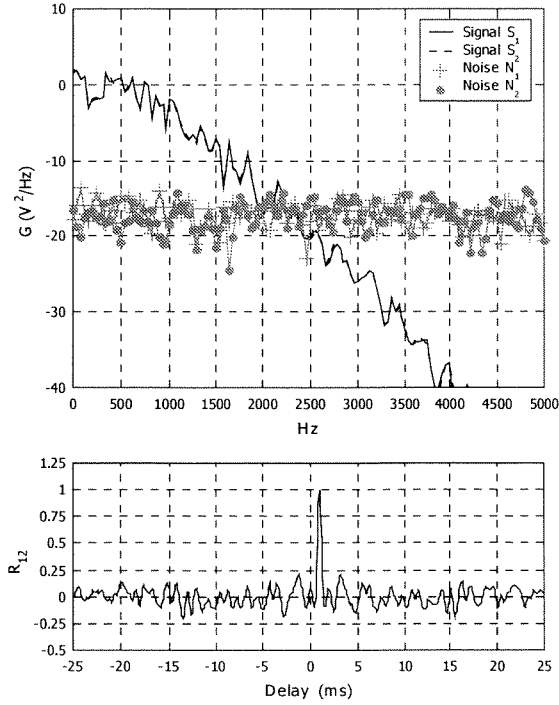


Figure 2.6 : Top - PSD of the different components;
Below – Normalized cross-correlation

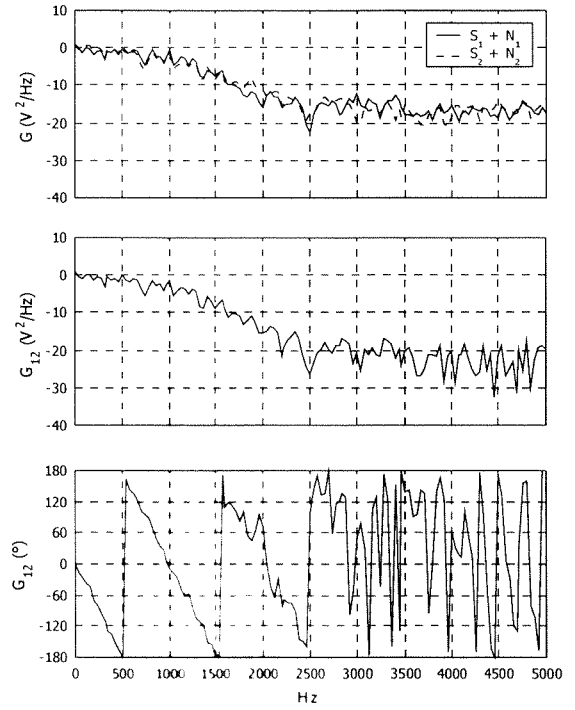


Figure 2.7 : Amplitude and phase of the cross-Power Spectral Density function

2.4.2 Generalized Cross-correlation

Generic formulation

To ensure a good time-delay resolution of the peak associated with the target source, the cross-correlation function can be “enhanced” by prefiltering the received waveforms. These techniques are included in the Generalized Cross-correlation methods [54]. In the time domain, prefiltering refers to the filtering of the input signal prior to delay, multiplication and integration. In the Fourier domain,

prefiltering is equivalent to applying a window or a weighting function to the CSD function. This leads to the generalized cross-correlation function, which is given by

$$R_{12}(\tau) = \int_{-\infty}^{\infty} \psi_g(f) G_{12}(f) e^{j2\pi f\tau} df \quad \text{Eq 2.15}$$

where ψ_g denotes an appropriately selected weighting function.

The estimated form is rewritten

$$\hat{R}_{12}(\tau) = \int_{-\infty}^{\infty} \psi_g(f) \hat{G}_{12}(f) e^{j2\pi f\tau} df \quad \text{Eq 2.16}$$

For the *basic cross-correlation processor* (no prefiltering), the weighting function is equal to unity for all frequencies.

SCOT transform

The *smoothed coherence transform* (SCOT) uses the weighting

$$\psi_s(f) = \frac{1}{\sqrt{G_{11}(f)G_{22}(f)}} \quad \text{Eq 2.17}$$

where $G_{11}(f)$ and $G_{22}(f)$ denote the power spectra of $x_1(t)$ and $x_2(t)$ respectively. The SCOT correlator can be interpreted as two pre-whitening filters and corresponds to the Fourier transform of the complex coherence. The signal spectrum term tends to de-emphasise very strong components such as tonals in broadband signals. Indeed, in the presence of strong tonals in $x_1(t)$ and $x_2(t)$, the cross-power density spectrum $G_{12}(f)$ exhibit Dirac function at the relevant frequencies and the normalization of these components by the power spectra reduces their weights. From the simulation presented in section 2.4.1, a sinus ($f = 250$ Hz) is added to the source signal. The classical cross-correlation exhibits a hazardous periodic behavior, the period of which corresponds to the pure tone (Figure 2.8). The induced ambiguities can cause an erroneous peak picking. In the same configuration, the SCOT correlator performs very well.

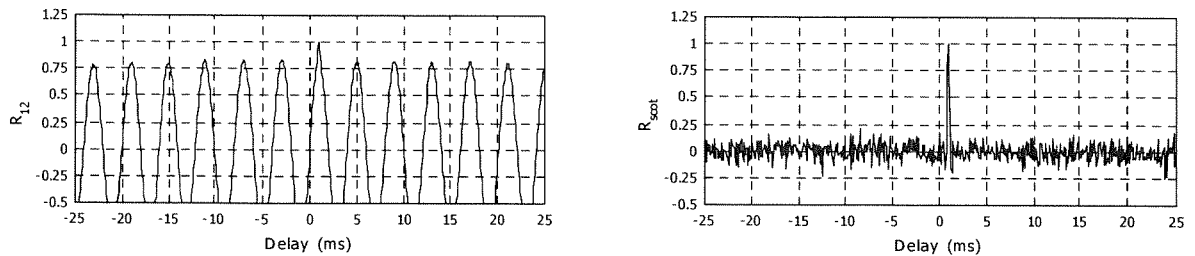


Figure 2.8 : Classical cross-correlation (Left) - SCOT correlator in the presence of a strong tonal ($f=250$ Hz)

Replacing Eq 2.17 in Eq 2.16, it appears that the SCOT correlator is the Fourier Transform of an estimation of the coherence function

$$R_{12}^S(\tau) = \int_{-\infty}^{\infty} \hat{\gamma}_{12}(f) e^{j2\pi f\tau} df \quad \text{Eq 2.18}$$

$$\hat{\gamma}_{12}(f) = \frac{\hat{G}_{12}(f)}{\sqrt{G_{11}(f)G_{22}(f)}} \quad \text{Eq 2.19}$$

where R_{12}^S is the SCOT correlation estimator and γ_{12} represents the complex coherence function.

PHAT transform - CPSP correlator

The *Phase transform processor (PHAT)* uses only the cross-spectral phase information for the Time delay estimation and corresponds to the weighting

$$\psi_p(f) = \frac{1}{|G_{12}(f)|} \quad \text{Eq 2.20}$$

The *PHAT* processor is an *ad hoc* method, indeed the generalized correlation becomes

$$R_{12}^P(\tau) = \int_{-\infty}^{\infty} \frac{\hat{G}_{12}(f)}{|G_{12}(f)|} e^{j2\pi f\tau} df \quad \text{Eq 2.21}$$

Under the theoretical assumption of uncorrelated noise signals $n_1(t)$ and $n_2(t)$, and in the ideal case $\hat{G}_{12}(f) = G_{12}(f)$, it follows that

$$R_{12}^P(\tau) = \int_{-\infty}^{\infty} e^{j2\pi f(\tau - \delta_{12})} df \quad \text{Eq 2.22}$$

and the generalized correlation is reduced to the Dirac function centered at the correct delay δ_{12} . It is worth noting that, contrary to both the classical and SCOT correlator, the PHAT correlator is independent from the input signal characteristics.

The generalized cross-correlator is estimated by the normalized Cross-Power Spectrum and is known as the Cross Power Spectrum Phase correlator [67]

$$R_{12}^{CPSP}(\tau) = \int_{-\infty}^{\infty} \frac{X_1(f) \cdot X_2^*(f)}{|X_1(f)| \cdot |X_2(f)|} e^{j2\pi f\tau} df \quad \text{Eq 2.23}$$

where $*$ denotes the complex conjugate.

As observed in Figure 2.9, the Phase correlator compensates the decrease in amplitude of the signal spectrum and presents a Dirac at the true delay as predicted in Eq 2.26. In the same configuration, the Classical Cross-correlation exhibits a very smooth and vague maximum.

Furthermore, the phase method performs very well when the source signal is white or broadband-limited, even in the presence of strong tonals. However, this method exhibits erratic behavior when the CSD is equal to zero in some frequency band (i.e., band limited signals) as the normalized CSD ψ_p .

$G_{12}(f)$ is undefined. Thus normalizing the CSD with its magnitude uniformly in the entire frequency range introduces artefacts in the cross-correlation and errors in the time delay estimation. Therefore, this behavior suggests that the phase weighting should be coupled by an extra term to compensate for the presence or absence of signal power.

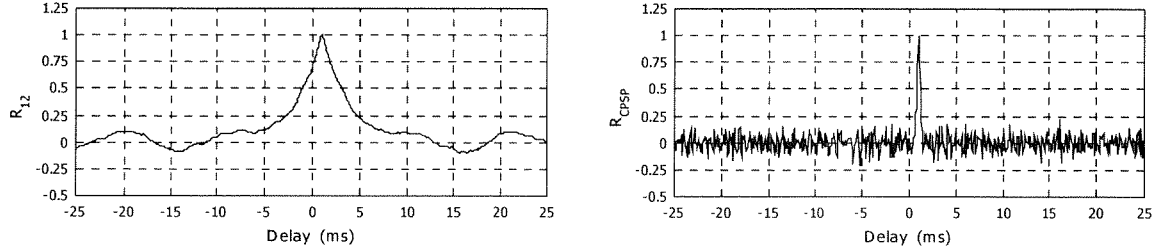


Figure 2.9 : Classical cross-correlation (Left) - CPSP correlation (Right) of a pink spectrum signal in the presence of white noise (SNR = 10dB)

ML correlator

The Maximum-Likelihood estimator, also called Hannan-Thomson processor, solves the *PHAT* drawback by weighting the normalized CSD by a coherence term. The ML weighting is given by

$$\psi_{ML}(f) = \frac{1}{|G_{12}(f)|} \cdot \frac{C_{12}(f)}{1 - C_{12}(f)} \quad \text{Eq 2.24}$$

and provides the maximum-likelihood estimate of the time delay under the assumption of band-limited random signals corrupted by white noise. The coherence term $C/(1-C)$ applies a greater weight to the phase in regions of the frequency domain that give near-unity coherence. The coherence term C_{12} is defined as the magnitude-squared coherence (MSC) and is given by

$$C_{12}(f) \equiv |\gamma_{12}(f)|^2, \quad 0 \leq C_{12} \leq 1, \quad \forall f$$

$$\gamma_{12}(f) = \frac{G_{12}(f)}{\sqrt{G_{11}(f) G_{22}(f)}} \quad \text{Eq 2.25}$$

Frequency bands without signals will present very low coherence and will be greatly attenuated. The coherence can be seen as a measure of the linear dependence between the two sensor signals [30].

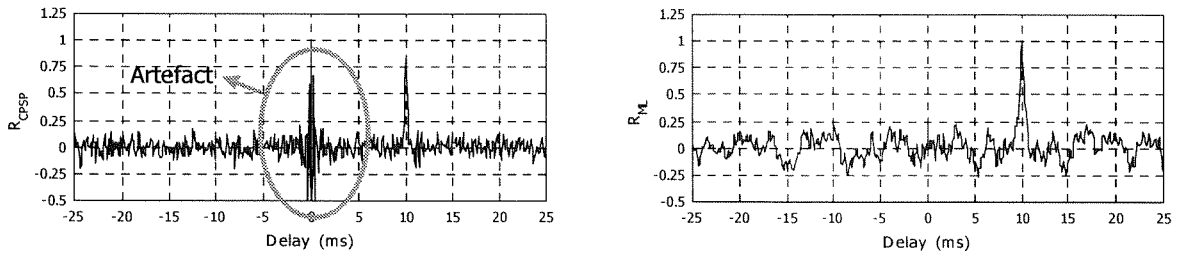


Figure 2.10 : CPSP correlation (Left) – ML correlation (Right) of a pink spectrum signal in the presence of white noise (SNR = 10dB) affected by a spectrum gap between 2.5 and 4.5 kHz

The comparison of the CPSP correlator and the ML correlator (Figure 2.10) displays the benefic effect of the coherence term to cancel the artefact introduced by the band-limited characteristics of the signals. Furthermore, the ML correlator is, by definition, the optimum Time Delay Estimator in the sense that the variance of its estimate reaches the absolute minimum variance (CRLB: *Cramer-Rao Lower Bound*) for long observation time. The demonstration can be found in [46].

Modified CPSP correlator

Another solution was presented by Omologo [69]

$$R_{12}^{CPSPm}(\tau) = \int_{-\infty}^{\infty} \frac{X_1(f) \cdot X_2^*(f)}{\left(|X_1(f)| \cdot |X_2(f)| \right)^\rho} e^{j2\pi f\tau} df \quad \text{Eq 2.26}$$

The basic idea is that frequency bands where the magnitude $|X(f)|$ is higher, will present greater SNR and more relevant information. Therefore, the whitening of the CSD is a partial normalization obtained by the introduction of ρ exponent. Setting ρ to zero produces unnormalized cross-correlation, while setting ρ to one produce the classical Cross-Power Spectrum Phase. Efficient values of ρ are mainly obtained by experimentation. When the operating SNR is poor and reverberation significant, ρ tends to be small. To the contrary, in "anechoic chamber" conditions, a ρ coefficient close to unity will emphasize phase information and will induce sharp correlation peaks and accurate TDE. An initial value of 0.75 is a good compromise.

Although sharp peaks enable precise time delay estimation, they are more sensitive to errors introduced by finite observation times and low SNR. Thus, the choice of ψ_g is a compromise between good resolution and stability.

2.4.3 Correlator implementation

Discrete formulation

The discrete counterpart of the continuous time domain Cross-correlation function (Eq 2.9) is given by

$$R_{12}[n] = \begin{cases} \sum_{k=0}^{K-|n|-1} x_1[k+1] \cdot x_2[k+n+1] & n \geq 0 \\ R_{21}[-n] & n < 0 \end{cases} \quad \text{Eq 2.27}$$

where $x_1[k]$, $k=1..K$ is a finite-length sequence from sensor 1. The time is related to the samples index by the relation $t=kFs$, $\tau=nFs$ and $T=KFs$. This formulation does not require any advanced signal processing functions. Moreover, the calculation can be restricted to an observation time window corresponding to the spatial window to be covered.

Yet, when the observation time increases, CPU constraints may be predominant as the processing time grows proportionally to K^2 . The frequency domain formulation may be preferred

$$R_{12}[n] = \text{Re} \left(F^{-1} \left(F(x_1[k]) \cdot F^*(x_2[k]) \right) \right) \quad \text{Eq 2.28}$$

where Φ refers to the Fast Fourier Transform and Φ^{-1} to the Inverse Fast Fourier Transform. Special care has to be taken when handling the FFT and IFFT calculation (one sample is truncated due to even FFT size although the spectrum is symmetrical).

The implementation of the generalized cross-correlation in the frequency domain approach is justified by the simplicity of the calculation. The different normalizations obtained by a straightforward division in the frequency domain would require to deconvolve the signals by the appropriate impulse response.

Sampling frequency and TDE resolution

The temporal resolution of the cross-correlation is defined as the minimum delay separating two distinct contributions. Theoretically, two sampling periods T_s are sufficient.

The first intuitive way to enhance the resolution of the cross-correlation would be to increase the sampling frequency. Yet, as no extra information is introduced in the process, the cross-correlation will only gain in precision but not in resolution.

Thus, the choice of the frequency sampling should only be determined by the signal spectrum. Referring to Shannon's sampling theorem (also called cardinal reconstruction formula), all information is conserved when sampling at $F_s \geq 2f_{max}$ (where f_{max} is the highest frequency of the signal).

Sub-sample precision

Yet, sub-sample precision is required in many cases to achieve the desired DOA precision. A first solution is to oversample the cross-correlation function. A second way is to enhance locally the precision in the vicinity of the maxima by a parabolic interpolation.

The oversampling operation can either be implemented in frequency domain (applied to the cross-power spectrum function) or in the time domain directly on the cross-correlation. In the frequency domain, the method consists in multiplying the sampling frequency by the required oversampling coefficient and to fill the spectrum with zeros up to half the new sampling frequency (zero-padding procedure). The inverse Fourier transform is applied to the resulting cross-power spectrum in order to obtain a cross-correlation function, the temporal sampling of which is reduced by the oversampling factor.

In the time domain, the oversampling is achieved by convoluting the cross-correlation by a SINC function. As the calculation becomes very tough with increasing oversampling coefficient, a truncated version of the SINC can be considered. The theoretically infinite length SINC can typically be reduced to 20 or 30 samples.

The parabolic interpolation is the easiest and fastest way to achieve the sub-sample precision. For example, the parabolic fitting by a 3-point interpolation method is given by

$$n_i = n - \frac{1}{2} \left[\frac{R_{12}[n+1] - R_{12}[n-1]}{R_{12}[n+1] - 2 \cdot R_{12}[n] + R_{12}[n-1]} \right] \quad \text{Eq 2.29}$$

where n is the index of the estimated delay, n_i is the index (non-integer) of the interpolated delay.

The parabolic fit approach was examined by R.E. Boucher and J.C. Hassab and has shown to be a biased estimator of the time delay [6], both bias and variance of the estimate depending on the location of the delay between the samples and the method used.

Smooth version of the correlator by incoherent processing

When the stationary conditions are fulfilled during several successive cross-correlation windows, a smoothed version of the correlator can be obtained by filtering (low pass). The new correlator is calculated as a weighted mean of the precedent cross-correlations as shown in

$$R_{12} = b(1) \cdot R_{12}^0 + b(2) \cdot R_{12}^{-1} + \dots + b(F) \cdot R_{12}^{-F+1} \quad \text{Eq 2.30}$$

where the exponent corresponds to the temporal index of the frame and F is the number of frames considered. The determination of the weightings is a FIR filter design problem. The result is a SNR enhancement. This method refers to incoherent processing as it operates on different frames. Practically, for memory and CPU constraints, a filter length of three is used (i.e. $b = [0.25 \ 0.5 \ 0.25]$).

Furthermore, Carter has shown in [17] that for a fixed amount of data, there is a trade-off between the frame length and number of independent segments available. The so-called "Weighted Overlap Segment Averaging (WOSA)" performs a temporal averaging of successive cross-correlation window in order to increase the TDE performances. The study conclusion proposes the use of a Hanning time weighting with a 50 to 62.5 % percent overlap.

Cross-correlation enhancement by coherent processing

The coherent processing consists in performing simultaneously the TDE along several equivalent baselines. Two baselines can be considered as equivalent if their spatial configurations (location and orientation) are sufficiently close from the source point of view. In such a case, the different cross-correlations can be superposed in order to deliver an enhanced average cross-correlation. For example, the coherent processing has been used in outdoor experiments for the localization of civilian airplanes (see application 5.3). Each TDE was estimated from the cross-correlation performed on the four parallel cube apexes. The peak was increased by 6 dB ($10 \cdot \log_{10}(4)$) relative to the incoherent background noise. The coherent processing has a remarkable action against the incoherent noise and on the local perturbations (different between sensors). Yet, this is to the detriment of the sensor number.

2.5 Localization

2.5.1 Wave vector and Direction of Arrival

The wave vector and Direction of Arrival (DOA) are describing the same information. They differ only by their point of view. The wave vector is related to the propagating wave and is pointing in the direction of propagation. The DOA is defined from the antenna point of view (*"Where does the sound come from?"*) and is opposite of the wave vector. They can be calculated from the TDOA by introducing the array geometry and the speed of sound.

Let us consider an array of M sensors located at the position $\{\vec{x}_m\}$, $m=1..M$ situated in a 2D coordinate system. The origin is chosen, for convenience, at the array's phase center defined by

$$\sum_{m=1}^M \vec{x}_m = 0 \quad \text{Eq 2.31}$$

In near-field source localization, as shown in Figure 2.11, each sensor sees the incident wave vector under a different angle.

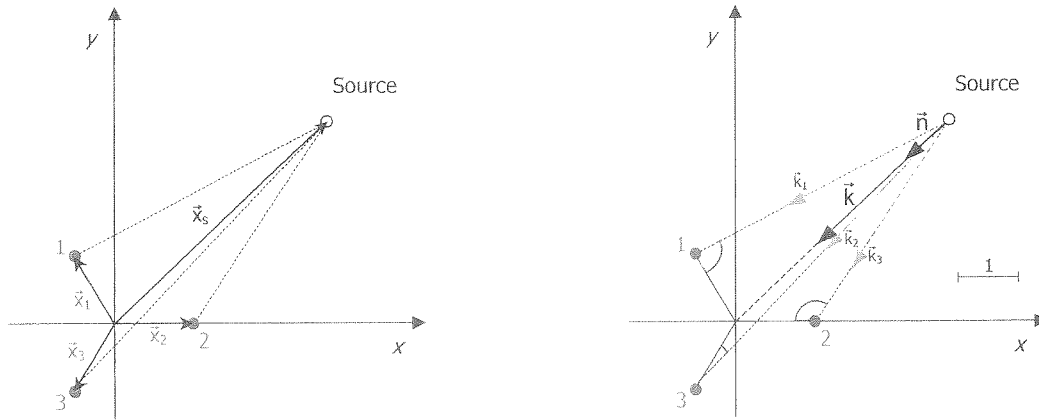


Figure 2.11 : Three-sensor antenna in the presence of a near source

If the amplitude variation across the array is neglected, the acoustic pressure observed at the sensor m can be written (see Eq 2.2)

$$p_m(t) = \frac{1}{r} \cdot p_s \left(t - \frac{\vec{k}_m \cdot \vec{x}_m}{\omega} \right) \quad \text{Eq 2.32}$$

where \vec{k}_m is the wavenumber vector that points from the source location to the sensor m .

In the far-field situation, the m wavenumber vectors tend to coincide with a unique array wavenumber vector \vec{k} pointing to the array's phase center (Figure 2.12). In this case, the propagation time τ_{sm} from the source to the sensor is therefore equal to

$$\tau_{sm} = \frac{\vec{k} \cdot \vec{x}_m}{\omega} \quad \text{Eq 2.33}$$

Considering the sensor pairs 12, the relation between the wave vector containing the DOA information and the TDOA can be estimated from section 2.4 by

$$\tau_{12} = \tau_{s2} - \tau_{s1} = \frac{\vec{k} \cdot (\vec{x}_2 - \vec{x}_1)}{\omega} = \frac{\vec{k} \cdot \vec{x}_{12}}{\omega} \quad \text{Eq 2.34}$$

By introducing the normalized vector

$$\vec{n} = \frac{\vec{k}}{|\vec{k}|}, \quad k = \frac{\omega}{c} \quad \text{Eq 2.35}$$

the TDOA from sensor 1 to sensor 2 is simplified to the dot product of the normalized wave vector and the relative position vector of the sensors scaled by the speed of sound as expressed in

$$\tau_{12} = \frac{1}{c} \vec{n} \cdot \vec{x}_{12} \quad \text{Eq 2.36}$$

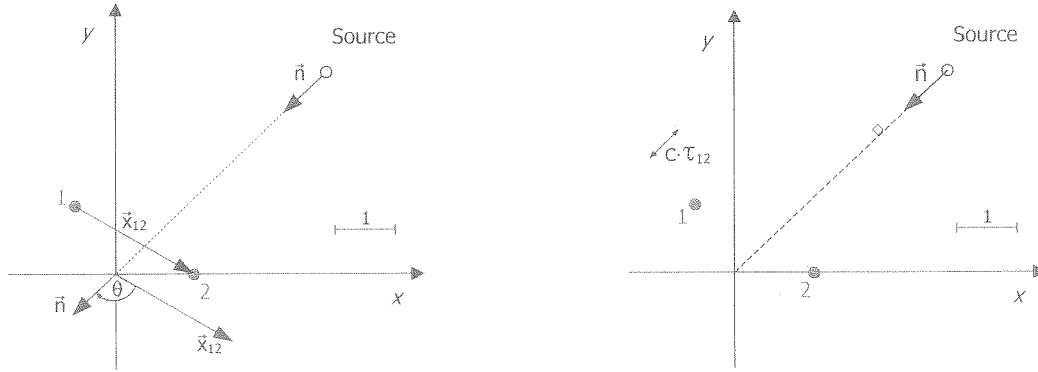


Figure 2.12 : Wave vector , relative position vector and time delay of a far source

Considering N_b different baselines (sensor pairs) adequately chosen in the $M(M-1)/2$ possibilities, the set of equations

$$\begin{cases} \dots \\ \tau_{ij} = \frac{1}{c} \vec{n} \cdot \vec{x}_{ij} & i, j \in 1..M, i \neq j \\ \dots \end{cases} \quad \text{Eq 2.37}$$

can be rewritten

$$\vec{\tau} = \frac{1}{c} \cdot D \cdot \vec{n} \quad \text{Eq 2.38}$$

with the different TDOA forming the time delay vector $\vec{\tau}$ and D a matrix depending only on the sensor locations. Reversing Eq 2.38 can easily solve the localization problem. From a mathematical point of view, we have to resolve an over-determined system of N linear equations to find two variables (2D-space) or three variables (3D-space). Thus the rank of D will determine the number of solutions.

In 2D space, two independent baselines (three sensors) are necessary for DOA finding without ambiguity and three independent baselines (four sensors) are necessary in 3D space. The next section introduces the inversion of D for M sensors in the 3D space.

2.5.2 Closed-form solution

The general solution of Eq 2.38 is given by

$$\vec{n} = c \cdot \mathcal{D} \cdot \vec{\tau} \quad \text{Eq 2.39}$$

where $\vec{n} = [n_x \ n_y \ n_z]^t$ is the wave vector and \mathcal{D} is the pseudo-inverse matrix of D calculated by the Singular Value Decomposition (SVD) method. Indeed, D is a square matrix and is invertible only if three independent baselines are considered. All other cases imply calculating the inversion of a rectangular matrix.

$$\mathcal{D} = (D' \cdot D)^{-1} \cdot D' \quad \text{Eq 2.40}$$

Finally, the wave vector component can be expressed in terms of the source azimuth Az and elevation El by using the relation

$$Az = \frac{\pi}{2} - \tan^{-1} \left(\frac{n_y}{n_x} \right), \quad El = \tan^{-1} \left(\frac{n_z}{\sqrt{n_x^2 + n_y^2}} \right) \quad \text{Eq 2.41}$$

The 3D representation of the azimuth and elevation angles is given in Figure 1.2.

2.6 Detection

2.6.1 Peak-picking step

The determination of the cross-correlation maxima is performed by a simple peak-picking procedure. By comparing the magnitude of a sample $R[n]$ to the previous $R[n-1]$ and the next one $R[n+1]$, it is possible to build the sorted peak vector composed of the first N_s (*a priori* number of sources) peaks:

$$R^{peak} = [R[n_1] R[n_2] \cdots R[n_{N_s}]]^t, \quad \forall i \in [0, N_s]: R[n_i] > R[n_{i+1}] \quad \text{Eq 2.42}$$

where n_i is the sample index of the i^{th} highest peak. The first element of the sorted vector supplies the most probable result as it corresponds to the highest correlation. In order to limit calculations, the peak-picking is restricted to physically reasonable delays with a few percent tolerance.

The operation is reiterated for each baseline. This enables to build the peak matrix composed of the cross-correlation $R_{n_b}^{n_p}$, where n_b is the baseline index and n_p is the peak index. The corresponding delay matrix is composed of the delay $\tau_{n_b}^{n_p}$.

2.6.2 Peaks recombination

Up to now, the maxima of each cross-correlation were considered to correspond to the true delays and thus to produce the true set of delays in order to localize the source. Realistically, it happens that the peak corresponding to the desired DOA is not the highest cross-correlation maximum: this appears, for example in low SNR conditions or when artefacts or ghosts are present. Furthermore, in the presence of several sources, each cross-correlation exhibits multiple maxima.

A sorting algorithm is therefore necessary to recombine the delays in order to reconstruct the different sets of delays for the localization. The method used to identify the true maxima combination is based on the minimization of the cost function defined by

$$\Gamma = \alpha \cdot J_{\vec{n}} + \beta \cdot J_{\tau} + \gamma \cdot J_R \quad \text{Eq 2.43}$$

where Γ is the recombination criterion. The coefficient α, β, γ are respectively the weightings of the norm cost function $J_{\vec{n}}$, the delay consistency cost function J_{τ} and the energy cost function J_R .

Norm criterion

The norm criterion is expressed by

$$J_{\vec{n}} = \left| \|\vec{n}\| - 1 \right| \quad \text{Eq 2.44}$$

It translates how well the delay set fits a physically plausible configuration. Indeed, according to the definition Eq 2.35, the norm of the wave vector is equal to unity. Thus, the distance between the norm

from unity is relevant to the distance between the candidate delays set and the closest physically plausible set.

Delay criterion

The second criterion expresses the fact that when the cross-correlations are calculated along a closed circuit, the sum of the delays must be equal to zero (i.e. $\tau_{12} + \tau_{23} + \tau_{34} + \tau_{41} = 0$). In such a case, the delays are said to be “consistent”. An offset will penalize the candidate combination as shown in

$$J_{\tau} = \sum_{n_b=1}^{N_b} \tau_{n_b} \quad \text{Eq 2.45}$$

where n_b is the baseline index, N_b is the total number of baselines forming a closed-circuit.

Energy criterion

The last criterion is derived from the peak magnitude information. The basic idea is to emphasize the highest peaks by penalizing the lowest. The energy criterion is expressed as the normalized distance between the highest delays set and the candidate delay set

$$J_R = \sqrt{\sum_{n_b=1}^{N_b} \left(\frac{R_{n_b}^1 - R_{n_b}}{R_{n_b}^1} \right)^2} \quad \text{Eq 2.46}$$

The following figures present a trial in an anechoic chamber. The cubic antenna is used in the presence of three white noise sources. The TDE is performed by the modified-CPSP ($\rho = 0.9$). To clarify the visualization of the DOA, the TDOA are multiplied by the speed of sound. The correlators are thus plotted in function of the path difference. The physical limits of the delays appear clearly (25 cm for edges, 37 cm for the diagonals).

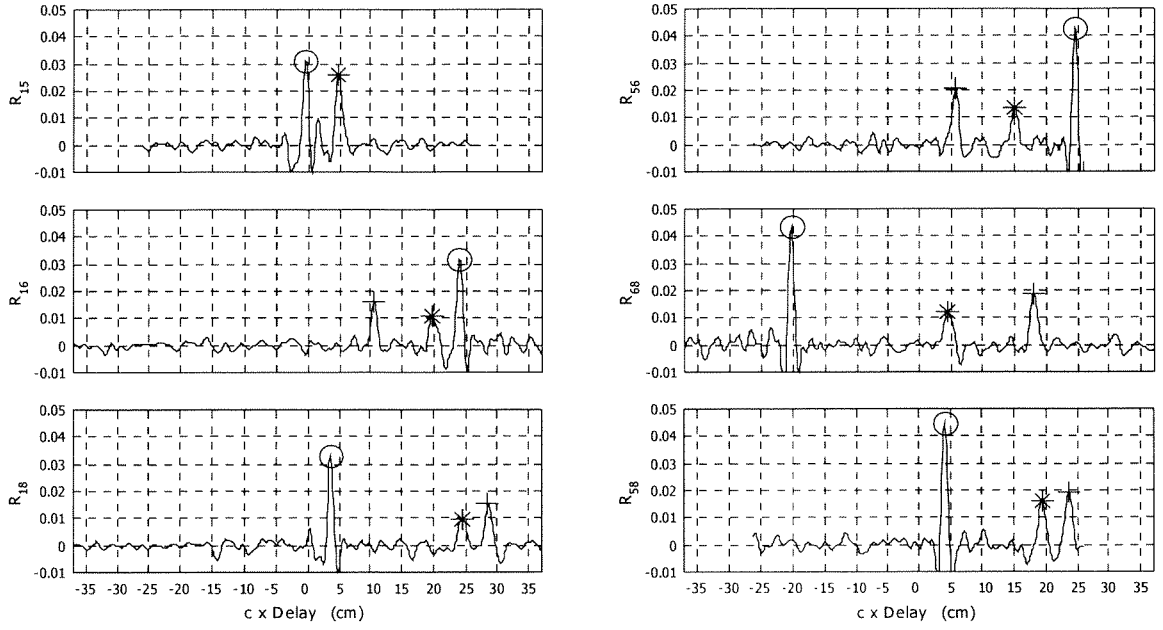


Figure 2.13 : Cross-correlations (CPSP method) of three white noise sources in anechoic chamber; four microphones of the cubic antenna are used (n°1, 5, 6 and 8); each of the six baselines are displayed

Once the highest maxima were located, the sorting algorithm calculates for each combination the cost function Γ . The table below presents the ten best combinations in terms of the recombination criterion. The three highest cross-correlation peaks of each baseline are located by the mark $R^{peak} = [O + *]^T$.

n°	R ₁₅	R ₁₆	R ₁₈	R ₅₆	R ₆₈	R ₅₈	$\alpha \cdot J_{\vec{n}}$	$\beta \cdot J_{\vec{r}}$	$\gamma \cdot J_R$	Γ
1	O	O	O	O	O	O	0.007	0.000	0.000	<u>0.007</u>
365	*	+	+	+	+	+	0.020	0.012	0.014	<u>0.046</u>
486	*	*	*	*	*	*	0.011	0.017	0.018	<u>0.048</u>
635	*	+	*	+	+	+	0.206	0.329	0.017	0.553
324	*	O	*	*	*	*	0.245	0.363	0.015	0.624
163	O	*	O	O	O	O	0.258	0.375	0.002	0.636
149	O	+	*	+	+	+	0.255	0.425	0.014	0.695
485	*	*	*	*	*	+	0.335	0.363	0.018	0.717
366	*	+	+	+	+	*	0.364	0.369	0.014	0.748
636	*	+	*	+	+	*	0.442	0.470	0.017	0.930

Table 1 : Ten best candidates in term of the recombination criterion; in gray the three delay sets validated

The first three combinations exhibit a very low cost function result (underlined in gray). The fourth combination presents a cost function ten times higher ($\Gamma=0.553 \gg 0.048$) and will be rejected. When observing the three first maxima combinations, it can be seen that the magnitude order "O + *" of the peaks is conserved. The first combination ('O') is composed of the highest maxima for each cross-correlation and so on for the two next combinations. Although this remark seems reasonable, it was observed in practice that this property couldn't be used directly to recombine the delays. For example,

the second maximum of cross-correlation R_{15} (outlined cell in Table 1) corresponds to two different sources as the baseline sees the sources under the same angle.

The total number of combinations is equal to $(N_S)^N$, where N_S is the estimated number of sources. In this case, 729 (3^6) combinations are tested. In order to reduce the calculations, a preliminary step based on the delay consistency test enables us to eliminate 90% of the potential combinations.

Criteria selectivity

The selectivity of the criteria translates how well the detection process discriminates true combinations from non-realistic ones.

The norm criterion is the most selective. Indeed, it tests the DOA and thus integrates all modules, in particular the antenna geometry. The delay consistency is only efficient to test closed circuits in the antenna but not the whole geometrical configuration, so that an error or a drift of an element in the relative position matrix D will appear in the norm but not in delay consistency criterion.

To visualize the difference in selectivity of each criterion, both cost functions were plotted in a 2D configuration including three sensors. The norm criterion is represented in Figure 2.14 and is expressed by

$$\sqrt{n_x^2 + n_y^2} = 1 \quad \text{Eq 2.47}$$

where n_x, n_y are the wave vector components along the x and y axes (defined inside the plan including the three sensors). The norm cost function appears as the distance between the candidate normalized wave vector v and the unity circle. If the norm criterion is translated in terms of delays (by using Eq 2.38), the circle becomes an ellipse, the size and axis of which translate the antenna geometry. The delay consistency expressed by

$$\tau_{12} + \tau_{23} + \tau_{31} = 0 \quad \text{Eq 2.48}$$

describes a plan including the origin and containing the norm ellipse (Figure 2.15). This means that each combination satisfying the norm criterion satisfies the delay consistency criterion.

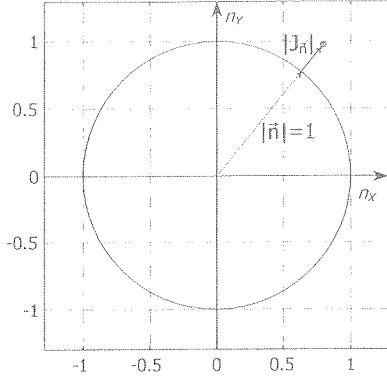


Figure 2.14 : Norm criterion in a 2D configuration
– representation of the norm function

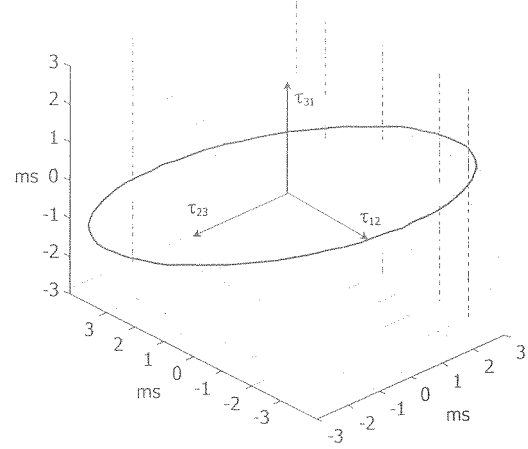


Figure 2.15 : Norm and delay consistency criteria
in the temporal domain

If a sensor is accidentally displaced during the goniometry, the candidate delay set will move away from the circle but will stay inside the plan and will continue to provide low delay consistency cost values. Thus a geometry alarm can be implemented by studying the history of the cost functions of the tracked sources. This consideration can be extended to a 3D goniometry without reserve.

Determination of the weightings $\alpha \beta \gamma$

The weightings of the criteria reflect the confidence that can be given in the different modules. For example, the infrasound localization involves a 50 m wide antenna. Both acoustic centers of the sensors and their positions are not precisely known. So, a low value of α would be adequate. Yet, an automatic determination of the weighting is preferred to a “know how” based manual approach.

The weightings determination is based upon a calibration procedure. The weightings are chosen in such a way that when a source is tracked, each term of the cost function has the same influence. The calibration has to be realized on a typical localization configuration over a statically representative number of frames N_f . The proposed weightings are

$$\alpha = \frac{1}{\sigma(J_{\vec{n}}^S[n_f])} \quad ; \quad \beta = \frac{1}{\sigma(J_{\vec{\tau}}^S[n_f])} \quad ; \quad \gamma = \frac{1}{\sigma(J_R^S[n_f])} \quad n_f = 1..N_f \quad \text{Eq 2.49}$$

where $J_{\vec{n}}^S[n_f]$ is the norm cost function calculated on the true delays over the frame of index n_f .

2.6.3 Delay set validation

The validation stage is the last step of the detection. It compares the norm and the consistency criteria of the best candidates to decision thresholds. The determination of the thresholds is obtained by the same approach as the definition of the weightings. A delay set is validated if both their associated norm and delay cost functions do not exceed the respective threshold defined by

$$\begin{aligned} J_{\vec{n}}^{th} &= K_{th} \cdot \sigma \left(J_{\vec{n}}^S [n_f] \right) \\ J_{\vec{\tau}}^{th} &= K_{th} \cdot \sigma \left(J_{\vec{\tau}}^S [n_f] \right) \end{aligned} \quad \text{with} \quad n_f = 1..N_f \quad \text{Eq 2.50}$$

where the coefficient K_{th} is set in agreement with the detection performance required (detection probability and false alarm rate). Typical values are from $K_{th}=2$ to 5.

The understanding of the tolerances to be accepted is better when the thresholds are expressed in terms of distance (see Annex 7.3). For example, the trials in an anechoic room with a cubic antenna lead to norm threshold of 5 mm ($\cong 1\%$ of the antenna extension). On the other hand, in-situ infrasound localization leads to norm tolerance of 5 m ($\cong 10\%$ of the antenna extension).

2.7 Extra modules

2.7.1 Integration in the goniometer design

Although they are not essential to the goniometry, the modules introduced in this section are adds-on that complement the localization. The Figure 2.16 presents their respective chronological positions in the goniometry flowchart. The distinction is made between the frame and the event-based approach.

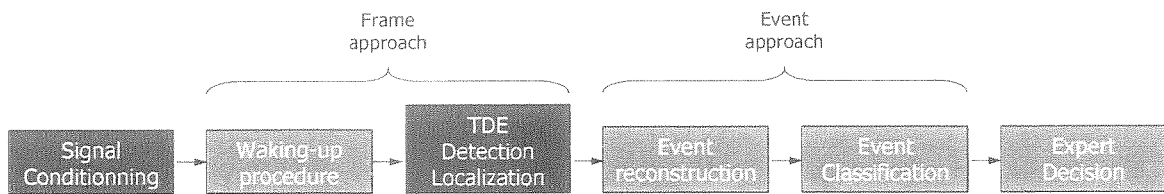


Figure 2.16 : Extra modules chronology

2.7.2 Waking up module

When post-processing large amounts of data or in a real-time process, it can be necessary to implement a *stand by* mode. Its purpose is to “wait” for relevant information. In the case of a “*waking-up*” order, the localization is processed as shown in the following figure:

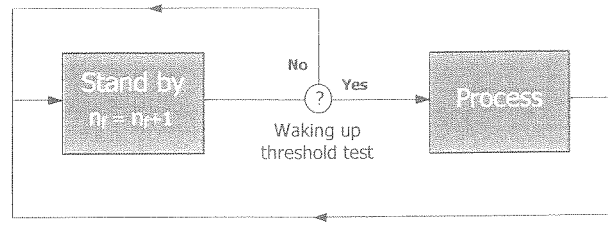


Figure 2.17 : Process activation procedure

The information used to implement the waking-up test is based on both the Power Spectrum Density and the coherence.

The coherent power spectrum [5] is given by

$$SCoh^3(f) = G_{11}(f) \cdot (C_{12}(f))^3 \quad \text{Eq 2.51}$$

where the magnitude-squared coherence C_{12} is calculated by applying Eq 2.25. The coherence term has a whitening effect on the PSD. Indeed, the coherence traduces the emergence of the signal on the uncorrelated noise (i.e. wind, electronic). Low SNR frequency bands will be attenuated. The whitening effect is clearly observed when comparing the classical sonogram to the $SCoh^3$ correlogram of an infrasonic event in windy conditions (Figure 2.18).

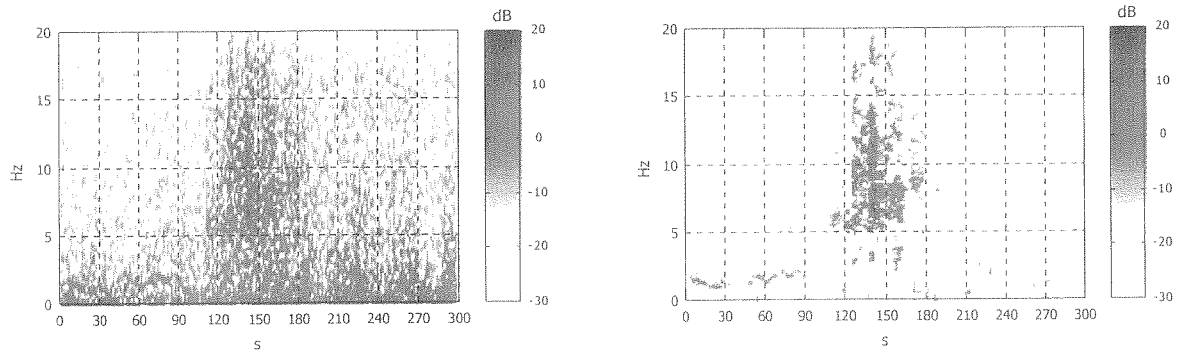


Figure 2.18 : Sonogram (Left) and $Scoh^3$ (Right) of a jet in windy condition

The frequency bands presenting high $SCoh^3$ are relevant of coherent acoustic energy across the antenna. This can foreshadow an event to be localized and will be processed. The determination of the frequency bands to test and the threshold are based on the *a priori* information on the signal spectrum and the $Scoh^3$ study in a no-source case.

Preliminary works on the avalanche acoustic signatures enabled us to set the upper frequency at 10 Hz. The $Scoh^3$ was, thus, summed over the band below 10 Hz and then compared to the threshold.

2.7.3 Event build up

Up to now, the localization was processed on successive frames. The event reconstruction module handles the final DOA results in order to build up the acoustic events. Indeed, the physically plausible trajectories define a maximum DOA displacement from frame to frame. The event reconstruction algorithm is presented in Figure 2.19.

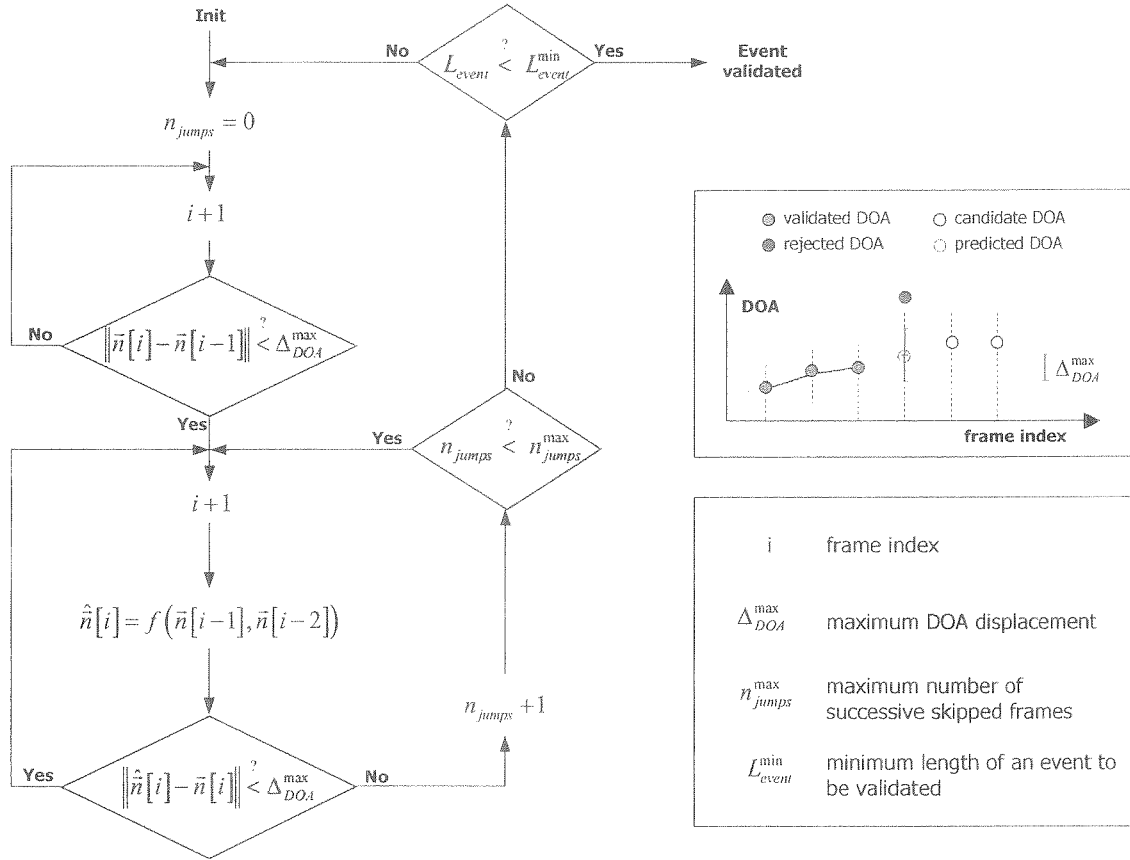


Figure 2.19 : Event reconstruction flowchart

An event determination procedure is undertaken when two successive DOA are close enough. Then the idea is to predict the next DOA according to a characteristic trajectory and to compare it to the measured DOA. If the distance between the prediction and the measurement is below the “maximum DOA displacement” tolerated, hence the DOA measurement will be validated and will be part of the potential event. If not, the predicted DOA is validated and the number of jumps is incremented (one frame has been bypassed or “jumped”). This procedure stops when the number of tolerated jumps is reached. If the event length satisfies the minimum length condition, the event is validated.

Considering the avalanche localization, the typical event minimum length is 20 s (8 frames). The number of skipped frames is set to 1 or 2 and the tolerated DOA displacement is set to 20°.

2.7.4 Classification

The event classification is based upon *a priori* information on the tracked source and on the competing sources. The $SCoh^3$ calculated over relevant frequency bands is chosen as discriminator. A training stage allows determining the frequency bands that minimize the false alarm rate. For example, preliminary studies on the avalanche have shown that the decomposition of the spectrum into four bands (0-5, 5-10, 10-15, 15-20 Hz) allowed us to discriminate avalanche events from competing sources with high performances. For example, the next table presents the $SCoh^3$ repartition (in %) of the five source patterns.

Pattern	$SCoh^3$ (%) [0-5 Hz]	$SCoh^3$ (%) [5-10 Hz]	$SCoh^3$ (%) [10-15 Hz]	$SCoh^3$ (%) [15-20 Hz]
Avalanche (type I)	50	35	10	5
Avalanche (type II)	20	50	20	10
Long range supersonic flight	90	10	0	0
Competing source	0	0	100	0
Competing source	0	0	0	100

Table 2 : Model characteristics

The classification is performed through a "*nearest-neighbor method*": the class chosen is the one that minimizes the distance between the event and the pattern. More information on the principles of the classifiers can be found in [24].

Chapter 3

Performance

3.1 Detection & precision: overview of the sensitive parameters

In order to estimate the performances of the goniometry, an exhaustive list of all the parameters influencing the DOA estimation was edited. The effect of the parameters on the solution was then studied both through theoretical and simulation approaches and experiments. Once the relations between the sensitive parameters and performance were established, it becomes possible to design a goniometer that fulfills the performance requirements. Figure 3.1 summarizes the interaction between the modules, variables and influencing parameters. The chronology of the artefact, imprecision or bias contamination is relevant to the way they reverberate on the final result.

The first sensitive parameters group describes the operational context (emission – propagation – reception). The emission is characterized by the signal properties: the bandwidth B and the central frequency f_c . The transmission includes the propagation phenomena such as the medium absorption, the reflections, the refraction, the scattering or medium displacement. The reception is characterized by the signal to noise ratio SNR . The second group is made of the algorithms and their parameters. Finally, the parameters interacting on the localization module are the speed of sound c , the sensor relative positions matrix D , the localization method and experimental conditions such as the source range R and the relative source-goniometer set-up. More precisely, the localization performances are related to the estimation errors on the speed of sound, on the position matrix and the induced errors due to far-field assumption.

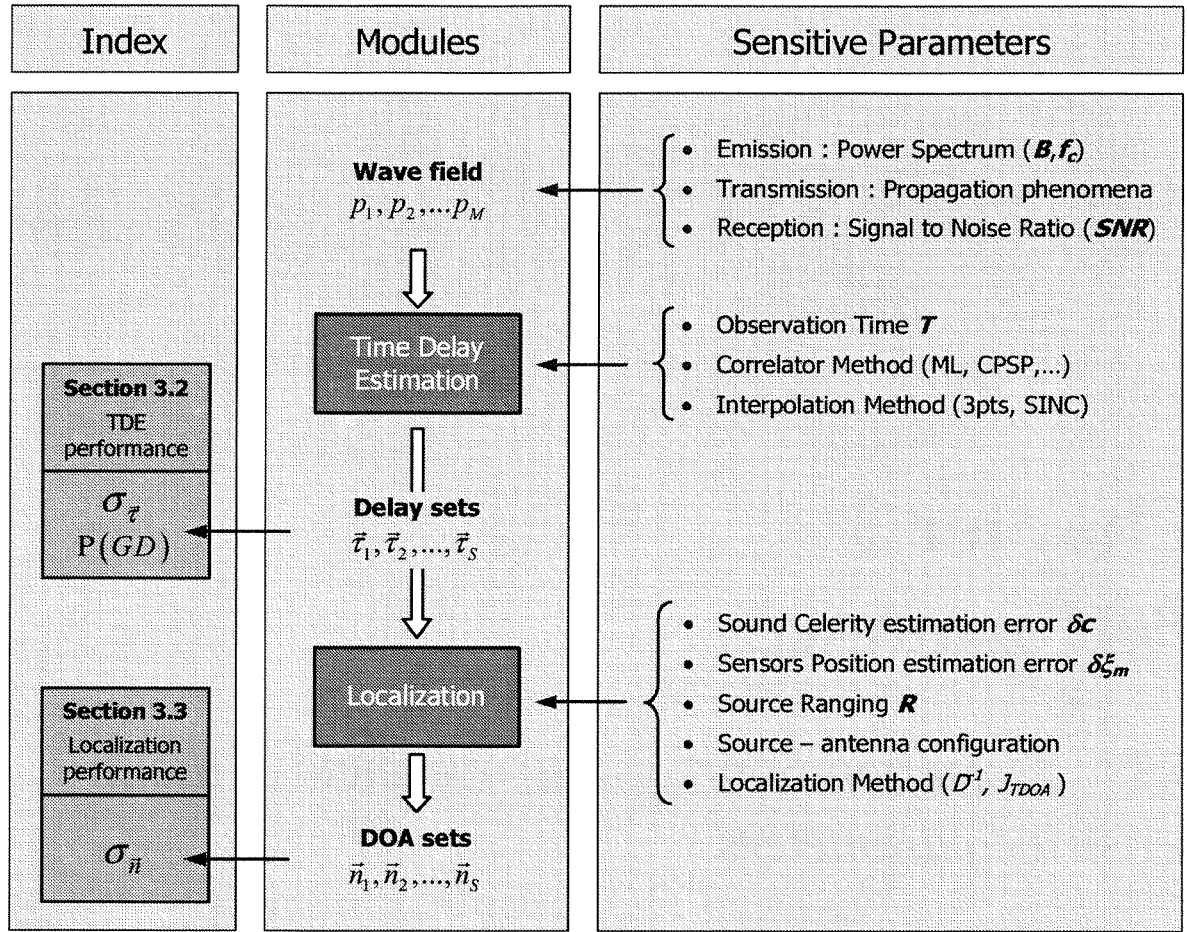


Figure 3.1 : Sensitive parameters related to the goniometer schematic diagram

Early investigations can be performed on the TDE by calculating the variance of the TDE and the probability of Good Detection (GD) through Monte Carlo series [64]. The optimization of the results drives the parameter determination. Finally, the DOA variance reveals the overall goniometer performance. The statistics on the DOA will be expressed in degrees to facilitate the visualization.

Following the application, some of the sensitive parameters are imposed although others allow performance optimization. Most of the time, the operational context is not modifiable. The goniometer will then be placed, when possible, in the best location so as to reduce undesirable propagation phenomena and to record the signals in the best SNR conditions.

In the case of the active localization, the source signal generation is controlled and allows fitted design. Its characteristics, as well as the calculation methods and algorithms parameters, will be determined through simulations by directly optimizing the TDE and localization performances.

3.2 TDE Performance

3.2.1 Emission – reception: signal characterization

Bandwidth and central frequency

The determination of the potential performance of a goniometer requires the estimation of the bandwidth and the central frequency of the signal. This task can prove to be very difficult in real life cases. The classical model of a band-pass signal is presented in Figure 3.2. The power spectrum, concentrated inside the frequency band $[f_{\min}, f_{\max}]$, is supposed to be flat inside the bandwidth (white noise type).

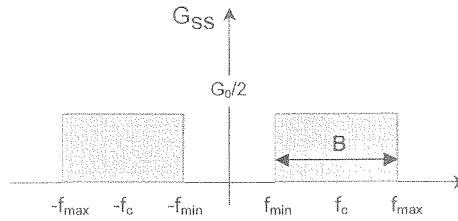


Figure 3.2 : Spectrum model of a band-pass signal

The central frequency and the bandwidth are related to the cut-off frequencies by

$$B = (f_{\max} - f_{\min}) \quad f_c = f_{\min} + \left(\frac{f_{\max} - f_{\min}}{2} \right) \quad \text{Eq 3.1}$$

Signal to Noise Ratio

The *SNR* is defined as the ratio between the signal power and the noise power. As previously defined in section 2.2, the signal represents the contribution to track, whereas the noise contains all other components. The discrete time domain relation is given by

$$SNR = 10 \cdot \log_{10} \left(\frac{\sum_{k=1}^K (s[k])^2}{\sum_{k=1}^K (n[k])^2} \right) \quad \text{Eq 3.2}$$

However, the signal and noise are rarely accessible separately. The comparison of the configurations source/no source enables us to estimate $(S+N)$ and N . If the noise is independent of the signal, then the *SNR* is easily obtained by subtracting the N from $(S+N)$ estimation. The background noise (incoherent) and the interfering noise (competing sources) fulfill this requirement. The coherent noise due to image sources does not. Therefore, the resulting *SNR* is reduced in relation to the number of source images, as they are additional noise sources.

3.2.2 Performance indexes

The relevant indexes to compare the TDE performances are the TDE variance, the TDE bias and the detection probability. A *good detection* means that the right peak was selected, a *false alarm* means that a peak was found where nothing occurred and a *non-detection* refers to a source event that was not seen.

At the same time, the emergence of the cross-correlation peaks on the background (floor) needs to be estimated to know the headroom. The proposed function is the multi-sources equivalence of the « Peak to Floor Ratio » proposed in [80]. The multi-sources Peak to Floor Ratio (*pfr*) is given by the mean of the N_s cross-correlation maxima values divided by the mean cross-correlation noise.

$$pfr = \left(\sum_{s=1}^{N_s} \frac{R[k_s]}{N_s} \right) / \left(\sum_{k=1, k \neq k_s}^K \frac{|R[k]|}{K - N_s} \right) \quad \text{Eq 3.3}$$

where N_s is the number of sources in presence, k_s is the index of the peak, and K is the cross-correlation length. For $pfr=1$, the peaks are of the same order of magnitude than the background noise. A second version is proposed in decibel:

$$PFR = 10 \cdot \log_{10}(pfr) \quad \text{Eq 3.4}$$

3.2.3 Cramer-Rao Lower Bound, anomalies and ambiguities

Extensive literature can be found on the estimation the Cramer-Rao Lower Bound (CRLB) of the Time Delay Estimation. Its use is justified by invoking the statistical theorem asserting that the Maximum Likelihood estimator is asymptotically unbiased and that its error variance approaches the CRLB for sufficiently long observation times. The CRLB can be seen as the optimal performances that can be achieved for a given set of parameters. In such a case, all the information (entropy) is used. The calculation of the CRLB enables us to understand the weighting of the different parameters in the overall performance. The CRLB is only valid when the goniometer is in “*Tracking*” mode (see Figure 3.3), when the SNR is sufficiently high, so that the correct peak always emerges from the cross-correlation noise. When the SNR decreases, the background noise of the cross-correlation increases relatively to the true cross-correlation peak. The peak-picking step can fail to select the right peak inducing a severe drop in performance.

This sudden decrease in performance corresponds to the transition zone of the so-called “*ambiguities*”. The probability of good detection fall from 1 to 0, the peak-picking step is no more capable of finding the right peak. If the SNR decreases another time, a second step appears. This very low performance region is the zone of the “*anomalies*” also called the envelope ambiguities and is useless for the TDE.

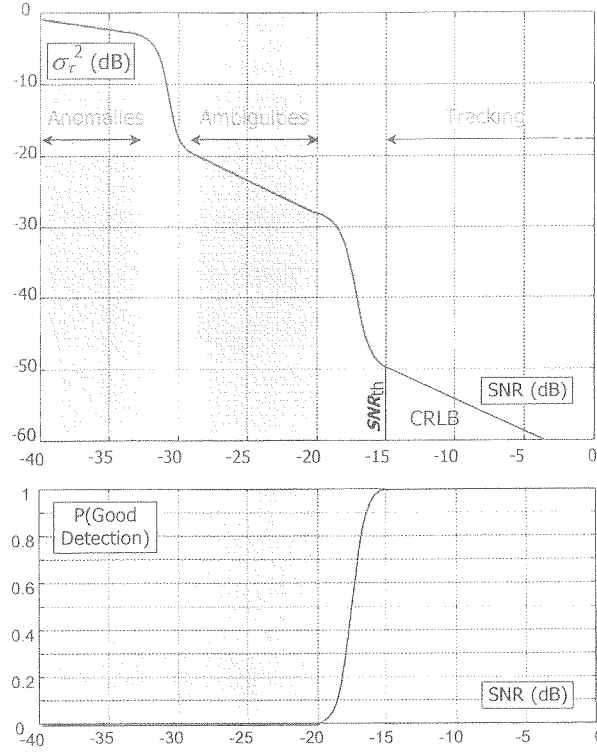


Figure 3.3 : Performance index as a function of the SNR

The difference between the ambiguities and anomalies is shown on a typical cross-correlation of a band-pass signal (Figure 3.4). The ambiguities are related to the central frequency f_c of the band-pass signal and the anomalies to the bandwidth B .

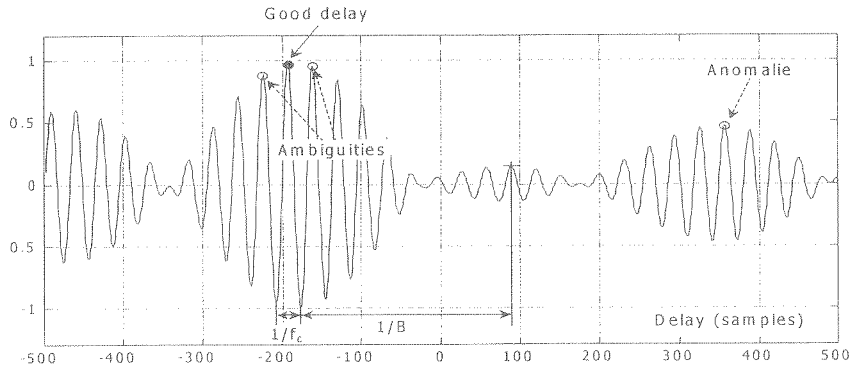


Figure 3.4 : Typical Cross-correlation function of a band limited signal

In the tracking zone ("Lock-In mode"), the TDE variance of a low pass signal corrupted with wide-band noise is given in high SNR condition by [74]

$$\sigma_{CRLB}^2 = \frac{3}{4\pi^2} \cdot \frac{1+2 \cdot SNR}{SNR^2} \cdot \frac{1}{B^3 T} \quad \text{Eq 3.5}$$

This relation reveals how important the bandwidth is. If B doubles, the variance on the TDE is divided by eight. The beneficial action of the observation time T is very interesting as it appears to be, in many case, the only parameter that can be modified. The formula are given in annex 7.1 for different configurations (high-low SNR , low-pass – band-pass signals). For example, the CRLB of a band-pass signal is dependant of the central frequency f_c . If the bandwidth is fixed, the variance on the TDE decreases for increasing central frequency, as the peak sharpens.

Different bounds have been proposed to describe the ambiguities zone. For example, the Ziv-Zakai Lower Bound (ZZLB) [113], the Barankin Bound [18] and the Correlator Performance Estimate (CPE : [46],[47],[48]) have been studied with respect to different operating hypotheses. The CPE proposed by Ianniello (annex 7.1) is a function of the CRLB weighted by the false detection probability. The intersection between the CRLB and the ambiguity zone variance estimator is defined by the SNR threshold SNR_{th} . Above the threshold, the process is ambiguity-free.

3.2.4 Correlators comparison and enhancement

Theory and real case

The performances of the generalized cross-correlator were extensively compared in literature ([43],[56],[90]). The main conclusion is that the results are highly dependent of the initial hypotheses and operating configurations. In this sense, it is very difficult to forecast whether the classical cross-correlation, the SCOT transform, the ML, the CPSP or the modified CPSP will perform best in terms of TDE variance, of probability of detection and Peak to Floor ratio.

The attitude, taken when tackling a new application, was to compare the performances by Monte-Carlo series. Up to now, either the ML estimator, or the modified CPSP were always found to perform best. Yet, the classical cross-correlation was chosen for a DSP implementation as it can be performed in the time domain.

3.2.5 Transmission: wave propagation influence

Attenuation –diffraction – refraction [86]

The impact of these propagation phenomena on the performances has not been studied during this work. They would deserve particular researches *per se*. Yet, a qualitative description of their effects on the TDE was necessary to classify them as first or second order influencing parameters.

The sound attenuation is mainly due to geometrical attenuation and medium absorption. Its main effect is to deteriorate the SNR . Furthermore, as the medium absorption growths with increasing frequencies, the signal spectrum is modified and can be reduced to the low-frequency band when the source is far. The bandwidth is reduced as well as the central frequency and so the performances decrease.

The diffraction[114] is considered as the change in direction of propagation of the wavefront due to the presence of an obstacle or discontinuity (with no change in velocity). This phenomena bends the wave vector with the consequence that an image secondary source appears located at the object boundary.

The refraction is the change in direction of propagation of the wavefront due to a change in its velocity (usually caused by a change of medium) and refers to different medium interface. For example, the infrasonic ducts are the consequence of refraction phenomena in the atmosphere layers (various temperature, pressure). Infrasonic sources, as the Concorde, can be observed 1000 km away in adequate configuration.

Both diffraction and refraction have the same effects on the TDE. Yet, two distinct cases are observed. When the phenomena perturb the signal propagation, the resulting effect is a wave vector bending inducing the goniometer to localize an apparent source without any decrease in performance localization. When the phenomena perturb directly the sound pick-up, that is, when refraction or diffraction occur across the antenna (non-homogenous medium), the performance drops, as well as the coherence between sensors [77].

Reflections

The goniometer processes reflections as waveforms coming from the image source predicted by ray theory (specular reflection). The goniometer cannot directly discern a direct component from a reflection without any *a priori* information. In the propagation model described in

$$\begin{aligned} x_1(t) &= \alpha s(t - \tau_1) + \alpha' s(t - \tau'_1) \\ x_2(t) &= \alpha s(t - \tau_2) + \alpha' s(t - \tau'_2) \end{aligned} \quad \text{Eq 3.6}$$

the reflected contribution (with $()'$ notation) only differs by the attenuation due to different paths and surface absorption and by the delay.

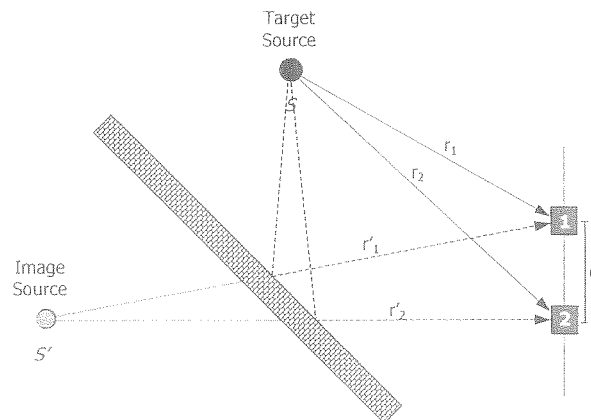


Figure 3.5 : Direct and reflected contributions

The propagation diagram (Figure 3.5) highlights the problem of cross-contribution terms resulting in **ghosts** (cross-correlation peaks without any physical sense). Indeed, as the direct and reflected contributions are highly correlated, the cross-correlation will exhibit four maxima: two corresponding to the source and the image source, and two resulting from mixed- contributions (i.e. the direct contribution recorded by sensor 1 correlated to the reflected contribution recorded by sensor 2).

These mixed contributions can be easily shown when developing the cross-correlation in the Fourier domain. If the attenuation effects are neglected, the different contributions are transformed into

$$s(t - \tau_1) = \delta(t - \tau_1) \otimes s(t) \xleftrightarrow{\mathcal{F}} S(\omega) \cdot e^{-j\omega\tau_1} \quad \text{Eq 3.7}$$

Thus the Cross-Power Spectrum is given by

$$\begin{aligned} G_{12}(\omega) &= X_1(\omega) \cdot X_2^*(\omega) \\ &= S(\omega) \cdot S^*(\omega) \cdot \left[e^{-j\omega(\tau_1 - \tau_2)} + e^{-j\omega(\tau'_1 - \tau'_2)} + e^{-j\omega(\tau_1 - \tau'_2)} + e^{-j\omega(\tau'_1 - \tau_2)} \right] \end{aligned} \quad \text{Eq 3.8}$$

Applying Eq 2.9, the cross-correlation is written

$$R_{12}(\tau) = \left[\delta(\tau - \tau_{21}) + \delta(\tau - \tau'_{21}) + \delta(\tau - (\tau_1 - \tau'_2)) + \delta(\tau - (\tau'_1 - \tau_2)) \right] \otimes R_{ss}(\tau) \quad \text{Eq 3.9}$$

where \otimes is the convolution operator and R_{ss} is the autocorrelation of the source signal. The third and fourth terms induce non-physical peaks. These ghosts can be avoided if the mixed delays are beyond the maximum physical lag τ_{max} . The condition to reject the ghosts outside the observation window can be written in terms of distance through

$$r_1 - r'_2 < 2d \quad ; \quad r'_1 - r_2 < 2d \quad \text{Eq 3.10}$$

To insure that the cross-contributions will not disturb the cross-correlation, the inequality " $<$ " should be modified to " $<<$ " as the Dirac function associated with the cross-contributions are convoluted by the auto-correlation of the signal source.

Application: Effect of the snow cover

A solution consisting in burying the infrasonic microphones below the cover was proposed to reduce the effect of the wind noise. It was observed that the snow cover affected the propagating wave in both amplitude and phase. Figure 3.6 presents the experimental configuration and the spectrum analysis of the signals recorded above and below the snow cover. In Figure 3.7, the transfer function is estimated in amplitude and phase and is validated for the band 2-20 Hz by the coherence function. The attenuation corresponds to a low-pass filter behavior (slope = - 12 dB/decade) and the phase rotation corresponds to an apparent speed of sound of 150 m/s in the snow cover.

Although the signal attenuation do not affect seriously the goniometry, the extra delays introduced by the snow cover are critical to the localization [1]. If the snow conditions are not homogenous over all the sensors, random additional propagation time will deteriorate the TDE.

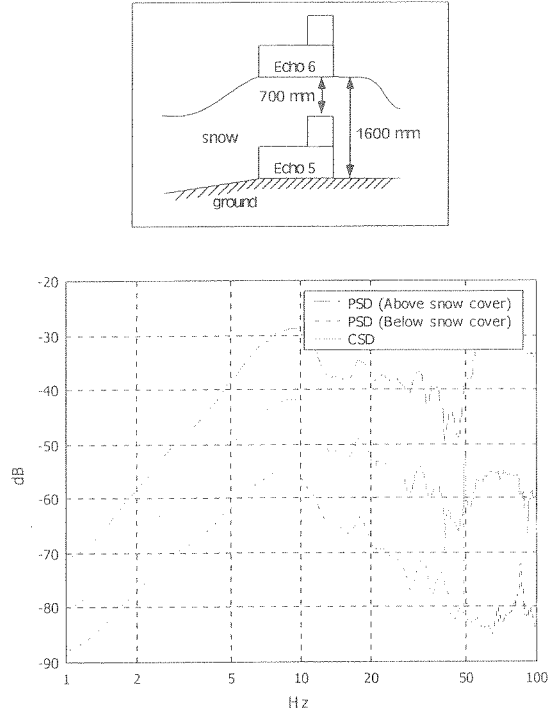


Figure 3.6 : Experimental configuration - Power Spectrum Density and Cross Power Spectrum Density

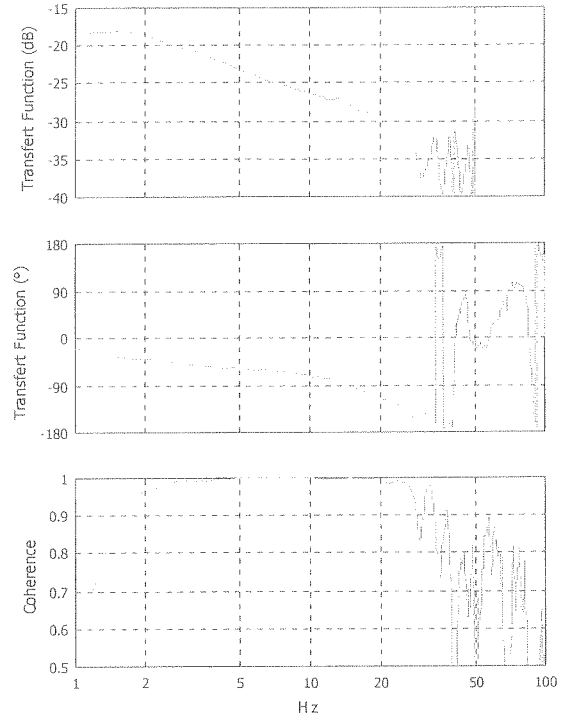


Figure 3.7 : Snow cover transfer function - coherence between microphones

Medium displacement

The flow of the propagation medium (wind, water current) induces a deviation of the wave vector when the displacement is homogenous (steady flow component) with respect to the antenna, whereas it induces decreases in the localization performance when turbulences have local effects on the sensors (turbulent components).

The wind effect on the localization has been studied in the case of infrasonic antenna of Anzère (section 5.2). Figure 3.8 presents the steady wind effect on the localization and Figure 3.9 shows the decomposition of the wind action into a steady component (homogenous) and a turbulent component (local).

Simulations have shown that in calm conditions (steady wind = 2 m/s, wind blow = 8 m/s), the estimation bias on the azimuth was 0.5° with a STD of 1.1° , and that in windy conditions (steady wind = 5 m/s, wind blow = 20 m/s) the azimuth bias was 1.2° and azimuth STD was 3° .

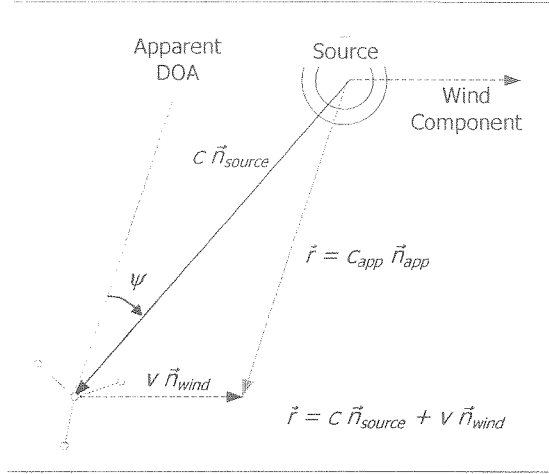


Figure 3.8 : Steady wind effect, apparent source

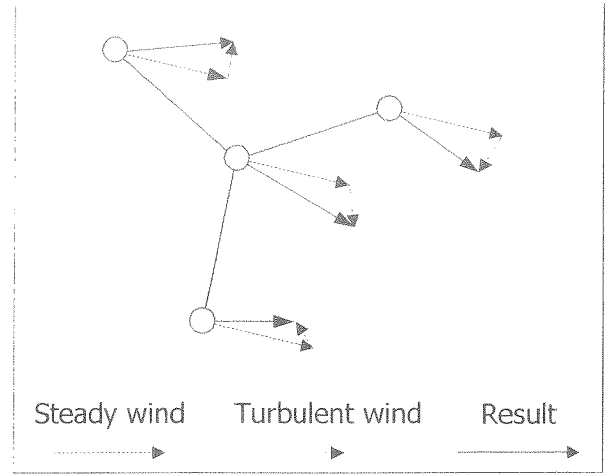


Figure 3.9 : Wind decomposition in steady and turbulent components

3.2.6 Wind effect on the SNR and coherence

Overview

In outdoor applications, such as localization of avalanches, airplanes, helicopters or artillery, the wind introduces undesirable effects, which can make goniometry impossible. The different outcomes of windy conditions are classified following the goniometry modules they affect. The acquisition module is troubled by the wind for input dynamics considerations; the TDE is perturbed by the SNR degradation and the coherence drop, and finally the localization modules is penalized by wave vector bending phenomena.

SNR degradation

The first restriction induced by the wind is the SNR decreasing. It was found that wind-induced noise is composed of two components ([3],[25]). The first one, called the *intrinsic turbulence*, is caused by the turbulence of the airflow in the vicinity of the diaphragm. Variations in wind speed and direction generate very localized changes in air pressure, which result in noise. The second component is turbulence generated by the microphone or the added windscreen exposed to the air-stream and is called *interaction wind noise*. The air passing around the microphone creates wake vortices when recombining at the leeward side. These vortices become small sources that radiate sound in all directions. Morgan and Raspet have shown that in turbulent airflow, as encountered in outdoor conditions, the interaction wind noise is negligible compared to the intrinsic turbulence [63]. On the other hand, laminar flow, as encountered in moving sound pick up in non-fluctuating wind, induces little intrinsic turbulence and the wake generation becomes the dominant noise source.

Hence, these wind components do not present any coherence between the array sensors. The SNR drop off infers a performance reduction as explained in section 3.2.1.

The spectrum of the intrinsic turbulence is dominated by low frequencies. As shown in Figure 3.11, the wind-induced noise presents a nearly $1/f$ behavior (-6 dB/oct) and thus becomes critical in infrasound applications. The evolution of the acoustic pressure and wind presented in Figure 3.10 was observed at the Avalanche Experimental Site of Anzère (Altitude = 2500m).

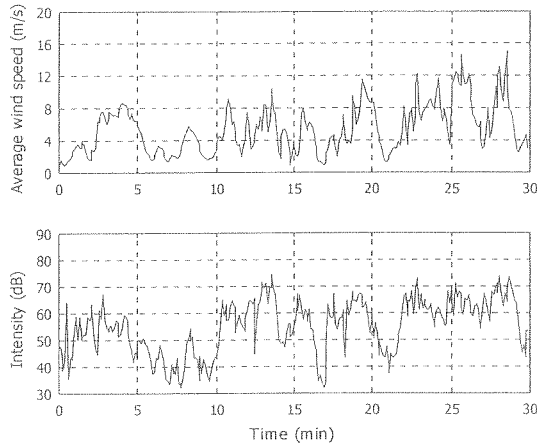


Figure 3.10: Temporal evolution of the average wind speed and the acoustic pressure

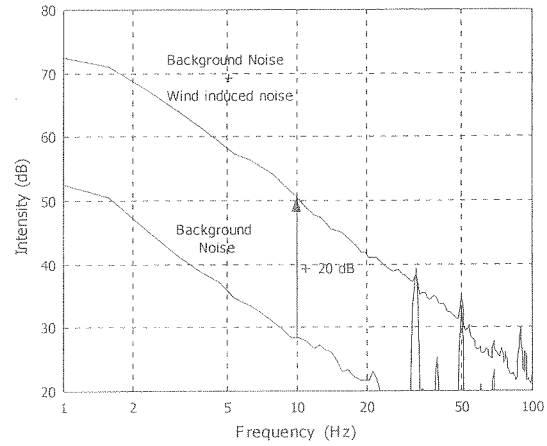


Figure 3.11: Frequency analysis of the induced wind noise compared the background ambient noise

The comparison of the wind evolution and the induced wind noise shows a general similarity. Second order differences are imputed to the 100m distance separating the microphone from the anemometer and reveal very local wind conditions.

In order to reduce these undesirable components, windscreens were designed. The complete protection barrier adopted in the infrasound pick-up system is made of an open cell polyurethane foam directly put on the microphone, covered then by a Gortex protection (rosy color) against humidity and finally by the “Anzère” windscreen made of 60x60 cm half-open cell foam as shown in Figure 3.12.

The main goal of the “Anzère” windscreen is to low-pass filter the pressure fluctuations at the surface of the windscreen and to create a laminar air flow inside the protection. Indeed, the windscreen achieves an averaging of the air turbulence over the entire surface and induced a drop of airflow. This requires that the windscreen dimensions are large when compared to the wind turbulence wavelength. Considering the 60 X 60 cm “Anzère” protection exposed to a gust of wind at 5 ms^{-1} , ($f=8\text{ Hz}$ for $\lambda = 0.6\text{ m}$), the low-pass filtering of the protection would be effective for gust wavelength below 0.2 m (25 Hz). The gusts of wind at higher frequencies are broken in smaller eddies and will be attenuated by the second stage protection (open cell foam) according to the same mechanism.

In the Tetraftia windscreen design, the problem is to terminate a 5 cm diameter tube (Figure 3.13). The dimensions being imposed, different materials were tested. The best choice incorporates a

compromise between the loss of sensitivity due to the acoustic resistance introduced by the protection and the wind induced noise reduction gain. In this study, the sintered bronze termination was chosen.



Figure 3.12: Norsonic microphone protected by open cell foam with Gortex protection and the “Anzère” windscreen

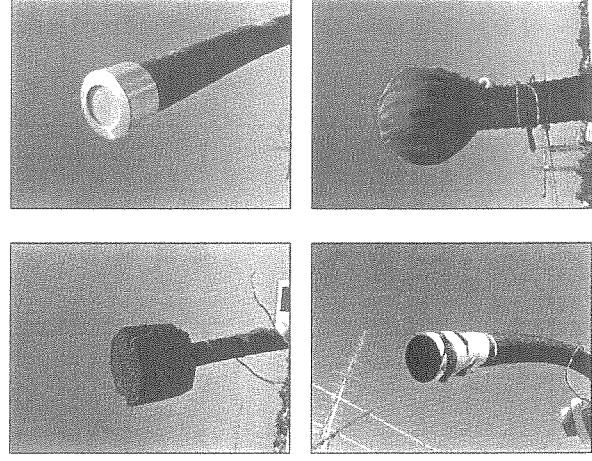


Figure 3.13: Tetraftia Wind protections (From left to right and up to down: sintered bronze, open-cell foam + Gortex, half-closed foam, and open cell foam inside the tube + Gortex skin)

The second wind induced noise component, the interaction noise, generates frequency components related to the size and shape of the windscreen and the wind velocity. When the shape can be assimilated to a circular cylinder, these variables are linked by

$$St = f \cdot \frac{\Phi}{V} \quad \text{Eq 3.11}$$

where St is the Strouhal number ($St = 0.2$), V the average wind velocity, Φ the windscreen diameter and f the vortex shedding frequency. For example, under the hypothesis of an equivalent cylindrical of a 70 cm diameter, and $V = 5 \text{ ms}^{-1}$, the induced frequency on the “Anzère” protection is about 1.4 Hz.

Coherence loss

The formulation of the generalized cross-correlation has demonstrated the critical importance of a “good” coherence between the input signals: as the time delay estimation is based on the Cross Spectrum Density, it is important that the signal spectra present linear dependence for all frequencies. The amount of shared information can be estimated by integrating the magnitude-squared coherence over the entire relevant spectrum. The resulting index represents the degree of linearity of the relation between the two signals.

In order to cope with outdoors conditions required for the Silence Light Project (section 5.3), different windscreen solutions were evaluated in the coherence sense. Laboratory tests were driven with a 40 cm fan in order to recreate the turbulent wind conditions (Figure 3.15). Although the turbulences were observed, their wavelengths are smaller than those expected in outdoor conditions. The MSC

calculated at low frequencies are in that sense over-evaluated. In these tests, the average wind speed measurement was chosen to describe and quantify the turbulence.

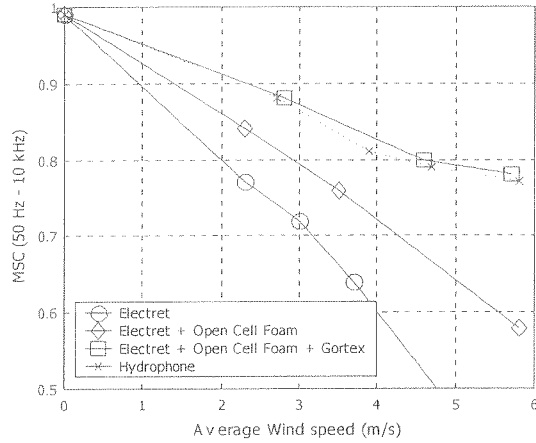


Figure 3.14 : Magnitude-squared coherence evolution for different wind speed – Experimental tests

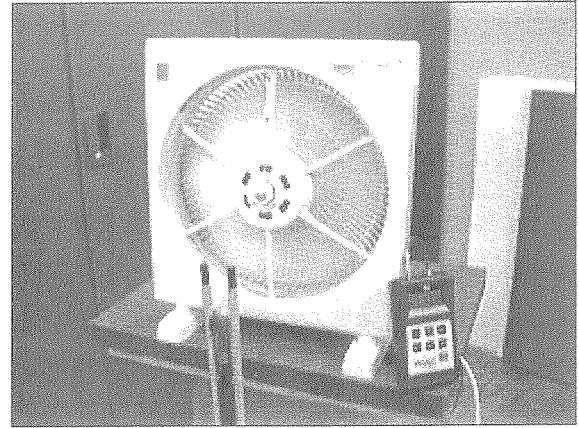


Figure 3.15 : Hydrophones pair in the presence of turbulent wind with Anemometer measurements

Figure 3.14 presents the MSC loss as a function of the average wind speed for four microphone – windscreen configurations. The first configuration is made of two electrets microphones (Sony ECM-77, ½ cm diameter) without any protection; the second is enhanced by the addition of an Open-Cell Foam (diameter: 1.2 cm, length: 2 cm); the third corresponds to the second with an extra Gortex material protection (principally used against rain); the last one involves hydrophones BK 8103. The graph analysis reveals, firstly, that the MSC decreases linearly with the average wind speed, independently of the microphone configurations and that the line slopes are relevant for the protection quality. Secondly, that the performance gain obtained when adding the Open Cell Foam and the Gortex justifies their use and the design efforts afforded. Finally, that the hydrophones solution acts as well as the Electret – Foam – Gortex configuration, but is much more expensive.

3.3 Localization performance

3.3.1 Two sensor goniometry: influence of parameters

The simple case of 2D goniometry with a pair of sensors is represented in Figure 3.16. In the far-field case, the DOA is completely defined by the angle θ and is obtained by the relation

$$\theta = \sin^{-1}\left(\frac{c\tau}{d}\right) \quad \text{Eq 3.12}$$

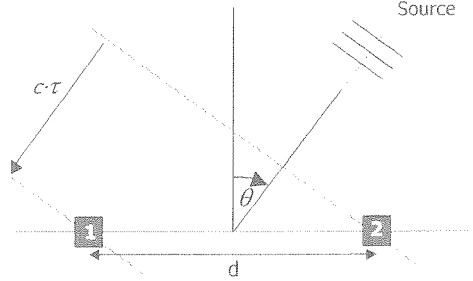


Figure 3.16 : 2D propagation model

To observe the robustness of the DOA estimation in the presence of the parameter errors $\{\delta c, \delta d, \delta \tau\}$, Eq 3.12 was developed into a Taylor Series around the nominal values $\{c_0, d_0, \tau_0\}$. The resulting nominal DOA is given by

$$\theta_0 = \theta(c_0, d_0, \tau_0) \quad \text{Eq 3.13}$$

At first, each parameter is separately contaminated by errors. In a second approach, all parameters are supposed noisy, which implies the introduction of a multi-variable Taylor development.

If we consider that the array geometry and the speed of sound are precisely known ($\delta d=0$ and $\delta c=0$), the error on the DOA is only due to the imprecision on the TDE and can be expressed by

$$\delta\theta = \theta(c_0, d_0, \tau_0 + \delta\tau) - \theta_0 = \sum_{n=1}^{\infty} \left\{ \frac{(\delta\tau)^n}{n!} \cdot \frac{\partial^n \theta}{\partial \tau^n} \right\}_{\tau=\tau_0} \quad \text{Eq 3.14}$$

When calculating the first terms of the development, the error is given by

$$\begin{aligned} \delta\theta = & \frac{c}{d} \frac{\delta\tau}{\left(1 - \left(\frac{\tau_0 c}{d}\right)^2\right)^{3/2}} + \frac{1}{2} \left(\frac{c}{d}\right)^3 \frac{\tau_0 (\delta\tau)^2}{\left(1 - \left(\frac{\tau_0 c}{d}\right)^2\right)^{5/2}} + \frac{1}{6} \left[3 \left(\frac{c}{d}\right)^5 \frac{\tau_0^2 (\delta\tau)^3}{\left(1 - \left(\frac{\tau_0 c}{d}\right)^2\right)^{7/2}} + \left(\frac{c}{d}\right)^3 \frac{1}{\left(1 - \left(\frac{\tau_0 c}{d}\right)^2\right)^{3/2}} \right] \\ & + \frac{1}{24} \left[15 \left(\frac{c}{d}\right)^7 \frac{\tau_0^3 (\delta\tau)^4}{\left(1 - \left(\frac{\tau_0 c}{d}\right)^2\right)^{9/2}} + 9 \left(\frac{c}{d}\right)^5 \frac{\tau_0}{\left(1 - \left(\frac{\tau_0 c}{d}\right)^2\right)^{5/2}} \right] + \dots \end{aligned} \quad \text{Eq 3.15}$$

The determination of the upper limit of the error on the DOA is very important to evaluate the overall performance. If we admit that the precision of the TDE is better than 5% of the maximum lag (physically expectable $\tau_{max}=d_0/c_0$), then we can calculate the DOA error $\delta\theta$ as a function of the nominal

DOA θ_0 . The next figure presents the mathematical results described by Eq 3.15 compared with a statistical approach (Figure 3.17). Indeed, by simulating noisy TDE and by calculating the final DOA error over thousands of attempts, the statistically estimated errors on the DOA present an upper limit theoretically identical to the mathematical approach. The problem is expressed as:

- find $\delta\theta = f(\delta\tau)$
- with $d_0=1m, \delta d=0, c_0=342ms^{-1}, \delta c=0$
- for $\theta_0 \in [0, 90^\circ], \delta\tau \in [-0.05 d_0/c_0, 0.05 d_0/c_0]$

For reasons of symmetry, the region $\theta \in [0, 90^\circ]$ is sufficient to describe all the phenomena.

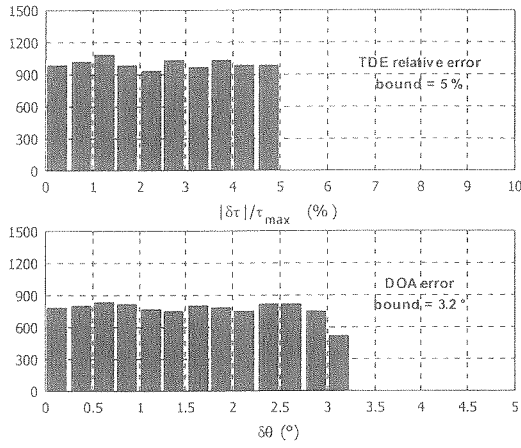


Figure 3.17 : Histogram of TDE errors distribution for $|\delta\tau| < 0.05 \tau_{max}$, histogram of the correspondent DOA error ($\theta_0=0^\circ$)

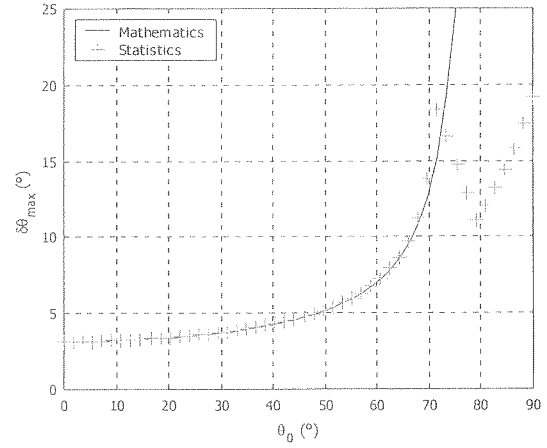


Figure 3.18 : DOA error bound as a function of the DOA angle θ_0 for $\delta d=0, \delta c=0, |\delta\tau| < 0.05 \tau_{max}$

The analysis of Figure 3.18 reveals that the goniometry for sources located in the region around the Broadside direction (frontal), performs much better than for sources located in the End-Fire region (lateral). In other terms, the DOA sensibility to TDE errors is much greater for sources aligned with the baseline. The DOA performances remain acceptable for a DOA between -50° and 50° , and decrease seriously beyond to reach a maximum value of 20° for $\theta_0=90^\circ$. The saturation of the errors between 70° and 90° observed in the statistical approach, is due to elimination of goniometry resulting in complex DOA ($\sin(\theta) > 1$). The complex DOA values, corresponding to TDE greater than the maximum physical time delay, are set equal to 90° . The mathematical approach does not take this physical limitation into account. Finally, the slight differences observed around $\theta_0=70^\circ$ are due to finite length of the Taylor series expansion used for the mathematical model (Order 4).

A similar development can be carried out in case of inaccuracy either on the speed of sound or on the sensor location (see Figure 3.19 and Figure 3.20). Finally, these three parameters influence the DOA errors in quite a similar fashion. Yet, an important difference is observed for the Broadside direction: in the particular case of $\theta_0=0^\circ$, errors on the speed of sound and sensor location do not have any influence on the DOA ($\delta\theta=0$).

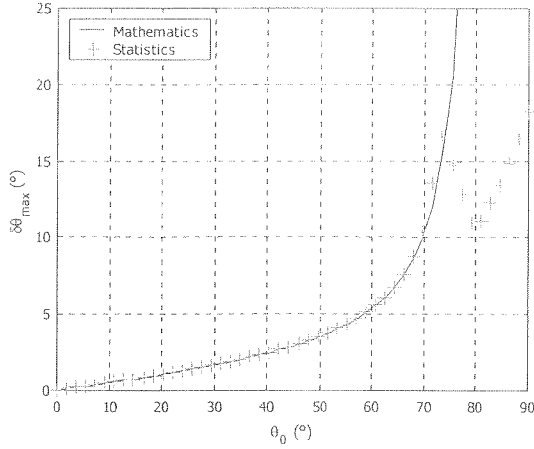


Figure 3.19 : DOA error bound as a function of the DOA for $\delta d=0$, $|\delta c| < 17.1 \text{ ms}^{-1} (0.05 \cdot c_0)$, $\delta \tau = 0$

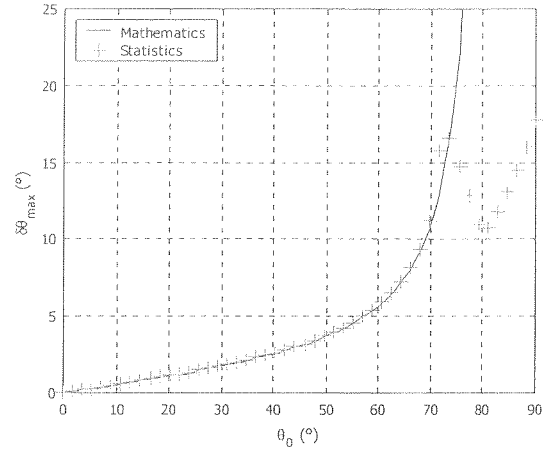


Figure 3.20 : DOA error bound as a function of the DOA for $|\delta d| < 5 \text{ cm} (0.05 \cdot d_0)$, $\delta c = 0$, $\delta \tau = 0$

In the second step, all the parameters are contaminated by noise (Figure 3.21). The mathematical error bound is obtained by calculating the three-variable Taylor series expansion given by

$$\delta\theta = \theta(\tau_0 + \delta\tau, c_0 + \delta c, d_0 + \delta d) - \theta_0 = \sum_{j=1}^{\infty} \frac{1}{j!} \left\{ \left(\delta\tau \frac{\partial}{\partial \tau} + \delta c \frac{\partial}{\partial c} + \delta d \frac{\partial}{\partial d} \right)^j \theta(\tau, c, d) \right\}_{\tau=\tau_0, c=c_0, d=d_0} \quad \text{Eq 3.16}$$

When all the parameters are noisy, the overall influence on the DOA error is more than the sum of the separated contributions. As the variables are closely linked (Eq 3.12) cross terms have to be considered.

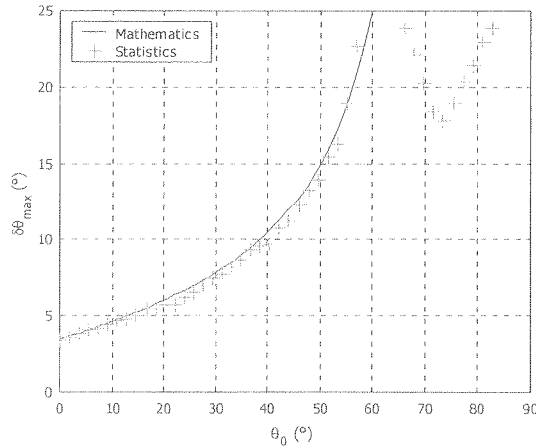


Figure 3.21 : Upper limit of DOA errors as a function of the DOA for $|\delta d| < 5 \text{ cm} (0.05 \cdot d_0)$, $|\delta c| < 17.1 \text{ ms}^{-1} (0.05 \cdot c_0)$, $|\delta \tau| < 0.15 \text{ ms} (0.05 \cdot d_0/c_0)$

When performing a two-sensor localization, it appears clearly that the performances fall when the DOA diverges from the Broadside direction. In the case of antenna with more than 2 sensors, the goniometer should be considered as a combination of several sensor pairs with different behaviors.

3.3.2 Antenna geometry and localization errors

The 3D localization requires at least four sensors located in 3D space (Section 2.5). By comparison with the two-sensor case, it is easy to deduce that the localization performances will differ according to the antenna geometry and the DOA. In order to quantify the performance disparities, the singular value decomposition of the relative sensor position matrix is performed. The resulting three-dimensional subspace represents the intrinsic antenna geometry. When the singular values are equal, the antenna presents “revolution symmetry”, denoting an isotropic approach. The DOA errors are almost independent of the DOA. The Tetrahedral or the Cube with adequate baseline selection presents this quality. If this condition is not fulfilled, the DOA performances exhibit disparities in relation to the singular values range. For example, the DOA error bound was calculated for every direction with a four-sensor cube base antenna (Figure 3.22). The relative bound errors are set to $|\delta d|/d_{max} < 0.05$, $|\delta \tau|/\tau_{max} < 0.05$ and the localization is performed with all six baselines.

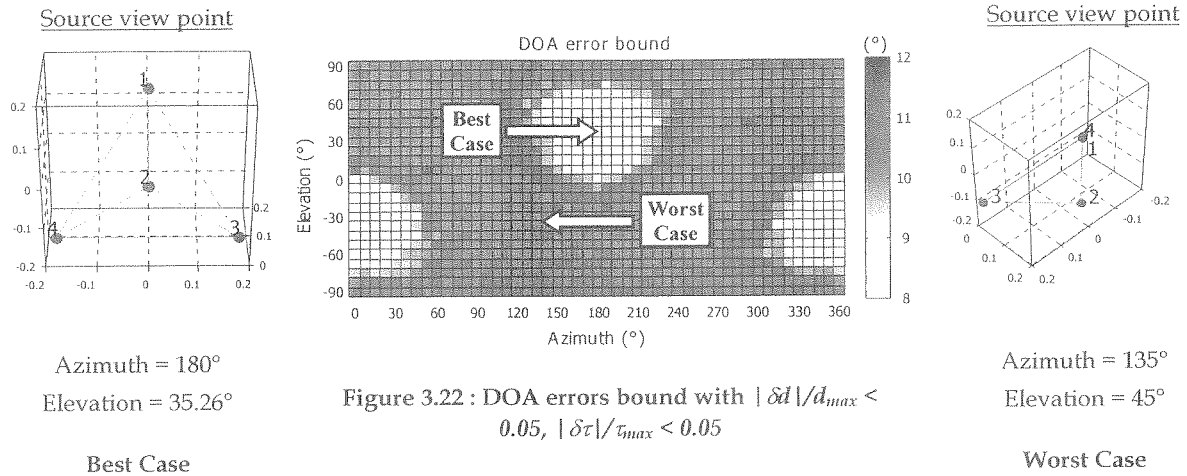


Figure 3.22 : DOA errors bound with $|\delta d|/d_{max} < 0.05$, $|\delta \tau|/\tau_{max} < 0.05$

The best cases correspond to the DOA presenting the lowest DOA error bound: the direction with azimuth = 180° and elevation = 35.26° is one optimum direction. From the source point of view, the antenna has its maximum of extension (left figure). The worst case can be observed, for example, in the DOA with azimuth = 135° and elevation = 45°, where the antenna shows the smallest extension (see right figure). The performance disparities are, as a first approximation, equal to the ratio between the highest and lowest singular values. In this case, the singular values are [0.5 0.5 0.25] and the ratio equals 2.

In order to facilitate the 3D localization, the DOA is usually transformed in azimuth and elevation components (Figure 3.23) as referenced in Eq 2.41. The interpretation of the azimuthal projection of the DOA error requires some precautions. When the elevation increases, the impact of DOA error on the azimuth errors is multiplied. For elevation closed to $\pm 90^\circ$ (Poles), the azimuth means nothing anymore. For this reason, the corresponding DOA was removed from the plots.

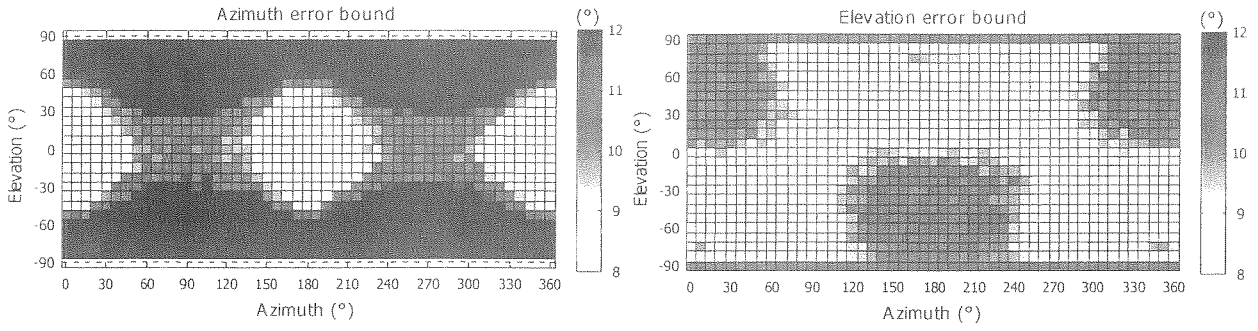


Figure 3.23 : DOA error bound in terms of azimuth and elevation ($|\delta d|/d_{max} < 0.05$, $|\delta \tau|/\tau_{max} < 0.05$)

3.3.3 Influence of the speed of sound estimation

Despite the fact that the celerity is essential to the knowledge of the sound field, calculations show that the DOA can be totally independent of estimation errors on the speed of sound. This requires the array to be composed of at least 4 microphones located in 3-D space (dimension of the subspace defined by the array equal to three). As an example, it is demonstrated in annex 7.4, that the errors on the azimuth are independent of the estimation of speed of sound. Similar argumentation can be established for the elevation.

Yet, a good estimation of the speed of sound is essential for the Detection module to perform well. Indeed, the norm criterion, defined in Eq 2.44, which permits to select “physically rational combinations”, is directly contaminated by speed of sound estimation errors. If the estimation quality is poor or the propagation conditions (atmospheric pressure, temperature, salinity) vary too much, a delay combination can be wrongly eliminated due to excessive wave vector norm. A solution to overcome this difficulty is to estimate the speed of sound via a calibrating active goniometry. The speed of sound is adjusted in such a way that the norm of any measured wave vector is equal to unity. In practice, due to other parameters inflowing onto the norm criterion, the speed of sound chosen is the one minimizing the distance between the wave vector norm and unity. To avoid favoring any direction, at least three source positions located in 3D space are needed to perform a relevant speed of sound measurement and to calibrate the goniometer.

3.3.4 Influence of the sensors position estimation

In section 3.3.1, it was demonstrated that the DOA error varies as a function of the DOA when the relative position of the sensors are contaminated with noise. In order to perform the same analysis for a complex 3D geometry antenna, Monte Carlo simulations were implemented to quantify the influence of the positioning precision on the DOA errors.

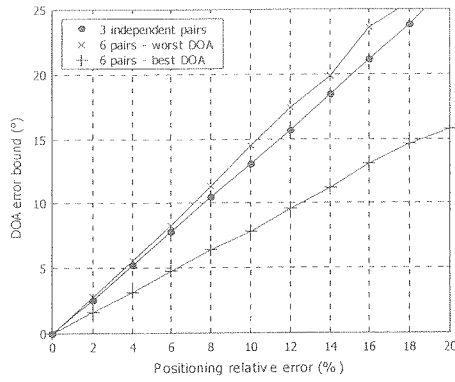


Figure 3.24 : DOA error bound in the presence of sensors position relative error (4 sensors cubic base antenna)

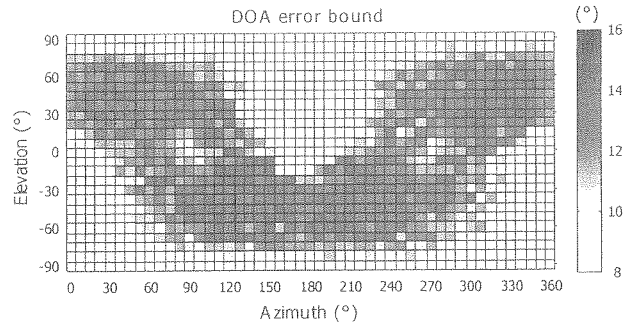


Figure 3.25 : DOA error bound in the presence of sensors position relative error (4 sensors cubic base antenna – 6 pairs) $|\delta d|/d_{max} < 0.1$

The simulations are carried out with the 4 sensor cubic base antenna. Three configurations were investigated (see Figure 3.24): the first performs the localization by using the 3 baselines of the same length (referred in the legend as “3 independent pairs”), the second and third are using all 6 baselines in the best case DOA and in the worst case DOA defined in section 3.3.2. The main remark is that the use of all baselines can reduce performance in some DOAs (Figure 3.25). The goniometry, which is almost DOA independent in the “3 pairs” localization (identical singular values), presents performance disparities when increasing the number of TDE. According to the DOA area to cover, extra precision can be obtained by increasing computation.

The origins of the positioning errors are multiple. For example, when performing infrasound localization, the sensors positions are measured with differential GPS. The inaccuracies are coming from the GPS precision, the measurement precision and from the estimation of the acoustic center. Other causes can be mechanical constraints or wind on the antenna structure (i.e. Tetrahedral antenna on the Silence Light mast). In this application, distinction has to be made between positioning errors inside the antenna, inducing errors in the relative position matrix and antenna displacement (i.e. mast movement). When the entire antenna is moving, the algorithm goniometry is not affected (norm criterion = 1) but the final result is biased. One way to detect such phenomena is to observe the DOA time evolution, particularly azimuth and elevation oscillations with few degrees of amplitude and frequency below 1 Hz.

3.3.5 Influence of the Time Delay Estimation

The influence of TDE errors on the localization is very close to the positioning errors effect, in terms of sensitivity and in terms of performance difference, according to the antenna subspace singular value disparities (Figure 3.26 and Figure 3.27).

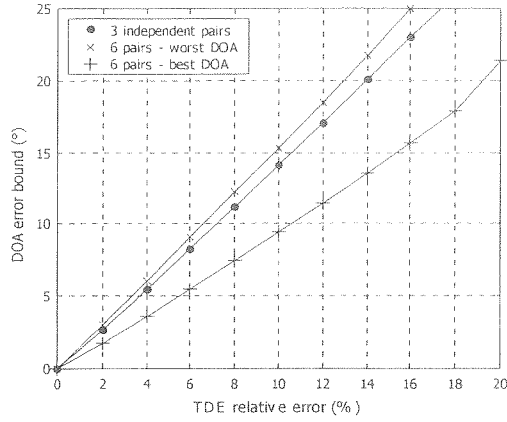


Figure 3.26 : DOA error bound in the presence of TDE relative error (4 sensors cubic base antenna)

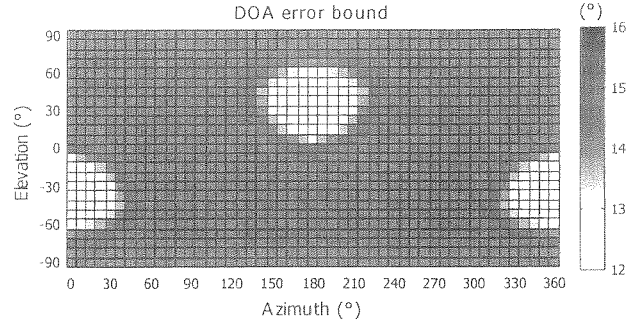


Figure 3.27 : DOA error bound in the presence of TDE relative error (4 sensors cubic base antenna)
 $|\delta\tau|/\tau_{max} < 0.1$

3.3.6 Plane wave assumption

Definition of the phenomena encountered

So far, developments were considered under the assumption that the source was sufficiently distant from the antenna, to be seen under the same angle from each sensor. In order to exhibit the induced errors on the localization, the near-field propagation is compared to the assumed far-field propagation in a geometrical approach. Then, simulations quantify the far-field assumption influence on the DOA.

Investigations have brought to light that the localization, assuming far-field propagation, deteriorates due to two successive distortions. The first is related to the aperture of the baseline when calculating the TDE: each sensor sees the source from a different direction. This introduces a DOA error quantified by the *distortion angle*. The second is related to the antenna aperture: each TDE is estimated from different observation points, which differ from the antenna phase center. These errors are referred to as the *observation point spreading*.

Errors related to the distortion angles

Considering a 3D localization with a unique sensor pair, the delay estimated by the TDE module enables us to calculate the DOA angle θ . Assuming the far-field propagation, the potential source directions are situated on a cone around the baseline (Figure 3.28). The direction locus corresponds unambiguously to a unique DOA θ and a unique TDE. If the potential locations of the source are situated in the vicinity of the antenna, the cone model has to be replaced by a hyperboloid as shown in Figure 3.29. All locations on the hyperboloid correspond to the same TDE.

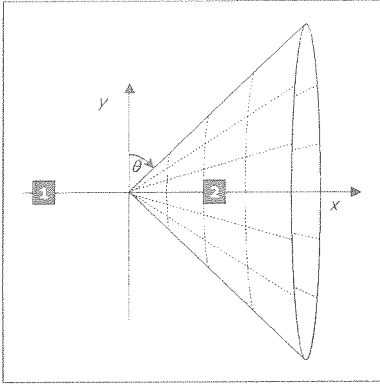


Figure 3.28 : Locus of potential source directions corresponding to τ_{12} under the plane wave assumption

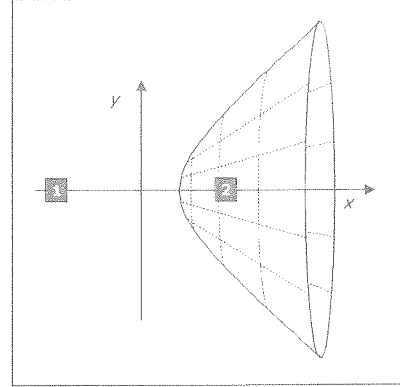


Figure 3.29 : Locus of potential source locations corresponding to τ_{12} under the spherical wave assumption

When looking in the plan xy , the locus defined by a constant TDE, which corresponds to a constant path difference, is a hyperbola, the focus of which are the sensors (Figure 3.30). The locus of potential locations, defined by the TDE τ_{12} , is described by the equation

$$|\vec{x}_{2s}| - |\vec{x}_{1s}| = c \cdot \tau_{12} \quad \text{Eq 3.17}$$

All locations situated on the locus are defined by different DOA angles but the same TDE.

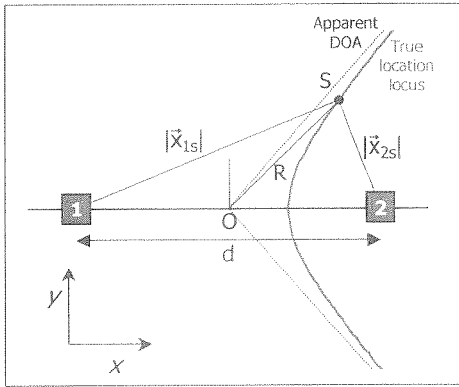


Figure 3.30 : Locus of potential source position (hyperbola), inter-sensor spacing d , source range R , phase center O

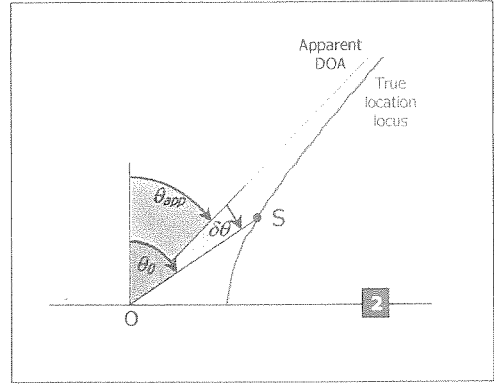


Figure 3.31 : True DOA angle θ_0 , apparent DOA angle θ_{app} and distortion angle $\delta\theta$

The distortion angle $\delta\theta = |\theta_0 - \theta_{app}|$, induced when assuming far-field propagation, is defined as the difference between the apparent DOA and the true DOA (Figure 3.31). When geometrically analyzing the distortion angles for different DOA angles θ_0 , it appears that, for the Broadside and End-fire directions, the hyperbola degenerates into its asymptotes, causing the distortion angle to be null. The general case was studied in [7] and reveals that the worst case is found for DOA $\theta_0 = 45^\circ$. The distortion angle can be approximated by

$$\delta\theta_{\{\theta_0=45^\circ\}} \cong \left(\frac{d}{4R} \right)^2 \quad \text{Eq 3.18}$$

where $d=|\vec{x}_{12}|$ is the inter-sensor distance and $R=|\vec{x}_S|$ the source range. As the source range R increases, the hyperbola tends to its asymptote and $\delta\theta \rightarrow 0$. For example, the distortion angle is about 4° when the source range is the same order of magnitude of the sensors separation and is less than a ten of a degree when the range reach $R = 6d$. Simulations corroborate the approximation function for relative range beyond $\frac{1}{2}$ (Figure 3.32). Below, simplification hypotheses used for the approximation are not fulfilled.

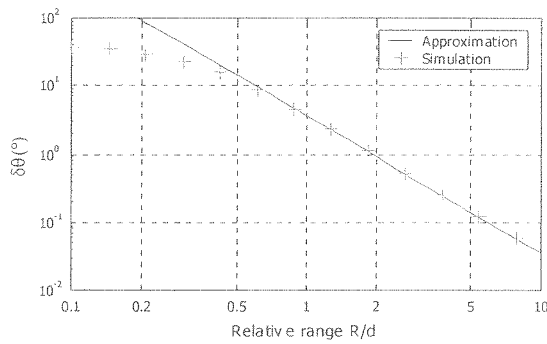


Figure 3.32 : Distortion angle assuming far-field propagation - worst case ($\theta_0=45^\circ$)

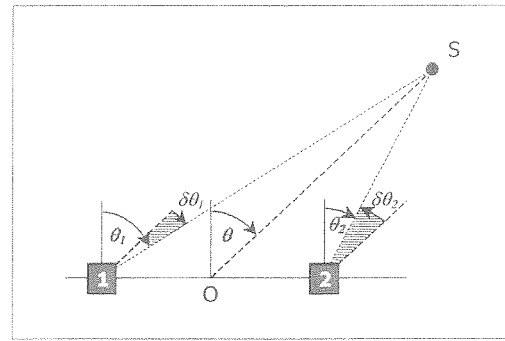


Figure 3.33 : Different directions of look across the baseline

A second way to understand the origin of the distortion angles is to observe the source from the different sensor viewpoints (Figure 3.33). The DOA angle θ , defined at the baseline phase center O , can be seen as an “average” DOA seen from the two baseline extremities. The differences between the DOA angle θ and the angle viewed from the sensor defined by $\{\delta\theta_1=\theta_1-\theta, \delta\theta_2=\theta_2-\theta\}$, are directly related to the distortion angle. When these differences are equal ($|\delta\theta_1|=|\delta\theta_2|$), as encountered in Broadside and End-fire region, the two different contributions tend to cancel each other out and the “average” DOA corresponds to the true DOA. As the discrepancy between $|\delta\theta_1|$ and $|\delta\theta_2|$ increases, the calculated average DOA, assuming far-field assumption, diverges from the true DOA and the distortion angle increases. The maximum disparity is observed for $\theta_0=45^\circ$ as predicted by the theory.

Up to now, a unique baseline has been considered. In the case of localization using an antenna (multiple TDE), the distortion angle is reported on each baseline. The way that the different distortion angles are combined varies with the DOA. According to the source location, it can appear that the distortion angles compensate and induce no distortion at all. To clarify the properties that allow such compensation, a six-sensor 3D cross antenna was used to localize a source, located in its vicinity, assuming far-field propagation. Indeed, the 3D cross antenna presents the particular characteristic that

the middle points of every sensor branch are located at the antenna phase center (Figure 3.34). Thus, no errors are introduced due to antenna observation points spreading, as discussed in the next section. With a same approach as presented in previous sections (3.3.3, 3.3.4, 3.3.5), the overall distortion angle is calculated for every DOA. The results are presented both in a planar plot (Figure 3.37) and in a 3D polar plot (Figure 3.35). This type of representation is the same as used to represent 3D directivity pattern. Each point of the surface is defined by 3D coordinates that correspond to a {azimuth, elevation} set and by a distance to the origin equal to the investigated error. In order to facilitate comprehension, the distance to the origin is corroborated by the surface color.

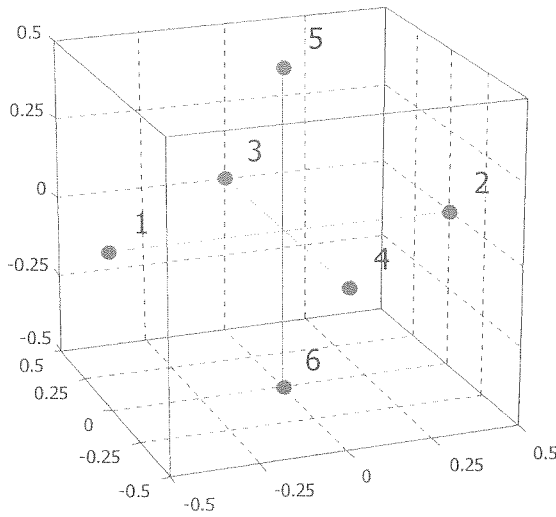


Figure 3.34 : Six-sensor 3D cross antenna

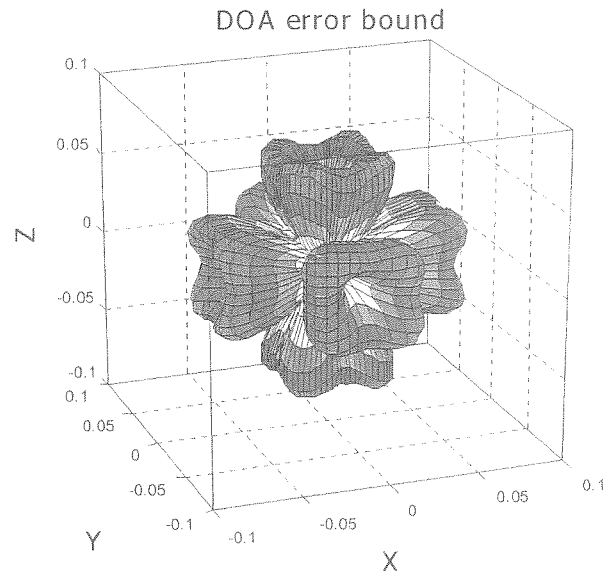


Figure 3.35: Overall distortion angle as a function of the DOA (source relative range $R/d=5$)

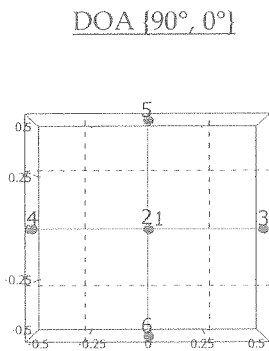


Figure 3.36 : Best case source viewpoint

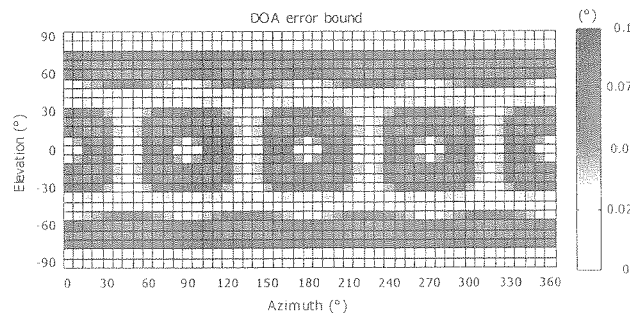


Figure 3.37 : Overall distortion angle as a function of the DOA (source relative range $R/d=5$)

DOA $\{225^\circ, 35.26^\circ\}$

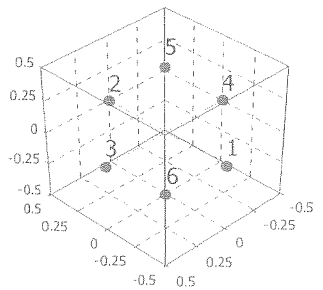


Figure 3.38 : Best case source viewpoint

Figure 3.36 shows the antenna from the source viewpoint. In this configuration, each baseline sees the source in its Broadside or End-fire region, so that no distortion is induced. Figure 3.38 presents one of

the special DOAs for which the different distortion errors compensate each other and cause the overall distortion angle to be null. The required condition is that the baselines present revolution symmetry around the axis connecting the antenna phase center to the source. Due to the symmetry in the antenna geometry, the first condition is observed for six DOAs, the second for height directions.

Errors related to the observation point spreading

In addition to the distortion angles that affect each baseline, the spreading of the acoustic phase centers (observation points) of each baseline around the antenna phase center (defined by Eq 2.31) introduces extra localization errors. In the case of long-range sources, the DOA does not vary from sensor to sensor. Each baseline sees the source under the same DOA angle. To the contrary, for close sources, the apparent DOAs differ across the antenna. As presented in Figure 3.39 in a 2D case, each baseline apparent DOAs $\{DOA_{12}, DOA_{13}\}$ are referenced to their own acoustic phase centers $\{O_{12}, O_{13}\}$, which differ from the antenna phase center O .

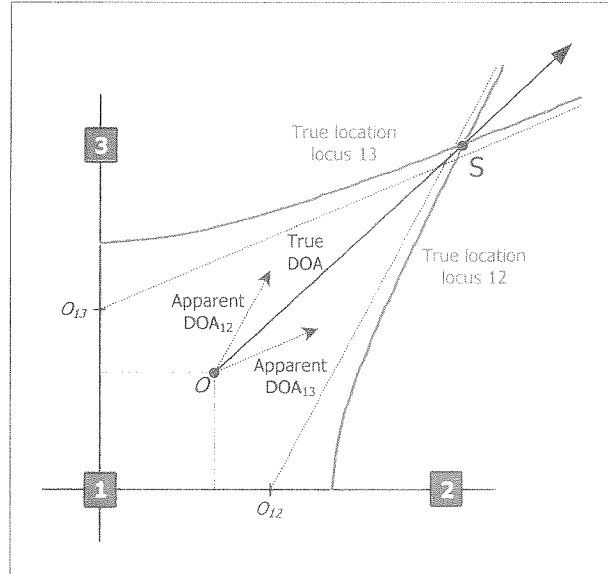


Figure 3.39 : Apparent DOA angles across the antenna

This scheme clearly shows that the order of magnitude of the errors, due to the observation points spreading, is much more important than the baseline distortion angle. As shown in Figure 3.41, the difference between the apparent DOA angles reach 5° for $R/d=10$.

In the same approach than for the baseline distortion angle, the DOA estimation given by the localization module can be seen as an "average" DOA over the antenna. Disparities in the apparent DOA induce localization errors. The figure connecting the middle of each baseline describes a sub-antenna, the extension of which accounts for the disparities in the DOA. When observing the antenna from the source viewpoint, if the sub-antenna is symmetrical around the axis OS (i.e. source located at $\theta=45^\circ$ in Figure 3.40), the different apparent DOA will be compensated to deliver a correct average value.

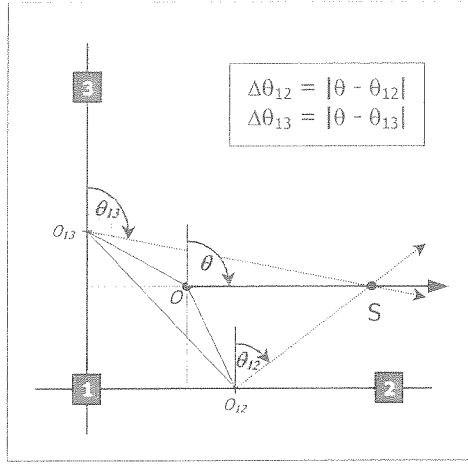


Figure 3.40 : Different DOA angles assuming a far source - worst case ($\theta_0=45^\circ$)

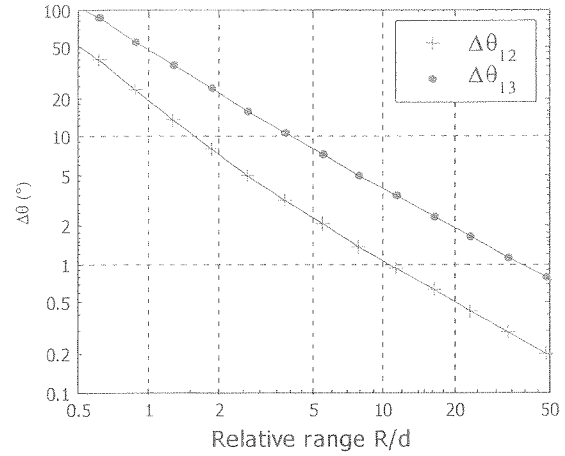


Figure 3.41 : Locus of potential source location corresponding to τ_{12} assuming a close source

The global effect of both distortion angle and observation point spreading is presented as a function of the DOA in the case of the four-sensor cube base antenna. The next figures present the DOA errors and their projections into azimuth and elevation coordinates for a source relative range $R/d=5$. One best-case DOA is observed for the DOA coordinates $\{180^\circ, 35.26^\circ\}$ (Figure 3.44). When looking at the antenna from this viewpoint, two revolution symmetries can be observed. Firstly, the observation sub-antenna presents revolution symmetry around the axis source - antenna phase center and looks like a perfect hexagon, inducing the error, due to observation point spreading, to be compensated. Secondly, the baselines present a revolution symmetry inducing the distortion errors to compensate. The global effect of the far-field assumption is null.

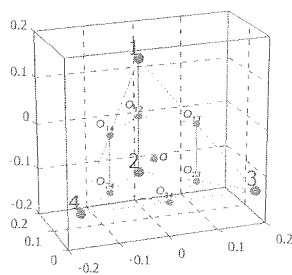


Figure 3.42 : Four-sensor cube base antenna and its observation sub-antenna

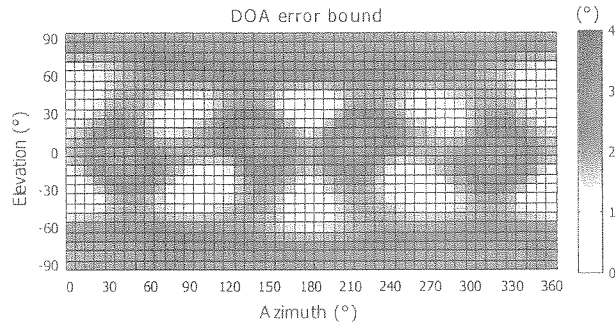


Figure 3.43 : Global distortion angle as a function of the DOA (source relative range $R/d=5$)

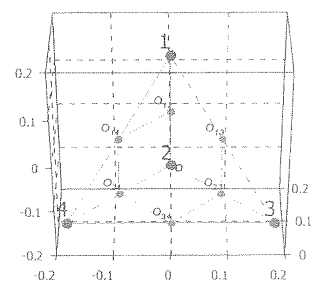


Figure 3.44 : Best case DOA $\{180^\circ, 35.26^\circ\}$

Although revolution symmetry enables us to obtain the compensation of DOA errors, axial symmetry in vertical or horizontal plan permits the errors to be compensated in respectively azimuth and elevation as observed in Figure 3.45 and Figure 3.46.

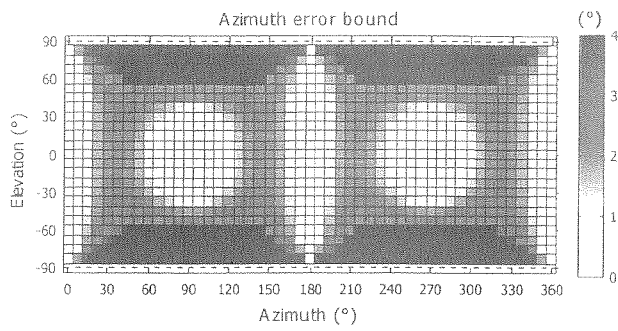


Figure 3.45 : Global distortion angle in azimuth as a function of the DOA ($R/d=5$)

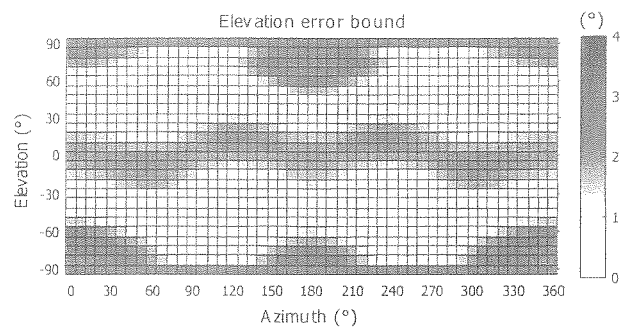


Figure 3.46 : Global distortion angle in elevation as a function of the DOA ($R/d=5$)

The close source model offers the advantages to introduce directly the source location. Investigations were carried out to perform acoustical triangulation in the vicinity of the antenna. By searching for the intersection of the hyperboloids described by the different baselines, it is possible to find the 3D source position.

Chapter 4

Antenna design

4.1 *Beamforming - DOA approaches*

The antenna design includes defining the number of sensors, the inter-sensors spacing and the geometry of the antenna. The extensive literature that can be found on the beamformer design is very helpful in the sense that the physical approach is very similar. Although the beamforming is based on a narrow-band approach, the rules and properties inherent in beamformers and goniometers present similarities, as a correctly designed beamformer will perform well in a DOA application.

In that sense, the Peak-to-Floor ratio can be seen as the counterpart of the array directivity index, as it traduces how well the process extracts the relevant information from the surrounding noise (see Annex 7.5). The DOA resolution has to be compared to the half-power angle, as it denotes how well the process discriminates two close contributions. The antenna design rules are derived from the beamforming design techniques. Yet, the advantages of the spatio-temporal approach were used to lower the frequency approach constraints. For example, the number of sensors is drastically reduced and the Nyquist spatial condition is less restraining.

4.2 *Sensor number*

In Section 2.5, it was demonstrated that four sensors distributed in 3D space are required to perform a 3D localization. Extra available baselines (linearly dependant with the three first baselines) will be used, as they enhance the localization precision. Yet, the gain in precision is obtained to the detriment

of the complexity of the detection module. Indeed, the probability of a good recombination decreases, as the baseline number increases. Thus, the number of baselines should be reduced to a minimum. If different configurations are possible, the geometry properties and the comparison of the TDE performance of each baseline should instruct the choice.

Nevertheless, other sensors can be added to increase the SNR of the cross-correlation by carrying out coherent processing (section 2.4.3). The number of sensors is then only determined by the ratio between the signal level and the incoherent Noise level defined in n_I (Eq 2.7). In a statistical approach, the cross-correlation $SNIR$ gain is related to the number of baselines that can be combined

$$G_{SNIR} = 10 \cdot \log_{10}(N_b) \quad \text{Eq 4.1}$$

For example, the theoretical gain obtained when performing coherent processing with four baselines ("Cubic antenna"), is equal to 6 dB. The argumentation is to define the operating $SNIR$ to fulfill the localization precision requirement and to deduce the baseline numbers.

4.3 Inter-sensors spacing

The determination of the antenna dimension is driven by the signal spectrum characteristics (B/f_c) and the SNR conditions. The mechanical and set-up constraints are not discussed in the section. The logical method to sharpen cross-correlation peaks and to insure good TDE precision, is to enlarge the inter-sensors spacing d . Yet, as the baseline length grows accordingly to the signal wavelength, ambiguities begin to appear in the observation window.

Figure 4.1 presents the standard deviation of the TDE error as a function of the ratio B/f_c and the inter-sensor spacing, in case of a unique source and $SNR = 0$ dB. The graph complexity denotes the difficulty to choose the spacing d that optimizes the localization and detection performances.

The vertical axis describes the signal spectrum properties. The maximum value corresponds to a Low-pass signal ($B=2f_c$), the medium values to band-pass signals and finally low ratio refers to narrow-band signals. The horizontal axis is the inter-sensors spacing to be found. For convenience, it is referenced to half the central wavelength.

Section 3.2, referring to the anomalies and ambiguities, has shown that the cross-correlation of a band-pass signal presents a direct periodicity modulated by an envelope, the period of which corresponds respectively to $1/f_c$ and $1/B$.

In a narrow-band configuration ("C" and "a,b,c" cross-correlations in Figure 4.1), the ratio $B/f_c \ll 1$ and thus the direct periodicity is preponderant. In order to avoid ambiguities, the spatial aliasing the Nyquist condition must be satisfied. When applying this criterion to the TDE, the condition

guarantees that for inter-sensor spacing below the central wavelength λ_c of the band-pass signal divided by a term including the angle θ , no ambiguities will appear in the cross-correlation.

$$d < \frac{\lambda_c}{1 + \sin(\theta)} \quad \text{Eq 4.2}$$

The angle θ is equal to 0° for Broadside direction (see Figure 3.16), and equal $\pm 90^\circ$ for End-Fire direction. Thus, End-Fire configuration is more sensitive to ambiguities, as the Nyquist frequency is two times less than in the Broadside case. When no *a priori* information on the source location is available, the condition is the most restrictive and can be written

$$\frac{d}{(\lambda_c/2)} < 1 \quad \text{Eq 4.3}$$

The transition zone between the tracking region ("Zone I") and the ambiguities region ("Zone II") corresponds to the apparition of ambiguities into the observation window (delimited by the vertical red line at $\tau = \pm 400$ smps). This transition is very abrupt as a wrong peak selection has a very strong impact on the localization precision.

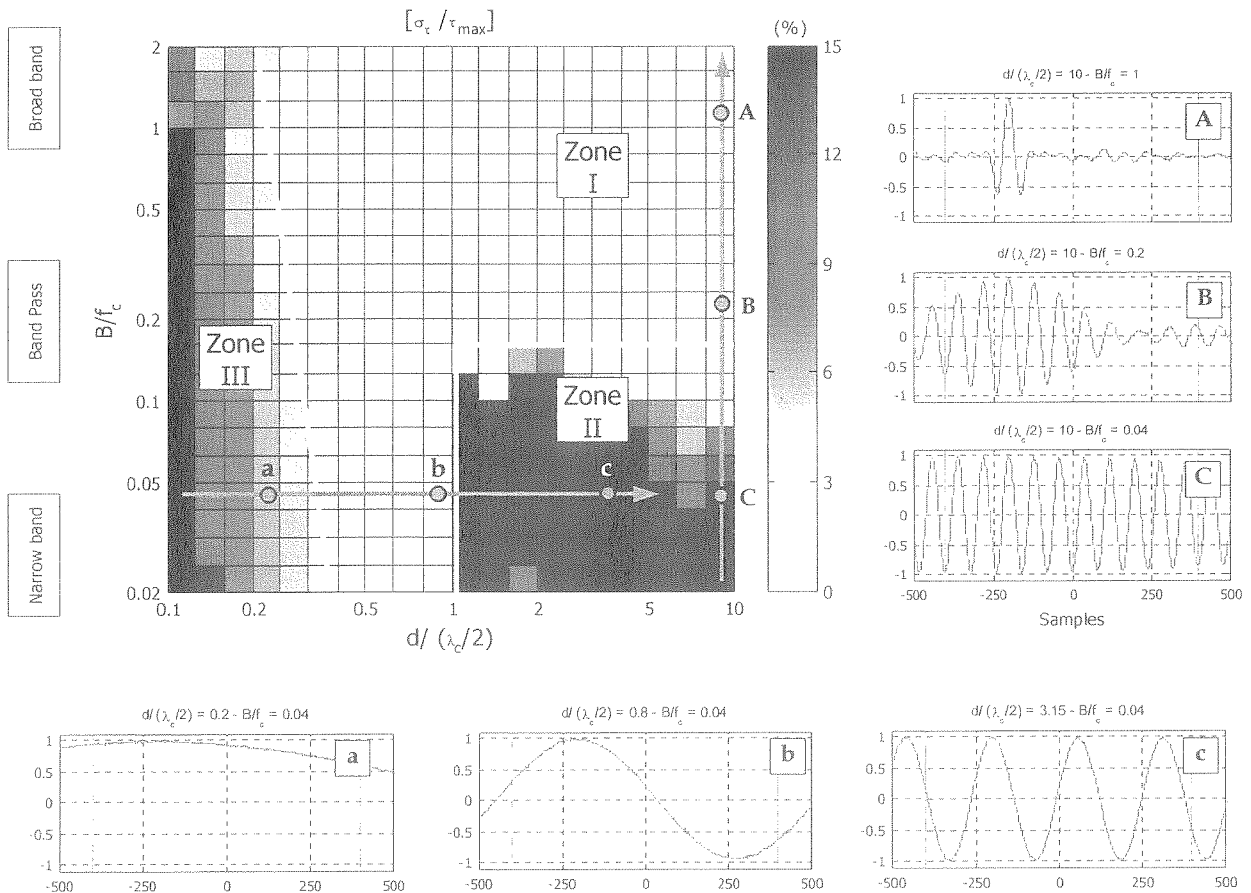


Figure 4.1 : Localization and detection performances as a function of the inter-sensor spacing and the spectrum characteristics – cross-correlations of pertinent configurations

The effect of the signal bandwidth is shown in the case of a very large inter-sensor spacing ($d = 10 \lambda_0/2$). The Nyquist criterion is absolutely not respected. In the narrowband configuration ("C"), the peak picking procedure has very little chance to select the right peak (10 peaks are situated inside the observation window). Yet, as the ratio B/f_c increases, the modulation period decreases, inducing the ambiguous peak level to decrease relatively to the true peak, as observed in the cross-correlation "B". In a Broadband configuration, the modulation is so important that the ambiguities are drowned in the cross-correlation noise ("A"). It is worth noting here that the Nyquist anti-aliasing condition can be largely violated, as far as the bandwidth is wide enough. The separation between the ambiguities and tracking region (between "C" and "B") is less abrupt than the one observed previously (between "c" and "b"). This horizontal boundary (corresponding to $B/f_c = 0.8$ at $SNR = 0$ dB) is dependant of the SNR. Decreasing SNR will induce the boundary to move toward the broadband configuration. The loss of relevant information has to be compensated by larger bandwidth.

"Zone III" is a low precision region and has to be avoided.

So far, the baselines were considered separately. Yet, the detection module, when recombining the cross-correlation peaks, is capable to reject outliers. Although the ambiguities cannot be distinguished from the true peaks when considering each TDE, the recombination criterion has demonstrated its ability to eliminate peaks corresponding to ambiguities. In practice, the recombination criterion can handle one or two ambiguities. Indeed, the norm cost function remains the only relevant criterion as the energy of the outliers peaks are similar to the true peak and as the consistency delay criterion is unhelpful to discern outliers.

In case of active goniometry, the signal bandwidth will be chosen as wide as possible to avoid ambiguities. At the same time, large inter-sensor spacing insures high localization precision. Typically, the baseline length will be chosen the largest possible with regard to the far-field assumption. The accommodation between the increasing TDE performances, due to large observation window and the decreasing localization performances due to far-field assumption, defines the best inter-sensor spacing.

The confrontation of the configuration of the different applications undertaken and Figure 4.1 summarize the performances of the different goniometers in relation with the source to track. Table 4.1 presents the relevant characteristics of both goniometer and source. The last two colons correspond to the extreme values plotted in Figure 4.2.

Most of the applications deal with low-pass signals. As the performances increase with respect to the inter-sensors spacing, large antennas will be preferred. The active localization presents the best theoretical performances (top - right of the graph). On the opposite side, the localization of the helicopter (narrow band signal around 17 Hz) failed when performed by the Echo Star antenna, as too many ambiguities appeared in the observation window.

	Antenna	d (m)	Source	B (Hz)	f_c (Hz)	$\lambda_c = c/f_c$ (m)	B/f_c	$d/(\lambda_c/2)$
Infrasound	Echo Star	20 - 35	Avalanche	5 - 10	5 - 10	32 - 64	0.5 - 2	0.6 - 2.2
	Echo Star	20 - 35	Helicopter	0.5	16 - 19	17 - 19	0.02 - 0.03	2.1 - 4.1
	Echo Star	20 - 35	Concorde	4	2	160	2	0.25 - 0.4
	Half-cross	50 - 70	Avalanche	5 - 10	5 - 10	32 - 64	0.5 - 2	1.5 - 4.4
	Half-cross	50 - 70	Concorde	4	2	160	2	0.6 - 0.9
Audio	Tetrahedron	1	Helicopter	150 - 1 k	300 - 750	0.45 - 1.1	0.2 - 2	1.7 - 4.4
	Tetrahedron	1	Aircraft	1 k - 2 k	500 - 1 k	0.34 - 0.68	2	3 - 6
	Cube	0.25 - 0.35	Aircraft	1 k - 2 k	500 - 1 k	0.34 - 0.68	2	0.7 - 2
	Cube	0.25 - 0.35	MLS	16 k	8 k	0.04	2	12 - 17
Ultra sound	Equilateral triangle	0.05	Chirp	10 k	25 - 45 k	0.03 - 0.06	0.2 - 0.4	1.6 - 3.3

Table 4.1 : Model characteristics

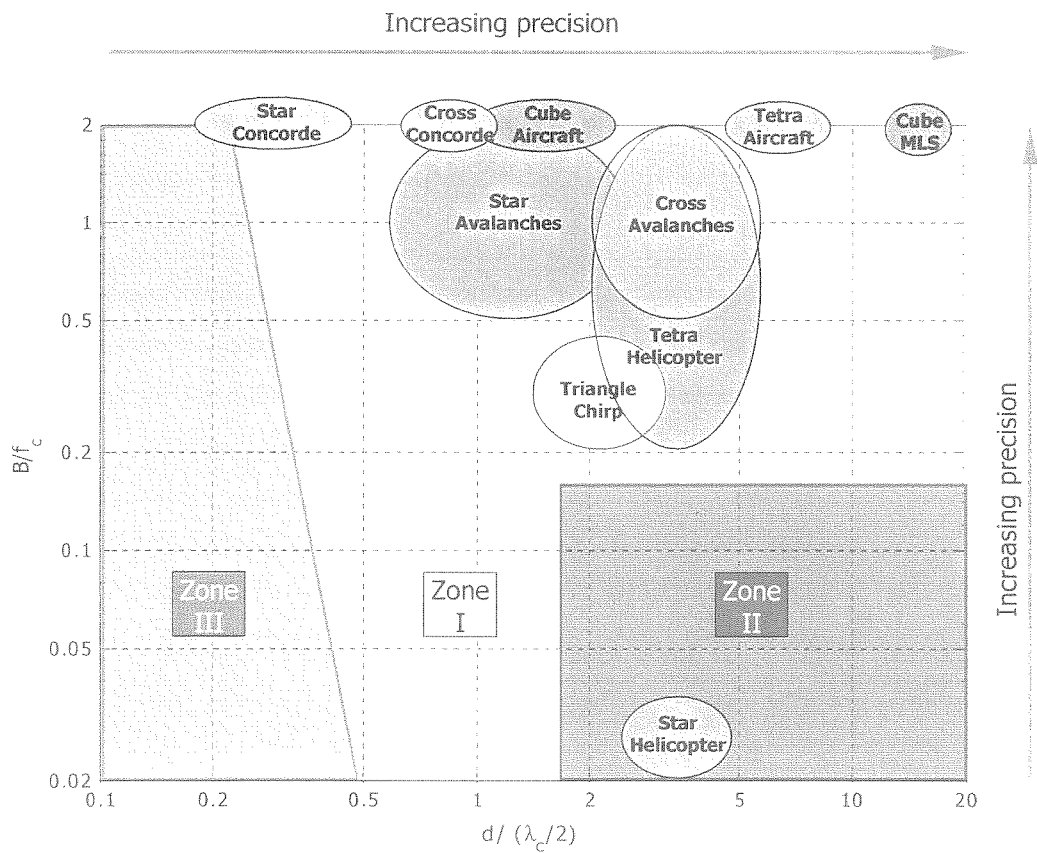


Figure 4.2 : Superposition of the performance graph and the application operational configuration (antenna and signal characteristics)

4.4 Antenna geometry

The determination of the antenna geometry is driven by the source – sensor configuration and, more precisely, by the solid angle to cover: indeed, the antenna geometry has to be designed in such a way that the DOA performances are independent of the DOA inside the operating region. The antenna geometry takes place in the localization equation (Eq 2.39) through the inverse relative position matrix \mathcal{D} . Thus, the subspace defined by the sensor through \mathcal{D} (or D) contains the entire geometry information.

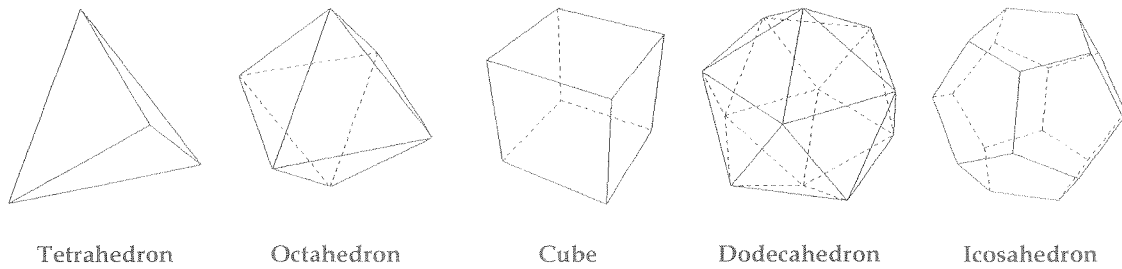
In the case of a full 3D localization, as for the Spatial Echogram application (Section 5.4), no direction should be privileged. This requires that the antenna spatial extension, observed from any direction, is identical. From a mathematical point of view, the range of the singular values of \mathcal{D} reflects the isotropic properties of the antenna. Small disparities in singular values traduce good isotropy; large disparities induce DOA dependent performances and privileged directions.

The commonly used estimator of the singular values disparities is the condition number defined by

$$\kappa(\mathcal{D}) = \|\mathcal{D}\| \cdot \|\mathcal{D}^{-1}\| = \|D^{-1}\| \cdot \|D\| = \kappa(D) \quad \text{Eq 4.4}$$

The perfect isotropic case is obtained for $\kappa=1$. (i.e. a tetrahedral antenna with all baselines considered – see Table 4.2 for different geometries).

The polyhedron 3-D solids present very interesting properties in terms of spatial symmetries. The sub-class “Platonic solids” is characterized by edges (baselines) of the same length. Sorted by increasing vertices (sensors) number, the shapes are the Tetrahedron, the Octahedron, the Cube, the Dodecahedron and the Icosahedron exhibiting respectively 4, 6, 8, 12 and 20 vertices.



The spherical symmetry appears clearly in the last two shapes.

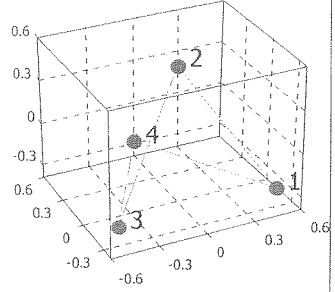
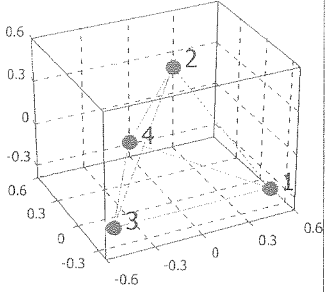
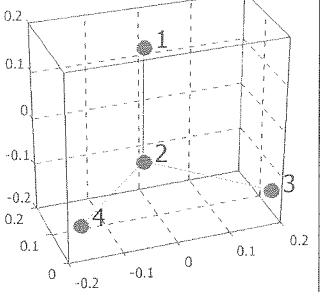
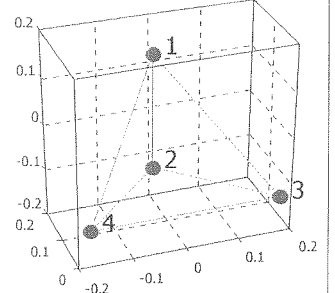
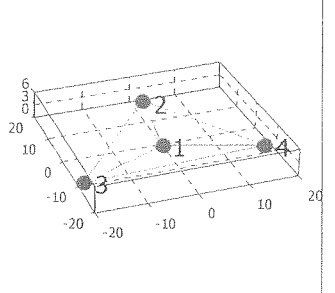
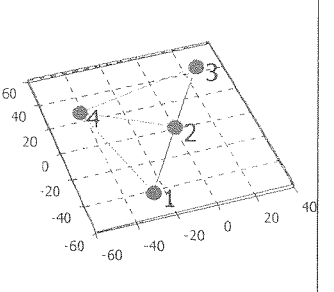
Antenna	Tetrahedral	Tetrahedral	4 sensors cubic base
Baselines	Path: 1 → 2 → 3 → 4 → 1 Pairs 1 2, 2 3, 3 4, 4 1	Full path Pairs 1 2, 1 3, 1 4, 2 3, 2 4, 3 4	3 independent pairs Pairs 2 1, 2 3, 2 4
κ	$\sqrt{2}$	1	1
3D plot (m)			
Antenna	4 sensors cubic base	Echo Star	Half cross Norsonic
Baselines	Full path Pairs 1 2, 1 3, 1 4, 2 3, 2 4, 3 4	Full path Pairs 1 2, 1 3, 1 4, 2 3, 2 4, 3 4	Full path Pairs 1 2, 1 3, 1 4, 2 3, 2 4, 3 4
κ	2	32	∞
3D plot (m)			

Table 4.2 : Conditioning number for different geometries

When the operating region can be restricted, the antenna geometry is adapted in such a way, that the performance of the localization is focalized on the region to cover. The localization precision will be enhanced by adequately orientating the antenna baselines in a Broadside configuration. The baseline length will be enlarged with respect to the observation window reduction. Indeed, the peak-picking scanning region is reduced from the plausible delay window ($\tau_{max}=d/c$) to a smaller operating window. The number of ambiguities decreases proportionally to the window reduction. The resulting drop in the false alarm rate enables us to enlarge the baselines and to gain in precision

A spatial filtering action should be added when focalizing on a restricted operating window. Indeed, in order to avoid that components coming from outside the operating window interfere with the cross-correlation function, the antenna output signals should be cleaned of these grating contributions. The main effect of the spatial filtering is to increase the SNR. It can be performed by using directional microphones or by sensor clustering.

Chapter 5

Applications

5.1 Preamble

This work was carried out in very favorable conditions, in the sense that external needs had been clearly expressed. The development of this methodological approach, that must be undertaken when handling a new goniometry application, has largely contributed to bring the right answers and solutions. The following sections summarize the essential of the developments that were performed, whilst emphasizing on the specificities of each application. The chronology of the actions has been nearly respected and corresponds to increasing frequency domains, as the first application deals with infrasounds, the second with audio signals and the last one with ultrasounds.

5.2 Infrasound goniometry

5.2.1 Background

At the LEMA's request, the GDA (Swiss Defense Procurement Agency) accepted to put at our disposal an infrasound goniometer, that was installed by the LEMA in Anzère (Central Valais) for avalanche monitoring. Prior to the LEMA action, the GDA performed goniometry for very long-range surveillance purposes. In a second step, the LEMA has successfully recorded infrasounds produced by snow avalanches (first observation in 1977 [97]). Then, the LEMA development focused on the automatic monitoring of avalanche activity, with the purpose of improving forecasting and assisting in the study of certain aspects of avalanche dynamics [1]. With the double aim of pursuing

investigations on the mechanics of the acoustic emission from avalanches and designing an automatic detection system, the LEMA developed specific instrumentation, the essential link of which is an array of infrasonic microphones part of a goniometer. Systematic measurements of the infrasonic emissions were carried out, not only of the natural and released avalanches themselves, but also of all events with the aim of characterizing the former in relation to « infrasonic noise ». The Half-cross antenna (Figure 5.1 and Figure 5.2) was designed and built by the LEMA for these tasks.

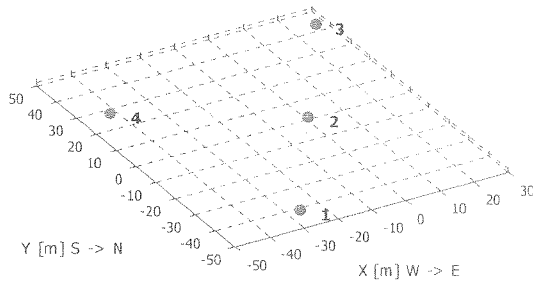


Figure 5.1 : Half-cross antenna

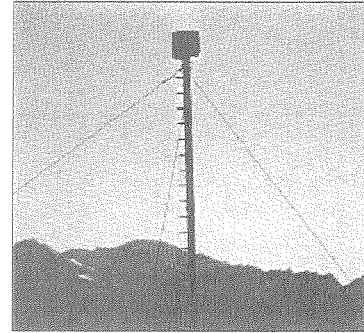


Figure 5.2 : Half-cross electrostatic measurement microphone

Finally, an exploratory goniometer was built on the basis of homemade very low frequency microphones (ECHO) placed in a Star-shape. It was dedicated to the study of the emission and the propagation of the infrasounds. Both Half-cross and Star antennas (Figure 5.3 and Figure 5.4) were developed prior to this work.

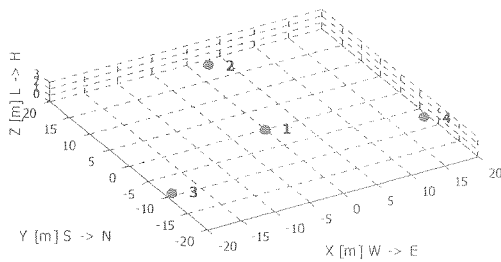


Figure 5.3 : Echo Star antenna

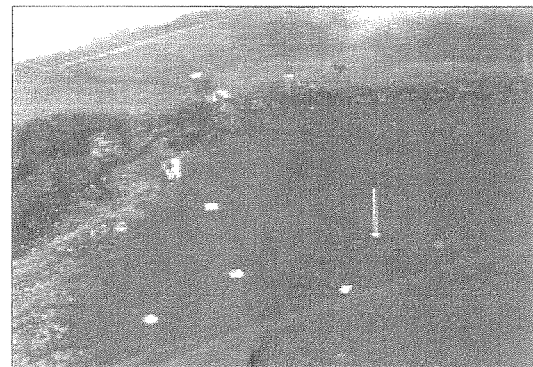


Figure 5.4 : Upper view of the Anzère Site - Echo Star antenna (white spots)

5.2.2 Foreground

The first studies aimed to characterize the specifications and performances of both antennas.

Half-cross antenna

Although the details of the algorithms were kept confidential, the basic idea of the Half-cross antenna algorithms was to perform two azimuthal goniometries by the two sub-antennas {1,2,4} and {2,3,4}

(three sensors in a triangular shape). After testing the consistency of the delays for each sub-antenna (see section 2.6.2), the azimuth results were compared for validation.

The theoretical analysis of the Half-Cross antenna reveals that localization performances are optimal in the azimuthal plan and that only a rough estimation of the elevation can be calculated (Best source-antenna configuration in the azimuthal plan = End-fire configuration). The vertical wave vector component can be calculated from the wave vector components n_x and n_y , by imposing the wave vector norm to be equal to one as expressed in

$$n_z^2 = 1 - (n_x^2 + n_y^2) \quad \text{Eq 5.1}$$

As the norm criterion is used to calculate the elevation, it cannot be used anymore to reject outliers (Detection module). Yet, the consistency criterion is helpful, although it does not take advantage of the antenna geometry information. The consequence is that the false alarm rate is much more important, since the consistency criterion is much less restrictive than the norm criterion.

The antenna Nyquist frequency, corresponding to the maximum baseline length ($d_{14}=d_{34}=70.7m$), equals 2.25 Hz. Thus, narrow band signals can be tackled without ambiguities, if their central frequencies are beyond 2.25 Hz.

Star antenna

The algorithms that control the Star antenna, were designed following the procedure developed in this work. The goniometry performances were determined from the confrontation of the snow avalanches recordings and the visual and video informations that were collected by in-situ observers. These experimental estimations of the performances corroborated the theoretical analysis (see section 3.3) that predicted localization error in azimuth to be less than 5°. In fact, this value appears to be the best estimation ever possible, as the avalanche width spread over hundreds of meter corresponding to several degrees.

Furthermore, the azimuth errors are almost unrelated with the azimuth, since the conditioning number in the horizontal plan is $\kappa=1.01$. It was also found that the elevation determination was impossible around the horizontal plan. Indeed, the global conditioning number of the Star antenna is equal to 32, which means that the localization performances in the direction perpendicular to the best plan containing the four microphones (roughly the horizontal plan), is 32 times worse than in the direction taken in the plan. This implies that around elevation equal to zero, STD errors of 2° in azimuth correspond to STD errors of 64° in elevation, which is not tolerable.

Work contributions

Several contracts financed by the GDA, the BUWAL, the Canton du Valais and the SAME European project enabled enhancements in the field of infrasound. Next table summarizes the tasks that were tackled during this work.

Avalanche activity monitoring	<ul style="list-style-type: none"> • measurement campaigns of infrasonic avalanche signatures • construction and analysis of the avalanche database (> 100 events) • determination of the acoustic center of the avalanches by confrontation between acoustic goniometry and video. • comparison of acoustic and seismic signals • implantation studies of Loetschental and Zinal sites • expert consulting for the infrasonic installation of Bonneval (F)
Propagation of infrasounds	<ul style="list-style-type: none"> • snow cover effect on infrasounds captured by buried microphones • wind effect on the infrasound localization (wave vector deviation)
Helicopter tracking	<ul style="list-style-type: none"> • feasibility study of the helicopter tracking by infrasound goniometry

Table 5.1 : Contributions brought during this work

5.2.3 Avalanche activity monitoring

Avalanche database

The characterization of an avalanche signature required four winters of recordings (1994-1998). The database, containing more than one hundred avalanches, was analyzed in order to relate the acoustic properties to the intrinsic avalanche characteristics. From this database, two avalanches artificially released and recorded in Anzère, are presented in Figure 5.5. The avalanche signatures are the two dark spread spots on the sonogram. The frequency analysis (vertical-left plot) of the avalanches exhibits higher energy in the band below 8 Hz, and the temporal analysis (horizontal-down plot) shows an increase of infrasound energy during the avalanches (around 30 s long). Competing sources are the first harmonic of the helicopter (trace from $t=45$ to 75 s) and the artificial explosions (vertical traces).

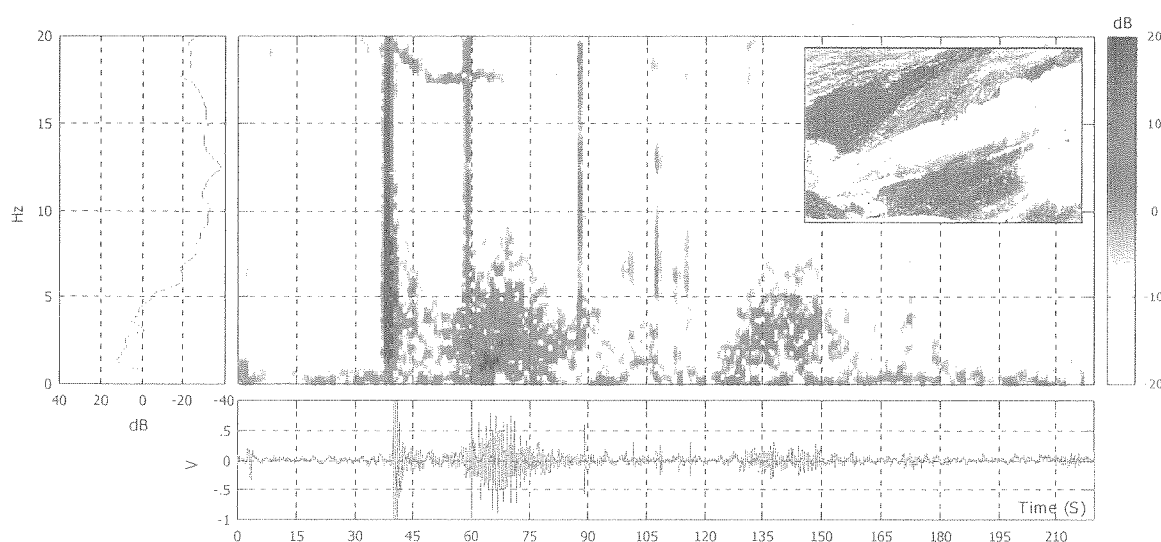


Figure 5.5 : Avalanches on "Lui du Sac" and "Tsarmettes" (16.2.97) – Vertical signatures = explosives – Horizontal signatures = helicopter first harmonic at 17.5 Hz.

The database analysis presents a unique frequency-temporal scenario. About 10 seconds after the first movement of the snow cover, the sensors record very low frequency components (< 4 Hz), then « medium » (4 – 6.3 Hz) and finally « high » frequencies (6.3 - 10 Hz). All along the flow, the spectrum is wide and full. As the avalanche slows and terminates, the acoustic energy in the high frequencies decreases, then in the medium, and finally in the low band.

It was observed that the avalanche signatures exhibited typical acoustic behavior and could be classified by sectors, as observed in the $\frac{1}{3}$ -Octave analysis presented in Figure 5.6 and Figure 5.7. The confrontation of the acoustic analysis with the topographic informations (sector slope, length, width, relative position of the sector to the antenna...) permitted to conclude that the central frequency of the signature decreases when the avalanche size grows. Therefore, wide avalanches are characterized by low central frequency (typically $f_c = 2.5$ Hz), and the smallest by central frequencies in the 5 Hz band.

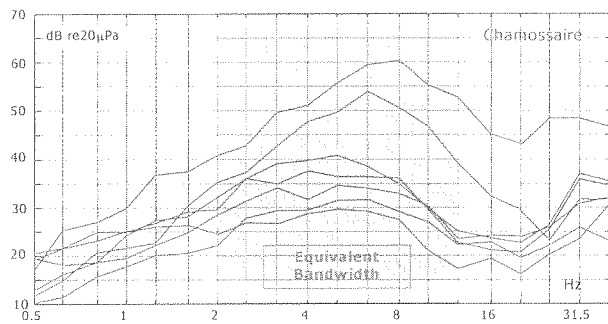


Figure 5.6 : $\frac{1}{3}$ -octave analysis of avalanches released on the sector "Chamossaire"

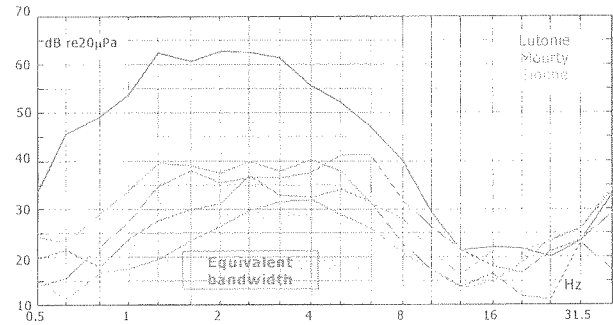


Figure 5.7 : $\frac{1}{3}$ -octave analysis of avalanches released on the sectors "Lutonie", "Mourty" and "La Sionne"

The study of the infrasound propagation has demonstrated that the specificity of each sector in terms of topography, range and percentage of direct view, implies a very local interpretation. For example, the size of avalanche can only be related to the acoustic emission, after carrying out a learning stage. A first winter is therefore necessary to collect information and to introduce the specificity of the site in the process.

The confrontation of the videos and the recorded levels showed that the factors supporting the generation of infrasound, are the speed of the front (which increases abruptly when the avalanche jumps bars of rocks) and the size of the front (estimated by the product of its width and its height). Detection is penalized when the corridors show the following characteristics: concave profiles (strong slope at the beginning, decreasing progressively) and heavy snows (spring avalanches). On the other hand, the conditions of detection are favorable in the event of continuous stiff slopes, of corridors intersected with rock bars and strong snowing up (slopes charged).

The localization of the avalanches presented in Figure 5.5 is shown below.

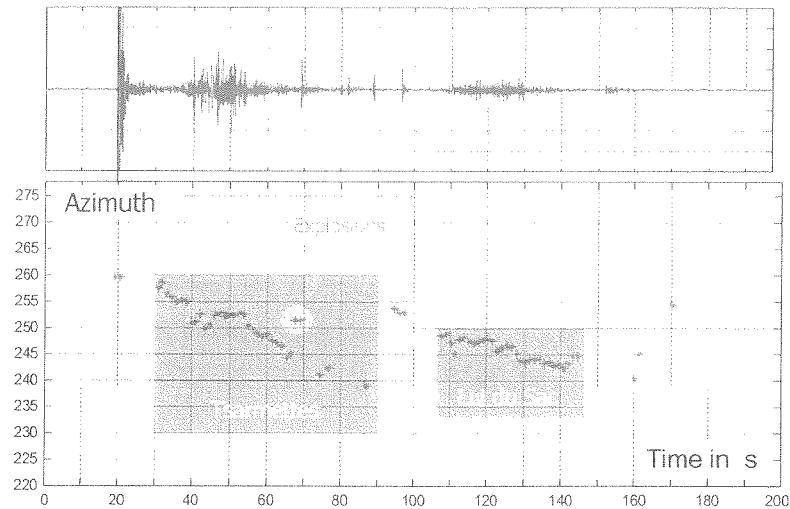


Figure 5.8 : Goniometry in the azimuthal plan of the avalanches on "Tsarmettes" and "Lui du Sac" (16.2.97)

Handling a new site

This analysis work concluded the prototyping step and the Anzère campaign. The validation step implied to choose a new site. Up to now, two candidate sites were studied: Loetschental and Zinal. The representation of the sectors to cover gives quick indications on the potential goniometer locations. Figure 5.9 presents the 3D topographical data of Zinal (VS-CH).

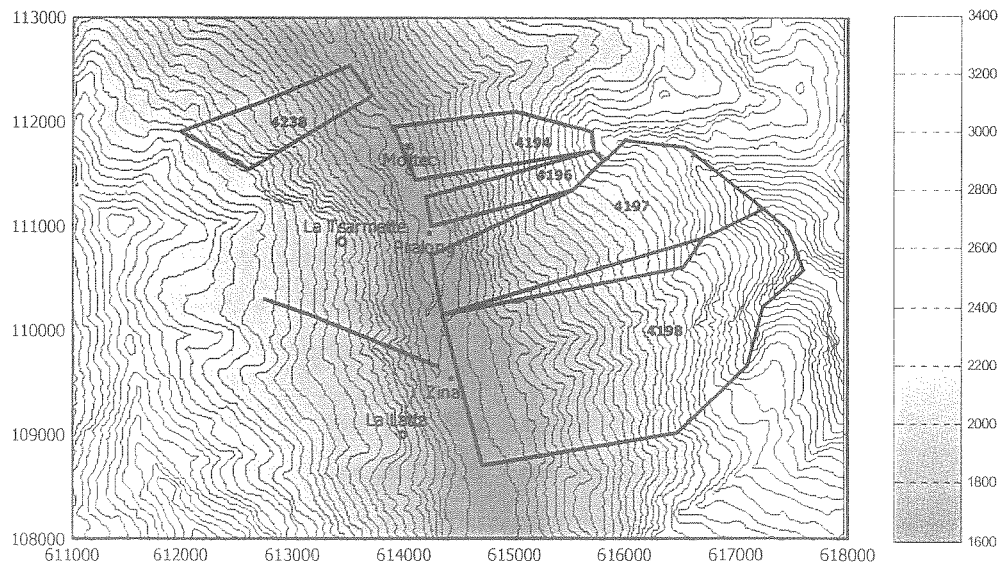


Figure 5.9 : Zinal topographical dataset

From the 3D map obtained at the Swiss Federal Office of Topography ("OFT"), the sectors can be delimited in latitude, longitude and altitude. Then, the location of the antenna installation is chosen in such a way that the goniometer can easily discriminate the sectors in azimuth. A central position

would be the optimum place to separate the sectors in azimuth. Others considerations are, among others, the exposition to wind, the radio cover, the power supply, the accessibility.

Table 5.2 presents, for the potential site “La Tsarmette”, the topographical dataset of the sectors referenced to the antenna.

	Sector	Azimuth	Elevation	Slope	Alti drop	Length
Mottec	4194	67° → 37°	14° → -30°	35°	1100 m	2000 m
	4194 starter	67° → 55°	14° → 0°	32°	500 m	800 m
	4196	72° → 70°	13° → -33°	35°	1100 m	2000 m
	4196 starter	72° → 75°	13° → 0°	32°	500 m	800 m
	4238	310° → 8°	10° → -23°	34°	700 m	1600 m
Zinal	4197	80° → 110°	16° → -26°	31°	1500 m	2900 m
	4198	95° → 135°	18° → -20°	28°	1600 m	3400 m

Table 5.2 : Topographical dataset of the site Zinal for the candidate installation location “La Tsarmette”

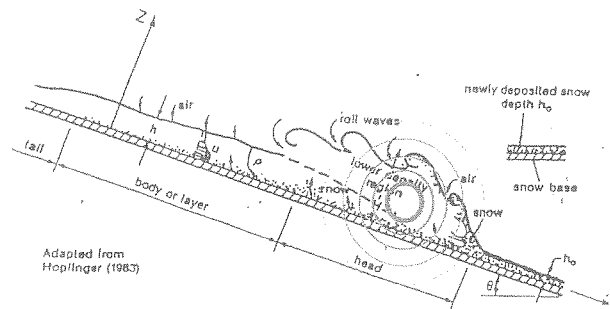


Figure 5.10 : Avalanche modeling [5] and approximate location of the acoustic center

Acoustic center localization

The goniometer has also been useful to progress in the understanding of the acoustic emission process. The acoustic center location was estimated by confronting the acoustic goniometry to the video. It appears that the center of the infrasound emission was located in the area corresponding to the penetration of the dense flow into the lower density region (Figure 5.10). Located a few tens of meters behind the front of the avalanche, this area brings into play significant masses of snow and creates zones of overpressure and depression, liable of the infrasound.

Comparison acoustic - seismic

During a joined artificial release campaign, regrouping the partners of the European project SAME (“Avalanche Mapping, model validation and warning system”), the acoustic signatures of avalanches were compared to the 3D seismic measurements (along the three axis {NS,EW,Z}).

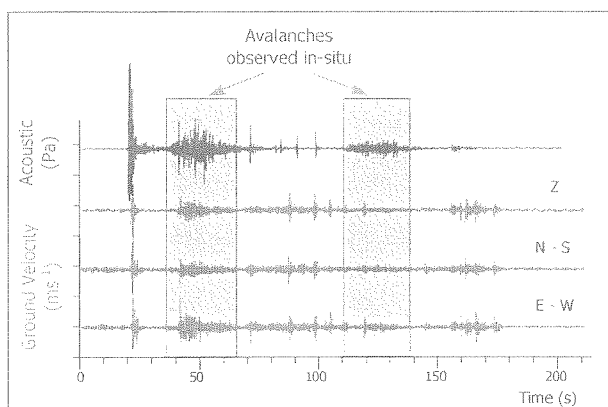


Figure 5.11 : Seismic - Acoustic avalanches signatures Tsarmettes – Lui du Sac (16.2.97)

Acoustic and seismic waveforms are very similar. The spectrum comparison reveals identical frequency components. Meanwhile, the seismic signals are far richer. For example, the seismic excitation is still observable up to 30 s after the end of the avalanche. The complexity of the seismic propagation (body waves: P-waves, S-waves; surface waves: love wave, Rayleigh wave) implies to process signals with extreme care. The seismic approach is dealt in [87].

5.2.4 Infrasound Monitoring

Due to very low atmosphere absorption and infrasonic ducts, the infrasounds have the properties to propagate over thousands of kilometers. So, an array of goniometers allows the surveillance over wide areas of the infrasound activity, like for example nuclear tests. The Comprehensive Test Ban Treaty (CTBT-1996, see [104]) has required installing a worldwide cover in order to insure the treaty to be respected.



Figure 5.12 : Triangulation of the Concorde by joined measurements in Anzère (CH)- Lysksee (S) [57]

Another application of the infrasound goniometry is the surveillance of supersonic flights. Even if this task was not a project as so, the supersonic flights were in a first approach confounded with avalanche signatures. Indeed, it was found that every day between 17h45 and 19h00, a persistent signal was located around the azimuth 300°. Investigations has shown that during its way down to Paris and London airport, the Concorde aircraft was generating a strong infrasound (Figure 5.12 and Figure 5.13).

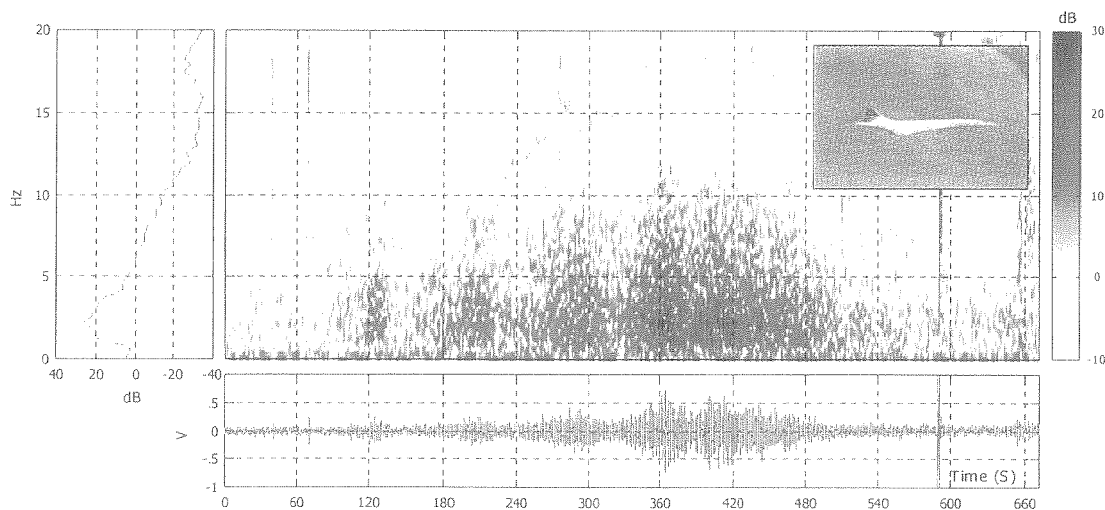


Figure 5.13 : Concorde signature (recorded by Star Echo) – strong infrasound around 2 Hz

5.3 Goniometry for outdoor active noise control

5.3.1 Problem definition and background

In order to reduce the nuisances in the vicinity of airports, the solution of outdoor active noise control was tackled (European Project BE Silence Light). Generated by a loudspeaker array, the adequate anti-noise is steered so as to “cancel” the airplane noise in a delimited volume (“Zone to protect” in Figure 5.14). The goniometry is absolutely necessary to determine the direction in which the anti-noise has to be focused. This new goniometry application does not imply to localize the airplane (which if necessary can be obtained by radar or GPS), but to determine the Direction of Arrival and more precisely the Direction of Departure (DOD) of the direct wave at the point of the anti-noise sources.

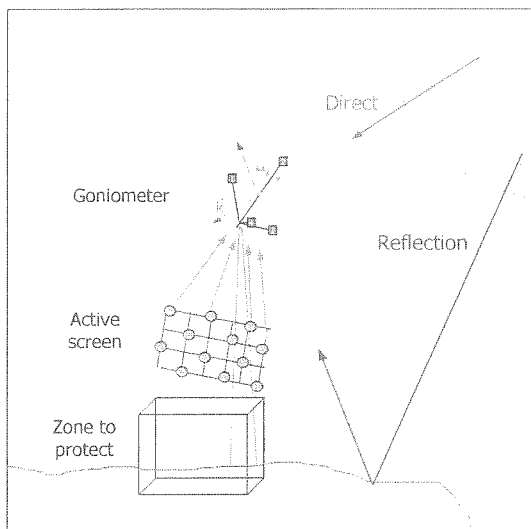


Figure 5.14 : Anti-noise experiment propagation model

This function should not be disturbed by other contributions, such as the ground reflections, anti-noise or other noise sources in the environment. The admissible degree of uncertainty on the determination of the wave vector was set to a tenth of a degree and the refreshing rate was set to 5 ms. The dimension of the anti-noise mast imposes the acceptable observation time for the goniometry, since the anti-noise has to be generated just as the sound propagates through the loudspeaker array. The entire goniometry process should not exceed 15 ms (5 m of propagation).

Following the requirements of the project coordinator, a tetrahedral geometry, coupled with the Classical Cross-correlation time delay estimator was proposed (Figure 5.15).

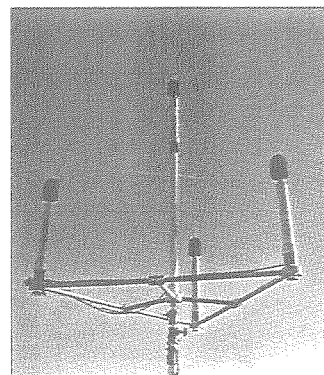
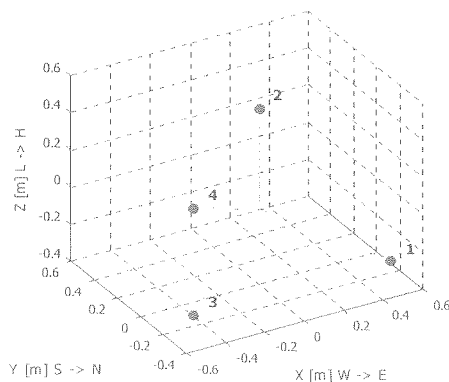


Figure 5.15 : Tetrahedral antenna made of four outdoor electrostatic measurement microphones – Inter-sensor spacing $d = 1\text{m}$

5.3.2 Foreground

Algorithm design

On the basis of the preliminary work, the algorithm was developed to fulfill the requested functions. For example, the observation time was doubled to approach the aimed precision. The detection module was designed to handle multiple sources and to reject outliers. The TDE was enhanced to the generalized method, to offer better performances in noisy condition. Finally, the cubic antenna (section 5.4) was designed to overcome the incoherent noise present in the outdoor condition.

Validation

After the validation of the new algorithms by simulation and anechoic chamber tests, the goniometry was experimented on the occasion of a helicopter flight. The helicopter location was calculated by a differential GPS, the precision of which reaches the meter. The experimental conditions were good, i.e. no wind, low ambient noise and helicopter in direct view.

The recording, whose frequency-temporal representation is presented in Figure 5.16, was collected during a one-way travel over the antenna. The spectrum reveals that frequency components can be observed up to 3 kHz, but that most of the energy is located below 500 Hz, where harmonic components clearly emerge from the wide band contribution. The tonals are attributed to the propeller blade rotation (main propeller: fundamental component at $f_1 = 17 \text{ Hz}$ + harmonics; rear propeller: $f_2 = 130 \text{ Hz}$ + harmonics). The turbine and nozzle produce the wide band noise. The comb filter effect that can be observed on sonogram ($t = 60 - 80\text{s}$) is imputed to the ground reflection (destructive summation with the direct component). Indeed, it is found that the distance, between two successive frequency zeros, equals 170 Hz when the helicopter is in vertical position ($t=80\text{s}$). This value corresponds to a difference of propagation path of 2m , which is the expected result. When the helicopter moves away, the path difference increases, as well as the inter-zeros distance.

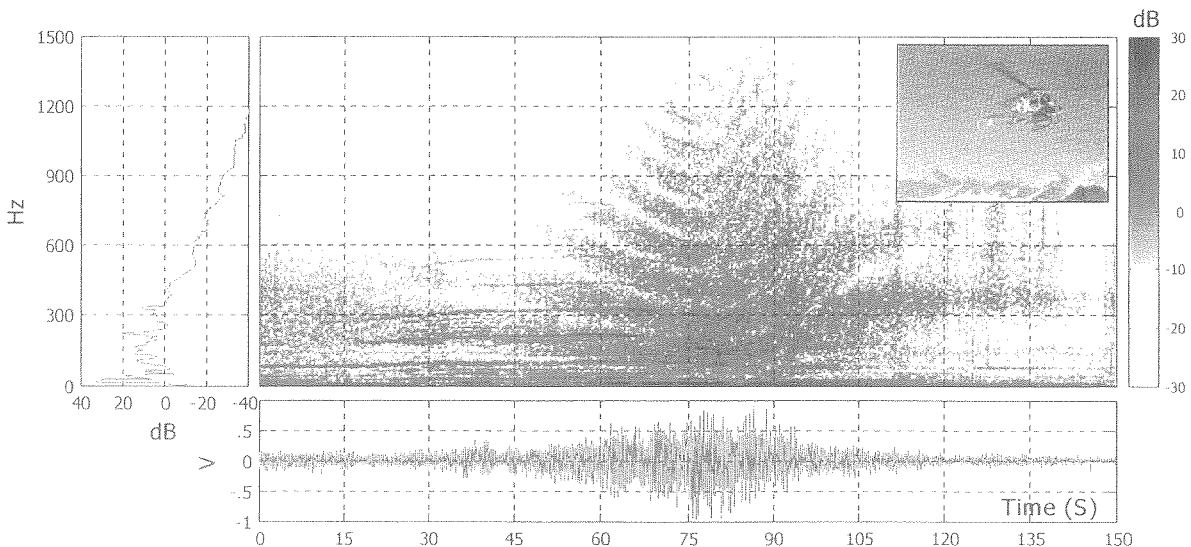


Figure 5.16 : Helicopter emission characterization

The experiment has validated the algorithms. The performance determination exhibits good detection probability, up to 90%, with errors on azimuth and elevation below 2.5° . Furthermore, the ground reflection was clearly detected (bunker roof recovered by 5 cm of snow). The goniometer tracked the helicopter up to 3 km range, corresponding to an SNR value below 0 dB.

In Figure 5.17, the acoustic measurements were superposed to the GPS information. As the graphic do not call in the time dimension, the superposition is immediate. Yet, the acoustic and GPS information that coincide on the plot do not occur at the same time, since the goniometry estimates the incident wave vector at the antenna and the GPS gives the helicopter position. Up to 10 seconds separates the two measurements.

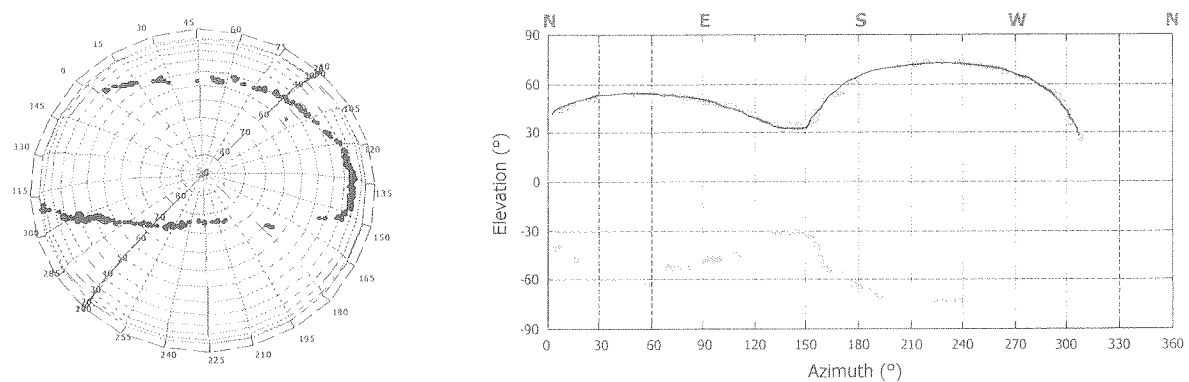


Figure 5.17 : Helicopter goniometry – Acoustic = black point markers, GPS = line

Experimentation on the site of St-Exupery

In order to integrate the goniometry in the outdoor active noise experiment, the project partner involved in the electronic design, implemented an alleviated version of the algorithms to perform the goniometry in real-time. The time constraint required optimizing the goniometry algorithms by eliminating the useless units. For example, the detection module was not considered, so that the goniometer always tracked the most powerful source. The validation of the DSP implementation occurred at the occasion of joined tests in anechoic chamber (Figure 5.18).

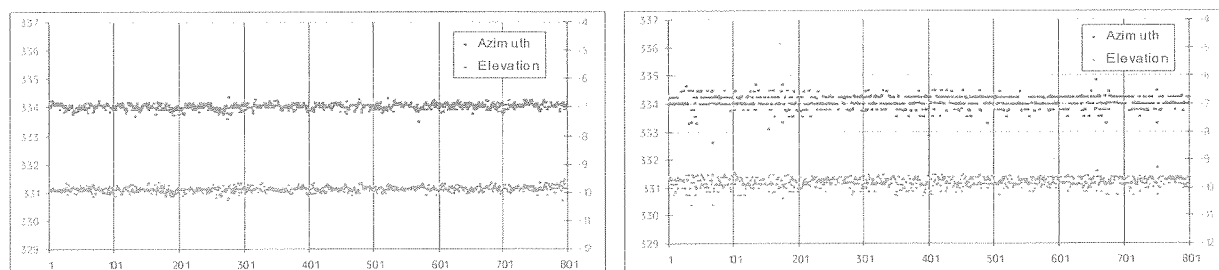


Figure 5.18 : Validation of the implementation on DSP by comparison of the localization results of an airplane noise with the Tetrahedral (Anechoic chamber) – Left, Post-processing (Matlab) – Right, Real-time process (DSP)

Although the performance disparities are acceptable, the real-time goniometry exhibits a bit less precision and resolution. The precision, traduced by the STD of the DOA, has doubled. This can be imputed to the acquisition electronic: high quality measurement alimentation, amplification and acquisition in the case of the post-processed goniometry and homemade electronic for the real-time process. The resolution decrease is simply due to the fact that the cross-correlation is not interpolated in the real-time algorithm (for CPU reasons). Nevertheless, as the STD of the DOA is beyond the resolution, there is no need to increase it for the time being. Finally, the electronic was then installed in the experimental site of St-Exupery.

The aircraft signature presented below was recorded during a preliminary acquisition campaign. From the different noise sources, the fan noise (harmonic) and jet noise (broad-band) are preponderant, respectively, when the plane is coming in direction of the antenna and when it is going away. Very strong components are present below 500 Hz but coherent energy is observable up to the 5 kHz frequency band.

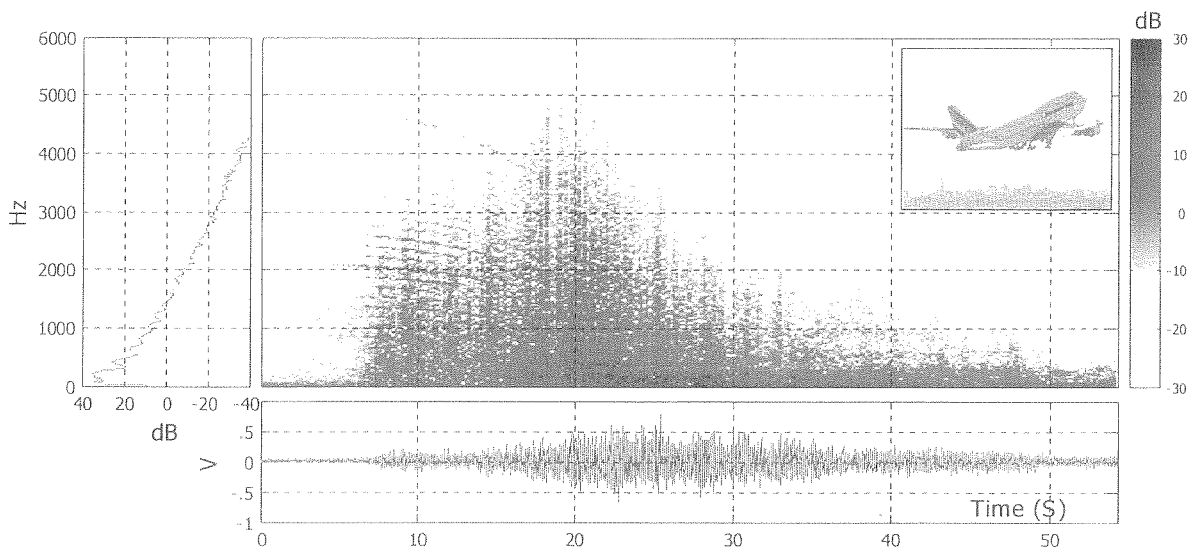


Figure 5.19 : Civil aircraft taking-off (Lyon - St-Exupery - June 1997)

In-situ experiments, performed with the DSP-implemented algorithm, exhibit satisfying performances. Yet, the system appears to be highly influenced by the wind induced noise. The Cube thus replaced the tetrahedral in order to reduce the wind effect by coherent processing. Figure 5.20 presents the localization results of a Mirage military aircraft, carried out in the St-Exupery site in windy conditions (estimated to 20 km/h). The azimuth and elevation are referenced to the antenna, but does not correspond to the classical terrestrial coordinates, since the antenna was attached to the anti-noise pylon.

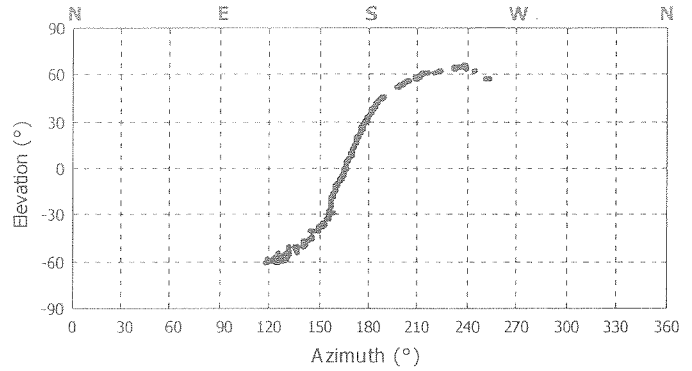
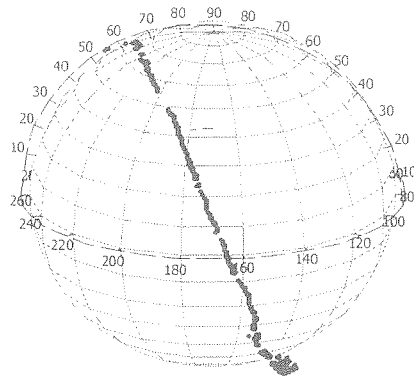


Figure 5.20 : Mirage 2000 goniometry (Lyon - St-Exupery - June 2000)

5.3.3 Signal extraction by spatial filtering

The goniometry provides the direction in which the secondary noise has to be emitted. Another need is to capture the aircraft signal, in order to build up the anti-noise. Although this step diverges from the goniometry, the combined action goniometry-extraction can be handled by a unique array of microphones performing DOA and beamforming in a mixed process. The following antenna is proposed to perform both tasks. Concerning the beamforming properties, the frequency band of best performances covers three octave bands (from 200 Hz to 1.6 kHz). The “Spider” antenna presented in next figures is made of three concentric pentagons (sub-arrays).

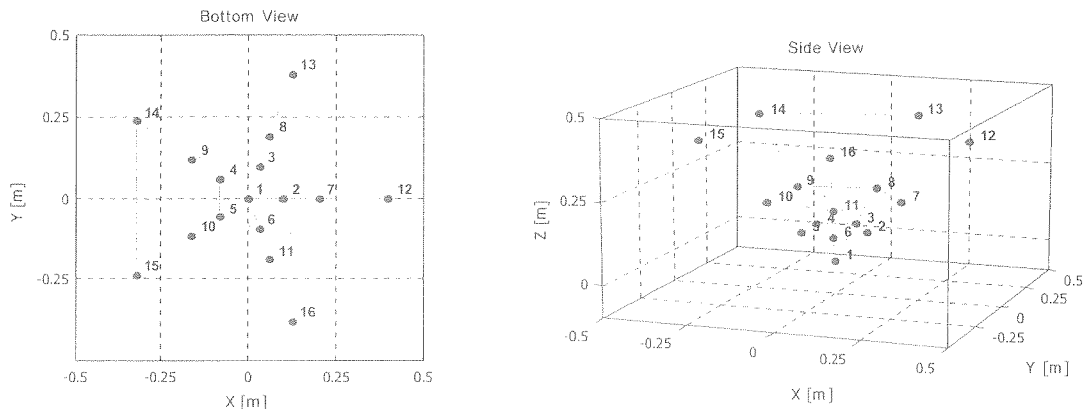


Figure 5.21 : Three octaves Spider Antenna

Their disposition was chosen in such a way that the baseline lengths double when changing of sub-array. The smallest sub-array resolves the ambiguity inconveniences, whereas the largest bring the precision. In addition, the sub-arrays are shifted to add the depth dimension to the antenna. Geometrical progression has also been respected. The next figures show the 2-D and 3-D directivity diagrams for relevant frequencies and focalization directions. The working DOA range was set to cover the solid angle defined by azimuth and elevation from -45° to 45° (correspond to 1/8 of the sphere).

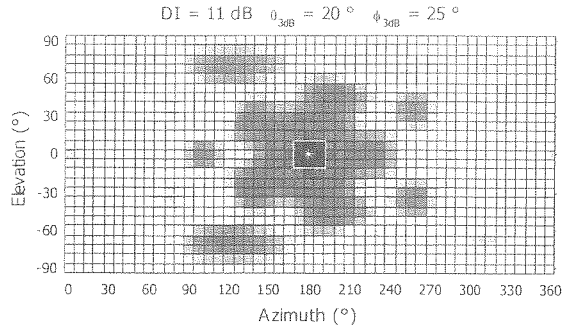


Figure 5.22 : Spider array response for the focalization direction {Azi=180°, Ele= 0°} - Narrow band signal with $f_c = 800$ Hz

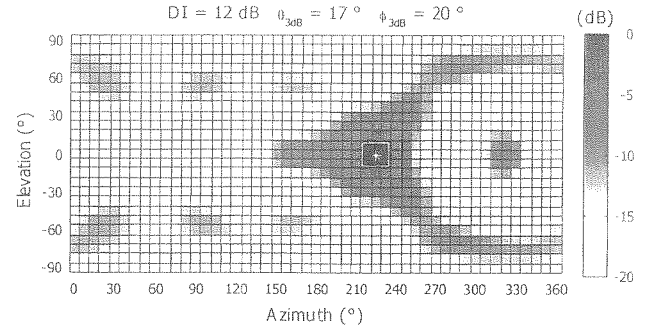


Figure 5.23 : Spider array response for the focalization direction {Azi=180°, Ele= 0°} - Narrow band signal with $f_c = 800$ Hz

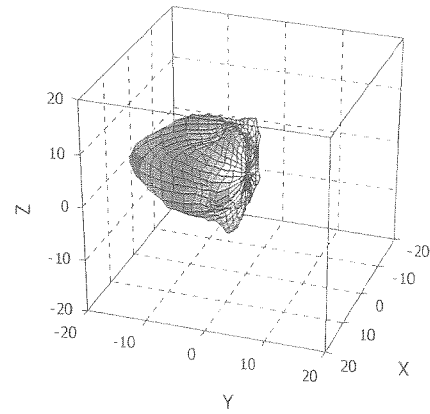
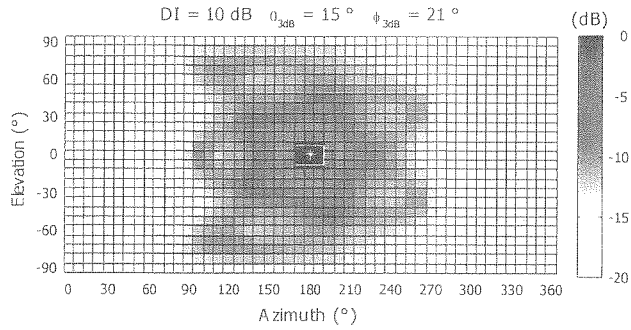


Figure 5.24 : 2D (Left) - 3D (right) Spider array response for the focalization direction {Azi=180°, Ele= 0°} - Broad band signal $\{f_{\min}= 200\text{Hz}, f_{\max}= 1600 \text{ Hz}\}$

The rear contribution (direction given Azimuth = 0°, Elevation = 0°) is at least 20dB below the energy observed in the focalization direction. This property is primordial to avoid the direct contribution to be polluted by the reflections and anti-noises.

The antenna, spreading in both xy directions, ensures a thin pencil (half-power angles ϕ_{3dB} and θ_{3dB} closed to 20°) and the antenna depth (z -axis) increases the rear-side rejection. This is traduced by directivity index beyond 10 dB.

5.4 Spatial Echogram

5.4.1 Problem definition

In the field of concert hall or auditorium acoustics, the echogram is an essential tool. Unfortunately, the classical echogram, which represents the amplitudes and arrival times of the sound rays, do not bring any information on the spatial distribution of these contributions. A new system was designed to make up for this lacuna, by localizing the direct and indirect rays. The “*spatial echogram*” will give information on the surfaces involved and on the reflection amplitudes.

5.4.2 Solution proposed

Antenna

The localization of the helicopter, performed with the Tetrahedral, demonstrated that the reflections as well as the direct contribution could be located. A first measurements campaign in the auditorium Stravinsky (Montreux – CH) showed that the Tetrahedral was not appropriated for indoor experiments, as the far-field assumption introduced large errors (due to observation point spreading – section 3.3.6). The cubic antenna (Figure 5.25) was designed to palliate this default.

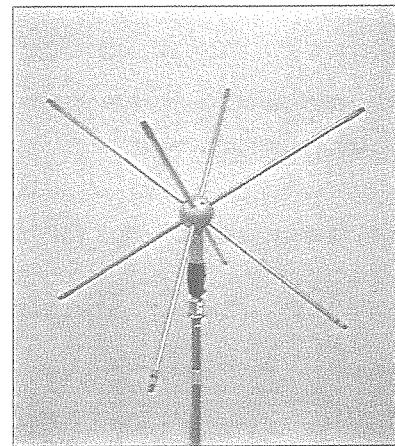
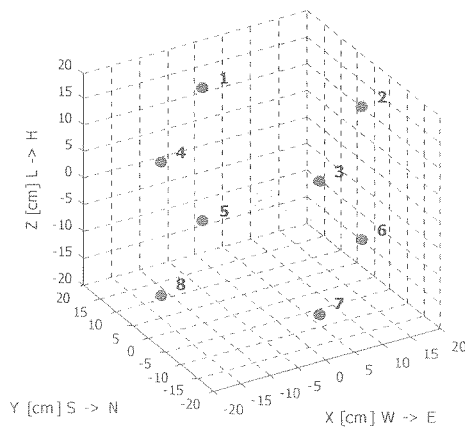


Figure 5.25 : Cubic antenna with 25cm edges made up of 8 omnidirectional electret microphones situated at the apex

The goniometry of the incident waves is carried out by estimating the time delay along the four diagonals of the cube $\{\tau_{17}, \tau_{28}, \tau_{35}, \tau_{46}\}$, so that the acoustic centers of the baselines are confounded and the errors due to far-field assumption are reduced to the distortion angle (less than 0.1°).

Active spatial echogram

In a first approach, the active goniometry was tested. Controlling the source (loudspeaker) enables to place the goniometer in its best configuration. Thus, in parallel to the goniometry, the classical

echogram is calculated for two microphones of the antenna (Figure 5.27 – upper graph). It can be obtained by cross-correlating the signal generated by the source with the recorded signals at the two sensors. A peak-picking algorithm selects the peaks of most energy for each response. The Echogram peak sets are then mixed, in order to make the relative delays, closed to those found in the localization module, appear.

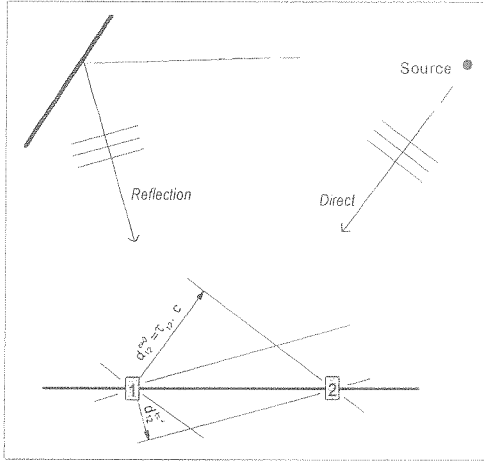


Figure 5.26 : Direct wave, reflections model

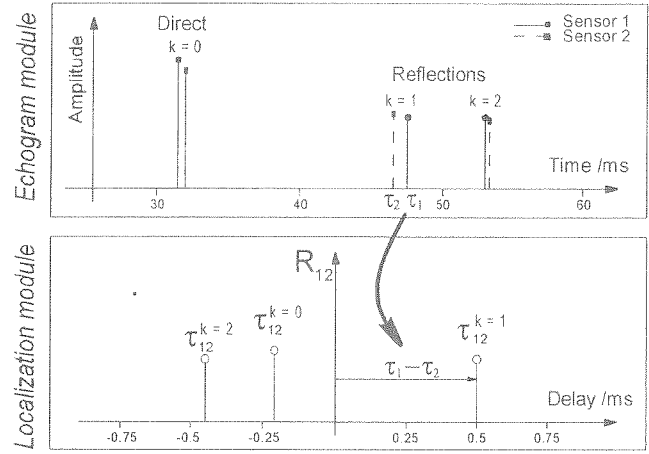


Figure 5.27 : Echogram and Localization module contributions identification

As shown in Figure 5.27 (sensors-pair 12), the algorithm associates the time differences of propagation sets, issued from the *Echogram module*, to the relative delays sets, issued from the *Localization module*. The association of Echogram sets Δ_{12} and Localization sets τ_{12} is obtained by minimizing the distance criterion expressed by

$$[I, J] = \min_{i, j} \left(\tau_{12}[i] - \Delta_{12}[j] \right)^2 \quad i, j = 1 \dots N_s$$

$$\Delta_{12} = \begin{bmatrix} \tau_2^1 - \tau_1^1, \tau_2^1 - \tau_1^2, \dots, \tau_2^1 - \tau_1^{N_s}, \\ \tau_2^2 - \tau_1^1, \tau_2^2 - \tau_1^2, \dots, \tau_2^2 - \tau_1^{N_s}, \\ \tau_2^{N_s} - \tau_1^1, \tau_2^{N_s} - \tau_1^2, \dots, \tau_2^{N_s} - \tau_1^{N_s} \end{bmatrix}^t \quad \text{Eq 5.2}$$

where $[I, J]$ is the index set of associated difference of propagation time and TDE, N_s is the *a priori* number of sources (and image sources) in presence, $\tau_{12}[i]$ is the TDE corresponding the i^{th} cross-correlation peak (sorted by amplitude) of the sensor pair 12 and $\Delta_{12}[j]$ is the j^{th} component of the vector composed of the difference of propagation time from the source to the microphone 2 (τ_2) and to the microphone 1 (τ_1).

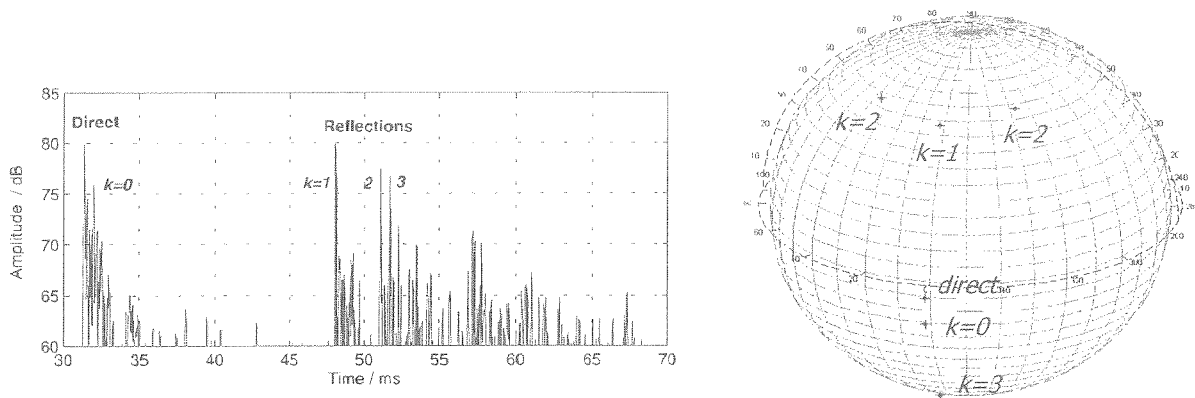


Figure 5.28 : Echogram and Localization matching results

The test presented took place in the Stravinsky Auditorium in Montreux. The goal was to localize early reflections (first 30 ms) coming from the orchestra reflectors (Figure 5.30). The trial involved a source piloted by PC (signal generator) and the cubic-shaped array. The source (5" loudspeaker) is situated backstage on a chair 50cm high and the antenna at the conductor's location, 9m away from the source and 1m up from the floor. The antenna is facing the source in such a way that the direct contribution is expected at roughly Azimuth 0°. The source - antenna pair is aligned to the central reflector below it. Two extra vertical panels, disposed between the source and the antenna, allow additional localization attempts without the masking effect of the direct component and without disturbing other reflected contributions.

The first tests session, without vertical panels, allowed validation and localization precision estimation to be made. The classical Echogram (Figure 5.28 - Left) clearly exhibits the direct contribution followed by three major reflections. The localization results are shown on the 3D-polar plot (Figure 5.28). The matching between the two approaches brings the spatial dimension to the classical temporal echogram. The total observation time was set to 5s; the acquisition length of each frame was fixed to 1024 samples and the ρ coefficient to 0.8. The matching results are summarized in Table 5.3

Contributions	Localization	Azimuth	Elevation
Direct	estimated precision of 1 or 2 degrees	1°	-4°
$k=0$	Very early reflection to a floor reflection	1°	-13°
$k=1$	Reflection to the central reflector	1°,	47°
$k=2$	Reflection to both adjacent reflectors	{ 329°, 32° }	52°
$k=3$	Reflection to a second reflection central reflector-floor	1°	-48°
$k=4$	lateral rear wall panels	34°	-4°
$k=5$	third order reflections source - central reflector - floor - central reflector - antenna	1°	82°

Table 5.3 : Contributions identified by spatio-temporal matching

The second test session, with vertical panels hiding the source, enables more reflections to be localized ($k = \{4,5\}$).

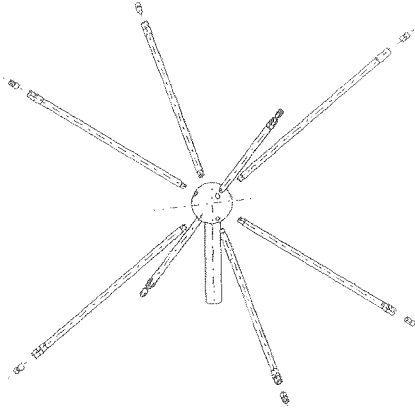


Figure 5.29 : 3D view of the Cubic antenna (homemade realization)

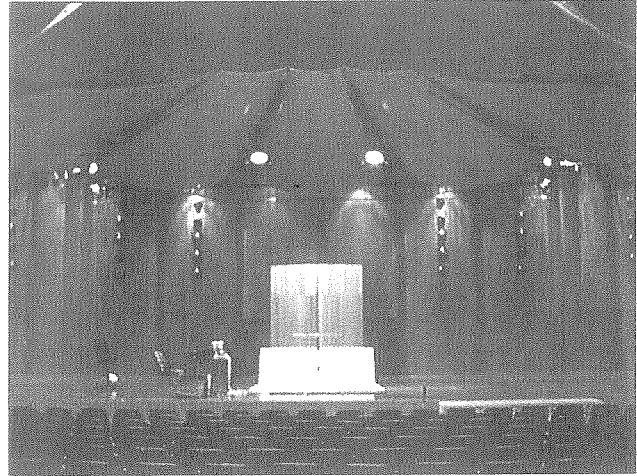


Figure 5.30 : Orchestra sound reflectors (Stravinsky Auditorium – Montreux)

During these tests, the modified CPSP has demonstrated its potential to deal with a reverberant environment. Actually, the ρ coefficient allows an optimal adaptation of the Time Delay Estimation to the acoustical characteristic of the Auditorium. The spatial echogram, concatenation of the localization module brought about by the antenna and the echogram module, corresponds to expectations. The direct contribution and five reflections were identified. In particular, the localization enables us to attribute the second reflection peaks ($k=2$) of the echogram to two separate contributions arriving simultaneously at the antenna due to the symmetric disposition of the reflectors. Extra reflections were observed by hiding the source behind panels, increasing the total observed reflections to seven contributions.

Passive spatial echogram

The next step is to do without the active loudspeaker. For example, performing the spatial echogram of an instrument (string, percussion, wind) is a goniometry challenge and is completely new. Indeed, the inherent characteristic of the instrument changes in terms of spectral properties (timbre) and in terms of spatial properties (directivity) according to the note played. The passive spatial echogram would be fundamental for studying the instruments in their concert configuration (musician and hall).

Preliminary tests were carried out with a saxophone in anechoic chamber, in order to figure out the spectrum richness and to conclude on the feasibility of the goniometry. The Figure 5.31 presents the TDE of the note Ab_2 , the fundamental frequency of which is equal to 103.4 Hz, with two microphones of the cubic antenna (inter-spacing $d = 35$ cm). The cross-spectrum amplitude (Upper - Right) reveals that most energy is below 1 kHz but that components can be found up to 6 kHz. The phase of the cross-power spectrum (Below - Right) presents good linearity up to 5 kHz, which is relevant of good

SNR. All these advantageous conditions result in a well-defined TDE narrow peak, without any ambiguities (Low - Left figure).

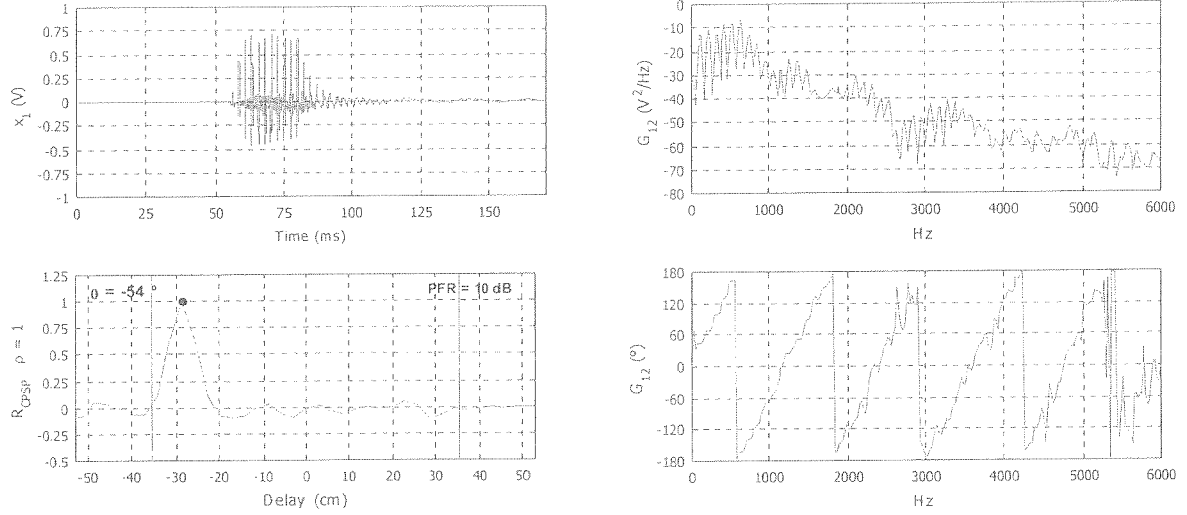


Figure 5.31 : Saxophone (Anechoic chamber test)

The corresponding DOA angle equals -54° and the cross-correlation PFR is 10 dB. These results are encouraging for future works. Yet, the difficulty must not be under evaluated. The disparities in the acoustic properties in relation to the note played, as well as to the instruments type, have to be tackled carefully. This first test was an easy case. Indeed, the fundamental is below the baseline Nyquist frequency, the harmonics spreads largely over the spectrum, the SNR is excellent and the acoustic source is unique (restricted to the bell for this tone as all holes are filled). The study of the harmonic richness in relation to the instrument types, as well as the study of multi-source instruments, would deserve works in themselves.

5.5 Underwater ultrasound localization

5.5.1 Problem definition

Within the framework of UDICOS (European Craft Project), an ultrasound goniometer was designed in order to help the divers either to locate the other divers or to find back their boat. The concept consists of an acoustic emitter placed under the boat or the diver and a reception unit (attached to the diver's wrist), acting as an acoustic compass (Figure 5.32). So, each diver has his own receptor composed of a hydrophone antenna connected to a process unit, which shows the goniometry result to the display.

The goniometry requirements are to achieve the DOA estimation in the azimuth plan with a precision of $\pm 22.5^\circ$, so as to divide the compass in 8 sectors. The good detection probability must be beyond 80% and the false alarm rate below 10%. The refreshing rate must be sufficient to avoid the diver to wait and had been set to 3 updates per second.

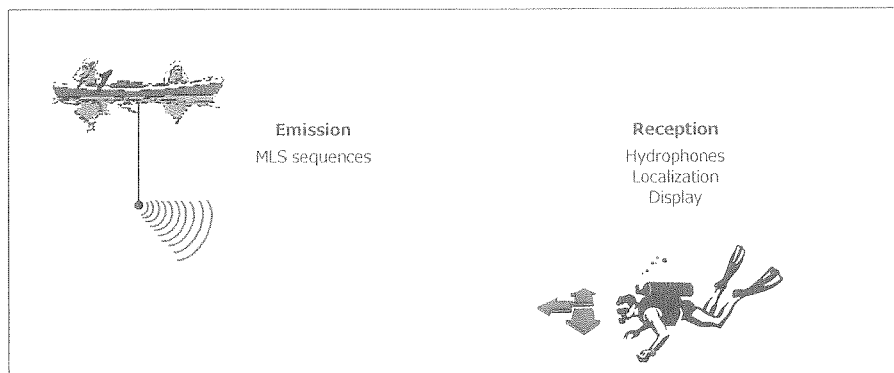


Figure 5.32 : Emission- reception model of the diver orientation system

5.5.2 Foreground

Preliminary work demonstrated that the frequency band from 20 to 50 kHz was a good compromise in term of transmission and background noise inside the divers evolution volume.

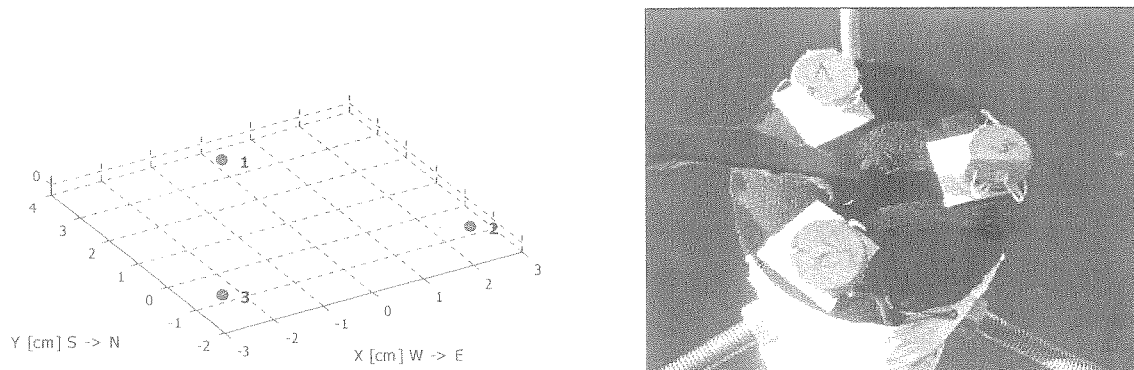


Figure 5.33 : Triangular antenna – Prototype mock-up developed by project partners

The design study concludes that the antenna extension should be comprised between 3 and 6 cm: the performance constraint requires that the inter-spacing is beyond 3 cm, and at the same time, antenna extension exceeding 6 cm would disturb the diver. The geometry was restricted to the minimum: three sensors in the azimuthal plan located at the apex of an equilateral triangle (Figure 5.33). The next table summarizes the choices and requirements for the sensors and the electronic.

DIVER DEVICE	PARAMETER	MAIN RESULT
Antenna	Geometry	3 transducers in an equilateral shaped triangular, 3-6 cm side length
	Transducers	BW : 20 kHz – 50 kHz, omnidirectional with linear phase in BW
Algorithm	TDE	Generalized method : Phase coherence algorithm
	Detection	Consistency test to eliminate the outliers
Bloc Diagram	Acquisition	Converters (8 bits, 100 kHz sampling rate)
	Processors	40 MHz DSP
	Display device	8 azimuth directions discrimination, inside mask led display, refresh rate of 3 Hz
BOAT DEVICE	PARAMETER	MAIN RESULT
Emitter	Characteristics	Omnidirectional, $L_1=100$ dB re $1\mu\text{Pa}$, BW 20 kHz -50 kHz
Signal emitted	Type	MLS salves

Table 5.4 : Goniometer design conclusions

After being validated by simulations, a first in-situ validation test took place in the Lake of Geneva. The emitter was placed 10 m below the prow of the boat and the antenna at the rear. The data were stored on diskette (recording by a digital multichannel oscilloscope), and then post-processed under Matlab. From the different campaigns that were carried out, the August 4 2000 tests made it possible to validate the goniometry for a sinusoidal salvo ($f=20$ kHz).

Chapter 6

Conclusions and perspectives

During this work, the goniometry has demonstrated on several occasions that it was an essential tool to solve the different problems encountered. Thus, the main goal of this research has been to design goniometers for a wide range of applications. Their operational contexts presented a large variety of emission properties (signal frequency, bandwidth, stationary properties), of configurations (far-field \leftrightarrow close range), source types (stationary \leftrightarrow moving, spread \leftrightarrow localized), source number (competitive sources, image sources) and environmental conditions (altitude, temperature, wind, noise).

The successive implementations were designed around a common framework, based on a two-step spatio-temporal process. The temporal step tackles the problem of the Time Delay Estimation along the antenna baselines, whereas the second step introduces the antenna geometry, in order to estimate the Direction of Arrival *per se*. The multi-sources case, as well as the outlier's rejection, is assured by a detection module, which uses the temporal and spatial properties of the propagation model. The performances of the TDE and the localization were then studied as a function of every relevant parameter, in order to determine the optimal antenna to run the two-step process. The antenna design rules concern its geometry, its size and its orientation.

The applications presented give a realistic idea of the goniometry capacities. Its performances are largely competitive to those of other techniques. Up to now, the goniometry developed during this work, fulfilled all prior requirements. Moreover, the goniometry appeared to be, in many cases, in advance with regards to technological tools such as the sound pick-up, the CPU implementation or installation constraints. For example, the positioning of the infrasound microphones for the avalanche mapping has not yet been solved: burying the sensors under the snow cover introduced uncontrolled propagation delays and infrasonic outdoor pick-up systems are polluted by wind noise. Therefore,

electro-acoustic researches have been undertaken by the LEMA to make up for this lacuna. In the application of the active outdoor noise control, the processing time constraints related to the physical reality of the experiment, forced the algorithms to be reduced to their minimal version.

However, future works can be undertaken to enhance this two-step localization method. Indeed, the resolution of the second order time delay estimator is limited to $1/B$. If the distance between the sources or the path difference is so small that the time delays induced at a sensor pair is below $1/B$, super-resolution techniques have to be considered, for example the temporal MUSIC algorithm. The price to be paid will be additional CPU load and a longer observation time. Concerning the case of highly reverberant rooms, the numerous replicas of the signals would make it worth considering MFA (Matched Field Array) processing, which takes advantage of the high correlation between the contributions (see Rabinkin [82]).

The second way to enhance the goniometry entails better knowledge of the propagation properties. The propagation phenomena affecting the goniometry such as the wave vector deviation, the diffraction effects or the reflections, would deserve specific work. This would enable us, either to develop a calibration procedure, or to determine the optimal configuration and design in order to free the goniometry from these phenomena.

It is worth noting here that the systems in competition with the goniometer are submitted to the same difficulties. Yet, the goniometry presents the advantages of using antennas with few sensors and small extensions.

The advice that could be given when handling goniometry problems would concern the spatio-temporal scales. The visualization of both spatial and temporal properties of the propagating waves and their comparison to those of the goniometer, are indeed fundamental when tackling antenna design. The signal central wavelength, the source spreading and range should always be compared to the baseline lengths and antenna extension. The period of the central frequency, the inverse bandwidth, the stationary properties of the emission have to be related to the observation time. This should help finding a good compromise between the search, on one hand for precision and resolution by designing large baselines and, on the other hand for unambiguous localization, which requires a condensed spatial sampling. The geometry influence is perhaps the most difficult to handle. It should be kept in mind that the relevant information for the localization is extracted from the projections of the incoming wave vector on each baseline. In relation with the *a priori* information on the source location, every potential DOAs should be tested in terms of spatial distribution of the projection inside the antenna. The antenna should be oriented in order to present the maximum extension to the sector to cover, as the baselines present higher performances in the Broadside directions.

The propagation phenomena should be visualized at the scale of the antenna. A perturbing phenomenon should always be handled as the superposition of a steady component, which is

homogenous with respect to the antenna and of very local components affecting each sensor differently. Whereas the local perturbations deteriorate the localization performance, the steady perturbations do not affect it but deliver *in fine* an apparent DOA, which can be very far from the source direction.

Although it is difficult to list all the potential applications, it is possible to say that every DOA application can be solved by this approach. The question is then *“Considering the operational context of my application, does the effort required to achieve the performances justify the use of this two-step goniometry more than another technique ?”* This work has demonstrated that the best results were obtained for the goniometry of a unique stationary localized source, generating broadband low pass signals in a homogenous medium, without wind and noise. To conclude, it is important to keep in mind that a judicious use of the goniometry requires the user to balance the operational conditions with the performances to achieve.

Chapter 7

Annex

7.1 CRLB

The Cramer-Rao Lower Bound defines the best performance that can be achieved. Concerning the TDE, the CRLB is the lower bound of the TDE error variance.

Under the assumptions that the noise are Gaussian, stationary and mutually uncorrelated, that both signal and noise present a flat spectrum inside the bandwidth and that the observation time is sufficient to respect $BT > 100$, the CRLB is given by the following formula [74].

Baseband signal

SNR << 1	SNR >> 1
$\sigma_{CRLB}^2 = \frac{3}{8\pi^2} \cdot \frac{1}{SNR_{sys}^2} \cdot \frac{1}{B^3T}$	$\sigma_{CRLB}^2 = \frac{3}{4\pi^2} \cdot \frac{1}{SNR_{sys}} \cdot \frac{1}{B^3T}$

where B is the bandwidth, T is the observation time. The SNR_{sys} is defined as a function of the SNR at each sensor

$$SNR_{sys} = \frac{SNR_1 \cdot SNR_2}{1 + SNR_1 + SNR_2}$$

If the acoustic conditions are homogenous inside the antenna $SNR_1 = SNR_2$ and the relation becomes

$$SNR_{sys} = \frac{(SNR)^2}{1 + 2 SNR}$$

Bandpass signal

$\text{SNR} \ll 1$	$\sigma_{CRLB}^2 = \frac{3}{8\pi^2} \cdot \frac{1}{\text{SNR}_{\text{sys}}^2} \cdot \frac{1}{T} \cdot \frac{1}{f_{\text{max}}^3 - f_{\text{min}}^3} \quad \text{with} \quad f_{\text{max}}^3 - f_{\text{min}}^3 = 3Bf_c^2 \cdot \left(1 + \frac{B^2}{12f_0^2}\right)$ $\sigma_{CRLB}^2 = \frac{1}{8\pi^2} \cdot \frac{1}{\text{SNR}_{\text{sys}}^2} \cdot \frac{1}{BT} \cdot \frac{1}{f_c^2} \cdot \frac{1}{\left(1 + \frac{B^2}{12f_c^2}\right)}$
$\text{SNR} \gg 1$	$\sigma_{CRLB}^2 = \frac{3}{4\pi^2} \cdot \frac{1}{\text{SNR}_{\text{sys}}^2} \cdot \frac{1}{T} \cdot \frac{1}{f_{\text{max}}^3 - f_{\text{min}}^3}$ $\sigma_{CRLB}^2 = \frac{1}{4\pi^2} \cdot \frac{1}{\text{SNR}_{\text{sys}}^2} \cdot \frac{1}{BT} \cdot \frac{1}{f_c^2} \cdot \frac{1}{\left(1 + \frac{B^2}{12f_c^2}\right)}$

where f_{min} and f_{max} are the cut-off frequencies and f_c is the central frequency of the spectrum of bandwidth B .

In many case, the modelization of the signal by a flat top band-pass signal is too restrictive. In [74], Quazi has calculated the CRLB for signal and noise, the spectra of which present a fall-off behavior.

7.2 CPE (Ianniello)

The correlator performance estimator provides performance prediction for the cross-correlation, in presence of large estimation errors or ambiguous, or anomalous estimates. The hypotheses are the same as those for the CRLB calculation. The calculation are done under the assumptions that the noise are Gaussian, stationary and mutually uncorrelated, that both signal and noise present a flat spectrum inside the bandwidth and that the observation time is sufficient to respect $BT > 100$. Finally, the ambiguous estimates have to be uniformly distributed across the correlation window $[-T_0, T_0]$.

The CPE yields to the following estimate of the variance on the TDE error

$$\sigma_{CPE}^2 = \frac{PT_0^2}{3} + (1-P)\sigma_{CRLB}^2$$

$$P \cong 1 - \int_{-\infty}^{\infty} \frac{1}{\sqrt{2\pi}} e^{-\frac{1}{2}(x-\alpha)^2} \cdot \left\{ \int_{-\infty}^{\beta x} \frac{1}{\sqrt{2\pi}} e^{-\frac{1}{2}y^2} dy \right\}^{M-1} dx$$

$$\alpha = \frac{\sqrt{2BT} \cdot \xi}{\sqrt{\xi^2 + (1+\xi)^2}} \quad \beta = \sqrt{1 + \frac{\xi^2}{(1+\xi)^2}}$$

$$M = 2 \frac{T_0}{T_c} \quad ; \quad B_s = 2B \quad ; \quad T_c = \frac{1}{2B}$$

P is the probability of wrong detection (ambiguities or anomalies), α is the post-integration SNR, β is a scaling factor (1 - 1.41), M is the number of independent values of the cross-correlation, T_c is the correlation time of the signal, and B_s the statistical bandwidth.

7.3 Norm criterion in spatial domain

The norm criterion expressed the distance between the measurements and the optimal case. Considering that the measured delay set was identified without any ambiguity, the measured wave vector is given in section 2.5.2 by

$$\vec{n}_{meas} = c \cdot \mathcal{D} \cdot \vec{\tau}_{meas} \quad \text{Eq 7.1}$$

The index $()_{meas}$ refers to measured values (noise contaminated). The norm criterion is thus expressed by

$$J_{\vec{n}} = \left| \|\vec{n}_{meas}\| - 1 \right| \quad \text{Eq 7.2}$$

The closest optimal wave vector, that satisfies the norm criterion, is obtained by normalizing the measured wave vector by its norm. The correspondent closest optimal set of delays is given by

$$\vec{\tau}_{opt} = c^{-1} \cdot \mathcal{D} \cdot \vec{n}_{opt} \quad \text{with} \quad \vec{n}_{opt} = \frac{\vec{n}_{meas}}{\|\vec{n}_{meas}\|} \quad \text{Eq 7.3}$$

where the index $()_{opt}$ refers to the closest optimal values, according to the norm criterion. The time domain counterpart of Eq 2.39 is given by

$$J_{\vec{n}} = \left| \|\vec{n}_{meas}\| - 1 \right| \quad \leftrightarrow \quad \left| \|\vec{\tau}_{meas}\| - \|\vec{\tau}_{opt}\| \right| \quad \text{Eq 7.4}$$

Finally, the multiplication of the time domain, equivalent by the speed of sound, translates the norm criterion into a spatial distance that can be compared to the antenna extension.

7.4 Speed of sound influence on 3D - DOA

The following calculation demonstrates that errors on the estimation of the speed of sound do not have any influence on the estimation of the DOA azimuth Az . The azimuth is related to the wave vector through

$$Az = \frac{\pi}{2} - \tan^{-1}\left(\frac{n_y}{n_x}\right) \quad \text{Eq 7.5}$$

Therefore, considering small errors $\delta\alpha$ around the nominal value α , we can build the relation between the azimuth errors and the wave vector errors by derivating the azimuth

$$\frac{\delta Az}{\delta\left(\frac{n_y}{n_x}\right)} = -\frac{1}{1+\left(\frac{-n_y}{n_x}\right)^2} \cdot (-1) = \frac{1}{1+\left(\frac{n_y}{n_x}\right)^2}$$

The estimation error on the azimuth is given by

$$\begin{aligned} \delta Az &= \frac{n_x^2}{n_x^2 + n_y^2} \delta\left(\frac{n_y}{n_x}\right) \quad \text{with} \quad \frac{\delta\left(\frac{n_y}{n_x}\right)}{\left(\frac{n_y}{n_x}\right)} = \frac{\delta n_y}{n_y} - \frac{\delta n_x}{n_x} \\ \delta Az &= \frac{n_x n_y}{n_x^2 + n_y^2} \left(\frac{\delta n_y}{n_y} - \frac{\delta n_x}{n_x} \right) = \frac{n_x \delta n_y - n_y \delta n_x}{n_x^2 + n_y^2} \end{aligned} \quad \text{Eq 7.6}$$

The wave vector component are related to the speed of sound through the relation

$$\vec{n} = c \cdot \mathcal{D} \cdot \vec{\tau}, \quad \mathcal{D} = D^{-1}$$

which can be written in the parametric form

$$n_k = c \cdot \sum_{n=1}^N \mathcal{D}_{kn} \cdot \tau_n$$

As the inverse sensor matrix position and the TDE estimation are unrelated to the speed of sound, the wave vector errors is simply equal to

$$\delta n_k = \delta c \cdot \sum_{n=1}^N \mathcal{D}_{kn} \cdot \tau_n = \delta c \cdot S_k$$

Introducing this relation in equation Eq 7.6 results in

$$\delta Az = \frac{c \cdot S_x \cdot \delta c \cdot S_y - c \cdot S_y \cdot \delta c \cdot S_x}{c^2 \cdot (S_x^2 + S_y^2)} = \frac{S_x S_y \left(\frac{\delta c}{c} - \frac{\delta c}{c} \right)}{(S_x^2 + S_y^2)} = 0$$

which means that for any value of c and δc , the induced error on the azimuth is null.

7.5 Array performance indexes [4]

Half-power angle

The performance of a beamforming array can be quantified by the pick-up angle at - 3 dB (θ_{3dB}), which represents the width of the main lobe of the directivity pattern, 3 dB below the maximum level of the lobe. Figure 7.2 represents a polar view of the directivity pattern, for a Broadside array composed of 5 microphones equally spaced ($d=10$ cm), in the [1 kHz-2 kHz] frequency band, where the beamforming direction is marked out by the angles $\theta_0 = 73^\circ$.

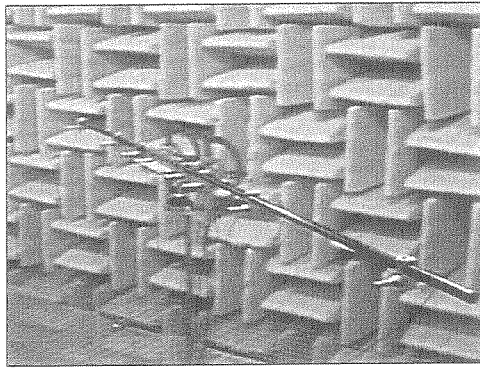


Figure 7.1 : Four octave bands beamformer
13 microphones nested array [106]

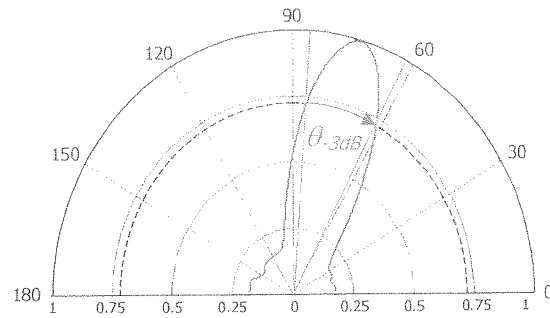


Figure 7.2 : Polar view of the directivity pattern in the horizontal plane of a Broadside array with 5 microphones

Directivity Index

The directivity index enables the energy received from a given direction to be compared to the overall energy. This characteristic, applied to a microphone array, enables to quantify the capacity of an array to pick up the energy, in a favored direction, while rejecting the energy stemming from the other directions. The directivity factor Di is equal to the ratio of its radiation intensity, in the beamforming direction over that of an isotropic source. The numerical approximation is obtained performing a double summation over small surface elements ($\pi/N \cdot 2\pi/M$).

$$Di = \frac{4\pi F(\theta_0, \phi_0)}{\frac{\pi}{N} \frac{2\pi}{M} \cdot \sum_{j=1}^M \left[\sum_{i=1}^N F(\theta_i, \phi_j) \sin(\theta_i) \right]} \quad DI = 10 \log_{10} Di \quad \text{Eq 7.7}$$

where the focalization direction is defined by the polar angles (θ_0, ϕ_0) , F is the directivity function, N and M are the number of uniform divisions in respectively azimuth and elevation.

The directivity index DI corresponds to the directivity factor expressed in dB.

Abbreviations and symbols

A	Signal amplitude	1
B	Signal bandwidth	Hz
c	Speed of sound	m/s
d	Inter-element spacing	m
D	Sensor relative location matrix	m
D_i	Directivity factor	1
DI	Directivity index (dB)	1
\mathcal{D}	Inverse sensor relative location matrix	m ⁻¹
f	Temporal frequency	Hz
f_c	Central frequency of a band-pass signal	Hz
f_{\min}	Low cut-off frequency	Hz
f_{\max}	Low cut-off frequency	Hz
F_s	frequency sampling	Hz
$G_{11}(f)$	Power Spectrum Density (PSD) of the signal $x_1(t)$	V ² /Hz
$G_{12}(f)$	Cross-Power Spectrum Density of the signal $x_1(t)$ and $x_2(t)$ (CSD)	V ² /Hz
k	Sample index in discrete Time domain	1
K	Samples number per observation window	1
κ	Wave vector	rad/m
m	Sensor index	1
n_b	Baseline index	1
n_f	Frame index	1
M	Antenna sensor number	1
N_b	Number of baselines	1
N_s	Number of sources in presence	1
N_f	Number of frames	1
v	Normalized wave vector	1
p	Acoustic pressure	Pa
r	Range from the source to the sound pick up system	m
$R_{12}(\tau)$	Cross-correlation function of signal 1 and 2 calculated at the delay τ	V ²
$s(t)$	Source signal (time domain)	V
St	Strouhal number	1

T	Observation time	s
ξ_m	Sensors spatial position vector (origin= antenna phase center)	m
ξ_s	Source spatial position vector (origin= antenna phase center)	m
$x_1(t)$	Signal recorded by microphone 1 (time domain)	V
$X_1(f)$	Fourier transform (Frequency domain) of $x_1(t)$	V/Hz
(θ, ϕ)	3D polar angle	rad
θ_{-3dB}	Half-power angle	rad
λ	Wavelength	m
λ_c	Central wavelength of a band-pass signal	m
$\gamma_{12}(f)$	Complex coherence function	1
κ	Condition number	1
Φ	Windscreen diameter	m
ρ	Coefficient	1
ω	Pulsation	rad/s
δ_{12}	Time Difference of Arrival between sensors 1 and 2	s
τ_{s1}	Propagation time from the source to the sensor 1	s
τ_{12}	Time difference of arrival from sensor 1 to sensor 2	s
$()^*$	Complex conjugate	
$()^t$	Transpose	
$()^H$	Hermitian = complex conjugate of the transpose	
(\wedge)	Estimation	
$ \quad $	Absolute value	
\otimes	Convolution operator	
$E[.]$	Expectation	
σ^2	Variance of a random variable	
$()_0$	Nominal value	
$()_{app}$	Apparent value	

ABBREVIATION

CPE	<i>Correlator Performance Estimate</i>
CRLB	<i>Cramér-Rao Lower Bound</i>
CPSP	<i>Cross Power Spectrum Phase</i>
CSD	<i>Cross Power Spectrum Density</i>
DOA	<i>Direction of Arrival</i>
FIR	<i>Finite Impulse Response</i>
LMS	<i>Least Mean Square</i>
MSC	<i>Magnitude Squared Coherence</i>
PSD	<i>Power Spectrum Density</i>
SNR	<i>Signal to Noise ratio</i>
STD	<i>Standard Deviation</i>
TDE	<i>Time Delay Estimation</i>
TDOA	<i>Time Difference Of Arrival</i>
ULA	<i>Uniform Linear Array</i>

Bibliography

- [1] V. Adam, V. Chritin, M. Rossi and E. Van Lancker, "*Infrasonic monitoring of snow-avalanche activity. What do we know and where do we go from here ?*," International Symposium on Snow and Avalanches, Chamonix, Annals of Glaciology, vol. 26, pp. 324-328, May 1997.
- [2] J.E. Adcock, J.H. DiBiase, M.S. Brandstein, and H.F. Silverman, "*Practical issues in the use of a frequency-domain delay estimator for microphone-array applications*," Proc. of the 128th Acoustical Society of America Meeting, Austin, Texas, Nov. 1994.
- [3] Y. Al, X. Qiu, and C. H. Hansen, "*Minimizing wind effects on active control systems for attenuating outdoor transformer noise*," J. of the Noise Control Engineering, vol. 48, no. 4, Jul-Aug 2000.
- [4] C.A. Balanis, "*Antenna Theory, Analysis and Design*," Harper & Row, 1982.
- [5] A.J. Bedard, G.E. Greene, J. Intrieri and R. Rodriguez, "*On the Feasibility and Value of Detecting and Characterizing Avalanches Remotely by Monitoring Radiated Sub-audible Atmospheric at Long Distances*," Proc. of the Engineering Foundation Conference, A Multidisciplinary Approach to Snow Engineering, vol. 08, n° 2, p 1-10, Dec 1989.
- [6] R.E. Boucher and J.C. Hassab, "*Analysis of Discrete Implementation of Generalized Cross-Correlator*," IEEE Transactions on Speech and Audio Processing, vol. 29, no. 3, pp. 609-611, June 1981.
- [7] M.S. Brandstein, "*A Framework for Speech Source Localization Using Sensor Arrays*," PhD thesis, Brown University, Providence RI, May 1995.
- [8] M.S. Brandstein, John E. Adcock, and Harvey F. Silverman, "*A practical time-delay estimator for localizing speech sources with a microphone array*," Computer Speech and Language, vol. 9, pp. 153-169, April 1995.
- [9] M.S. Brandstein and H. Silverman, "*A practical methodology for speech source localization with microphone arrays*," Computer, Speech, and Language, vol. 11, no. 2, pp. 91-126, April 1997.
- [10] M.S. Brandstein, J. E. Adcock, and H. F. Silverman, "*A closed-form location estimator for use with room environment microphone arrays*," IEEE Transactions on Speech and Audio Processing, vol. 5, no. 1, pp. 45-50, Jan. 1997.
- [11] M.S. Brandstein, "*An event-based method for microphone array speech enhancement*," Proc. of ICASSP, Phoenix, Arizona USA, vol. 2, pp. 953-956, March. 1999.
- [12] M.S. Brandstein, J.E. Adcock, and H. Silverman, "*Microphone array localization error estimation with application to sensor placement*," J. Acoust. Soc. Am., vol. 99, no. 6, pp. 3807-3816, June 1996.
- [13] M.S. Brandstein and H. Silverman, "*A Robust Method for Speech Signal Time-Delay Estimation in Reverberant Rooms*," Proc. of ICASSP, Munich, Germany, vol. 1, pp. 375-378, April 1997.

- [14] M.S. Brandstein, J. E. Adcock and H. F. Silverman, "A Localization-Error Based Method for Microphone-Array Design," Proc. of ICASSP, Atlanta, GA, vol. 2, pp. 901-904, May 1996.
- [15] M.S. Brandstein, "Time-delay estimation of reverberated speech exploiting harmonic structure," J. Acoust. Soc. Am., vol. 105, no. 5, pp. 2914-2919, May 1999.
- [16] G.C. Carter, "Special Issue on Time Delay Estimation," IEEE Trans. on Acoustics, Speech and Signal Processing, vol. 29, no. 2, June 1981.
- [17] G.C. Carter, "Coherence and Time Delay Estimation: An Applied Tutorial for Research, Development, Test, and Evaluation Engineers," IEEE Press, Trade Cloth, April 1993.
- [18] S.K. Chow and P.M. Schultheiss, "Delay Estimation Using Narrow-band Processes," IEEE Trans. on Acoustics, Speech and Signal Processing, vol. 29, no. 3, pt. 2, pp. 478-484, June 1981.
- [19] T. Chou, "Frequency-independent beamformer with low response error," Proc. of ICASSP, pp. 2995-2998, 1995.
- [20] Y.T. Chan and K.C. Ho, "A Simple and Efficient Estimator for Hyperbolic Location," IEEE Trans. on Signal Processing, vol. 42, no. 8, pp. 1905-1915, Feb. 1994.
- [21] B. Champagne, S. Bedard, and A. Stephenne, "Performance of time-delay estimation in the presence of room reverberation," IEEE Trans. on Speech and Audio Processing, vol. 4, no. 2, pp. 148-152, March 1996.
- [22] V. Chritin, M. Rossi, R. Bolognesi, "Acoustic detection system for operational avalanche forecasting," Proc. of International Snow and Science workshop, Banff, Canada, pp. 149-151, Oct. 1996.
- [23] F. de Coulon, "Théorie et Traitement des Signaux," Presses Polytechniques et Universitaires Romandes ed., Lausanne, Ecole Polytechnique Fédérale de Lausanne, vol. 6, 1998.
- [24] C. Couvreur and P. Chapelle, "Statistical Decision Theory Methods for Noise and Vibration Engineering", <http://citeseer.nj.nec.com/2837.html>.
- [25] R. Cook, "Microphone windscreens for low level environmental measurements," Proc. of the INTER-NOISE 91, pp. 969-972, 1991.
- [26] S.R. Dooley and A.K. Nandi, "Adaptive subsample time delay estimation using Lagrange interpolators," IEEE Signal Processing Letters, vol. 6, no. 3, pp. 65-67, March 1999.
- [27] S.R. Dooley and A.K. Nandi, "Comparison of discrete subsample time delay estimation methods applied to narrowband signals," IOP Measurement Science & Technology, vol. 9, no. 9, pp. 1400-1408, Sept. 1998
- [28] G.L. Duckworth, D.C. Gilbert, and J.E. Barger, "Acoustic counter-sniper system," SPIE, vol. 2938, no. 38, pp. 262-275, 1997.
- [29] G.W. Elko, "Microphone array systems for hands-free telecommunication," Speech Communication, vol. 20, no. 3-4, pp. 229-240, Dec. 1996.
- [30] F. Fahy, "Foundations of Engineering Acoustics," Academic Press, 2001.
- [31] B.G. Ferguson, "Improved Time-Delay Estimates of Underwater Acoustic Signals Using Beamforming and Prefiltering Techniques," IEEE J. Oceanic Eng., vol. 14, no. 3, pp. 238-244, July 1989.
- [32] S. Fischer and K.U. Simmer, "An adaptive microphone array for hands-free communication," Proc. of 4th International Workshop on Acoustic Echo and Noise Control, Rros, Norway, pp. 44-47, 1995.
- [33] S. Fischer and K.U. Simmer, "Beamforming microphone arrays for speech acquisition in noisy environments," Speech Communication, vol. 20, no. 3-4, pp. 215-227, Dec. 1996.
- [34] J.L. Flanagan, D.A. Berkley, G.W. Elko, J.E. West, and M.M. Sondhi, "Autodirective microphone systems," Acustica, vol. 73, pp. 58-71, 1991.
- [35] J.L. Flanagan, J.D. Johnston, R. Zahn, and G.W. Elko, "Computer-steered microphone arrays for sound transduction in large rooms," J. Acoust. Soc. Am., vol. 78, no. 5, pp. 1508-1518, Nov. 1985.
- [36] T. Funkhouser, I. Carlbom, G. Elko, G. Pingali, M. Sondhi, and J. West, "A beam tracing approach to acoustic modeling for interactive virtual environments," Proc. of the 25th annual conference on Computer Graphics, Orlando, Floride USA, pp. 21-32, July 1998.

- [37] P.G. Georgiou, C. Kyriakakis, and P. Tsakalides, "Robust time delay estimation for sound source localization in noisy environments," Workshop on the Applications of Signal Processing to Audio and Acoustic, Mohonk, New York USA, pp. 18-21, Oct. 1997.
- [38] D. Giuliani, M. Omologo, and P. Svaizer, "Talker Localization and Speech Recognition Using a Microphone Array and a Cross-Powerspectrum Phase Analysis," Proc. of ICSLP, vol. 22, no. 1, pp. 1243-1246, Sep. 1994.
- [39] D. Giuliani, M. Matassoni, M. Omologo, and P. Svaizer, "Use of Different Microphone Array Configurations for Hands-free Speech Recognition in Noisy and Reverberant Environment," Proc. of Eurospeech, Rhodes, Greece, vol. 1, pp. 347-350. Sept. 1997.
- [40] D. Giuliani, M. Matassoni, M. Omologo, and P. Svaizer, "Hands Free Continuous Speech Recognition in Noisy Environment using a Four Microphone Array," Proc. of ICASSP, Detroit, vol. 2, pp. 860-863, April 1995.
- [41] M. Goodwin and G. Elko, "Constant beamwidth beamforming," Proc. of ICASSP, vol 1, pp. 169-172, 1993
- [42] J.C. Hassab and R.E. Boucher, "Optimum estimation of time delay by a generalized correlator," IEEE Trans. on Acoustics, Speech and Signal Processing, vol. 27, no. 4, pp. 373-380, Aug 1979.
- [43] J.C. Hassab and R.E. Boucher, "Performances of the generalized Cross Correlator in the presence of a strong spectral peak in the signal," IEEE Trans. on Acoustics, Speech and Signal Processing, vol. 29, no. 3, pp. 549-555, June 1981.
- [44] S. Holm, B. Elgetun, and G. Dahl, "Properties of the beampattern of weight- and layout-optimized sparse arrays," IEEE Transactions on Ultrasonics, Ferroelectrics, and Frequency Control, vol. 44, pp. 983-991, Sep. 1997.
- [45] Y. Huang, J. Benesty, and G. W. Elko, "Adaptive eigenvalue decomposition algorithm for realtime acoustic source localization system," Proc. of ICASSP, Phoenix, Arizona USA, vol. 2, pp. 937-940, March 1999.
- [46] J.P. Ianniello, "Threshold effects in time delay estimation using narrowband signals," Proc. of ICASSP, vol. 1, pp. 375-378, 1982.
- [47] J.P. Ianniello, "Time delay estimation via cross-correlation in the presence of large estimation errors," Trans. Acoust., Speech, Signal Processing, vol. 30, n°6, pp. 998-1003, Dec 1982.
- [48] J.P. Ianniello, "Comparison of the Ziv-Zakai Lower Bound on the time delay estimation with correlator performance," Proc. of ICASSP, vol. 2, pp. 875-878, April 1983.
- [49] E.E. Jan, P. Svaizer, and J.L. Flanagan, "A database for microphone array experimentation," Proc. of Eurospeech, pp. 813-816. ESCA, 1995.
- [50] E.E. Jan and J.L. Flanagan, "Sound Source Localization in Reverberant Environments using an Outlier Elimination Algorithm," Proc. of ICSLP, Philadelphia, USA, vol. 3, pp. 1321-1325, Oct. 1996.
- [51] D.H. Johnson and D.E. Dudgeon, "Array Signal Processing: Concepts and Techniques," Prentice Hall Signal Processing Series. Prentice-Hall, Englewood Cliffs, NJ, 1993.
- [52] M. Joho and G.S. Moschytz, "On the Design of the Target-Signal Filter in Adaptive Beamforming," IEEE Trans Circuits Systems II, vol. 46, no. 7, pp. 963-966, July 1999.
- [53] W. Kellermann, "A self-steering digital microphone array," Proc. of ICASSP, Toronto, Canada, vol. 5, pp. 3581-3584, May 1991.
- [54] C.H. Knapp and G.C. Carter, "The Generalized Correlation Method for Estimation of Time Delay," IEEE Trans. on Acoustics, Speech and Signal Processing, vol. 24, no. 4, pp. 320-327, Aug. 1976.
- [55] H. Krim and M. Viberg, "Two decades of array signal processing research," IEEE Signal Processing Magazine, vol. 13, no. 4, pp. 67-94, July 1996.
- [56] J. Krolik, M. Joy, S. Pasupathy, and M. Eizenman, "A comparative study of the LMS adaptive filter versus generalized correlation methods for time delay estimation," Proc. of ICASSP, vol. 1, pp. 15.11/1-4, March 1994.
- [57] L. Liszka, "Infrasonic Observations of the Gaz Explosion on April 26-27, 1995", Journal of Low Noise and Vibration, vol. 15, no. 1, 1996.
- [58] V. Madisetti and D.B. Williams, "The Digital Signal Processing Handbook," IEEE Press, 1998.

- [59] Y. Mahieux, G. Le Tourneur, A. Gilloire, A. Saliou, and J.P. Jullien, "A microphone array for multimedia workstations," Proc. of the 3rd International Workshop on Acoustic Echo Control, Plestin les Greves, France, pp. 145-149, Sep. 1993.
- [60] M. Matassoni, M. Omologo, L. Cristoforetti, D. Giuliani, P. Svaizer, E. Trentin, and E. Zovato, "Some results on the development of an hands-free Speech recognizer for car-environment," Proc. of the Workshop on Automatic Speech Recognition and Understanding, Keystone, Colorado USA, pp. 377-380, Dec. 1999.
- [61] J. Max and J-L. Lacoume, "Méthodes et techniques de traitement du signal et applications aux mesures physiques – Principes généraux et methodes classiques," Masson, Paris, 1996.
- [62] J. Max and al., "Méthodes et techniques de traitement du signal et applications aux mesures physiques – Appareillage – Méthodes nouvelles – Exemple d'applications," Masson, 1987.
- [63] S. Morgan and R. Raspet, "Investigation of the mechanisms of low-frequency wind noise generation outdoors," J. Acous. Soc. Am., vol. 92, no. 2 Pt. 1, pp. 1180-1183, Aug. 1992.
- [64] J.P. Nougier, "Méthodes de calcul numérique," Masson, 1987.
- [65] R.O. Nielsen, "Sonar Signal Processing," Artech House, 1991.
- [66] C.L. Nikias and R. Pan, "Time Delay Estimation in Unknown Gaussian Spatially Correlated Noise," Proc. of ICASSP, vol. 5, pp. 2638-2641, April 1988.
- [67] M. Omologo and P. Svaizer, "Use of the cross-power spectrum phase in acoustic event localization," Technical Report No. 9303-13, IRST, Povo di Trento, Italy, March 1993.
- [68] M. Omologo and P. Svaizer, "Talker Localization and Speech Enhancement in a Noisy Environment using a Microphone Array based Acquisition System," Proc. of Eurospeech, Berlin, Germany, pp. 605-609, Sep. 1993.
- [69] M. Omologo and P. Svaizer, "Acoustic Event Localization using a Crosspower-Spectrum Phase based Technique," Proc. of ICASSP, Adelaide, Vol. 2, pp. 273-276, 1994.
- [70] M. Omologo and P. Svaizer, "Acoustic Source Location in Noisy and Reverberant Environment using CSP Analysis," Proc. of ICASSP, Atlanta, GA USA, vol. 2, pp. 921-924, 1996.
- [71] M. Omologo, M. Matassoni, P. Svaizer, and D. Giuliani, "Microphone Array Based Speech Recognition with Different Talker-Array Positions," Proc. of ICASSP, Munich, Germany, vol. 1, pp. 227-230, April 1997.
- [72] M. Omologo and P. Svaizer, "Use of the Cross-power-Spectrum Phase in Acoustic Event Location," IEEE Trans. on Speech and Audio Processing, vol. 5, no. 3, pp. 288-292, 1997.
- [73] M. Omologo, P. Svaizer, and M. Matassoni, "Environmental conditions and acoustic transduction in hands-free speech recognition," Speech Communication, vol. 25, pp. 75-95, Aug. 1998.
- [74] A.H. Quazi, "An overview on the time delay estimate in active and passive systems for target localization," IEEE Trans. on Acoustics, Speech and Signal Processing, vol. 29, no. 3, pt. 2, pp. 527-533, June 1981.
- [75] A.D. Pierce, "Acoustics - An introduction to its physical principles and applications," Acoustical Society of America, 1991.
- [76] S.U. Pillai, "Array Signal Processing," Springer-Verlag New-York Inc, 1989.
- [77] S. Prasad, M. S. Narayanan, and S. R. Desai, "Time-Delay Estimation Performance in a Scattering Medium," IEEE Trans. on Acoustics, Speech and Signal Processing, vol. 33, no. 1, pp. 50-60, Feb 1985.
- [78] D.V. Rabinkin, D. Macomber, R.J. Renomeron, and J.L. Flanagan, "Optimal Truncation Time for Matched Filter Array Processing," Proc of ICASSP, Seattle, Washington USA, vol. 6, pp. 3629-3632, May 1998.
- [79] D.V. Rabinkin, R.J. Renomeron, A. Dahl, J.C. French, J.L. Flanagan, and M.H. Bianchi, "A DSP Implementation of Source Location Using Microphone Arrays," Proc. of the SPIE, Denver, vol. 2846, pp. 88-99, Aug. 1996.
- [80] D.V. Rabinkin, R.J. Renomeron, J.C. French, and J.L. Flanagan, "Estimation of wavefront arrival delay using a cross-power spectrum phase technique," Journal of ASA, vol. 100, no. 4, Pt. 2, pp. 2697-2707, 1996.
- [81] D.V. Rabinkin, R.J. Renomeron, J.C. French, and J.L. Flanagan, "Optimum microphone placement for array sound capture," Proc. of the SPIE, vol. 3162, pp. 227-239, 1997.

- [82] D.V. Rabinkin, "Optimum sensor placement for microphone array," PhD thesis, The State University of New Jersey, New Brunswick, 1998.
- [83] F.A. Reed, P.L. Feintuch, and N.J. Bershad, "Time Delay Estimation using the LMS Adaptive Filter-Static Behaviour," IEEE Trans. on Acoustics, Speech and Signal Processing, vol. 29, no. 3, pp. 571-577, June 1981.
- [84] R.J. Renomeron, D.V. Rabinkin, J.C. French, and J.L. Flanagan, "Small-scale matched filter array processing for spatially selective sound capture," J. Acous. Soc. Am., vol. 102, no. 5 Pt. 2, pp. 3208-3218, Nov. 1997.
- [85] E.R. Robinson and A.H. Quazi, "Effect of sound-speed profile on differential time-delay estimation," J. Acoust. Soc. Am., vol. 77, no. 3, pp. 1086-1090, March 1985.
- [86] M. Rossi, "Electroacoustique," Presses Polytechniques et Universitaires Romandes ed., Lausanne, Ecole Polytechnique Fédérale de Lausanne, vol. XXI, 1986.
- [87] F. Sabot, M. Naaïm, F. Granada, E. Suriñach, P. Planet-Ladret and Furdada, "Study of the Avalanche Dynamics by means of Seismic Methods, Image Processing Techniques and Numerical Models," Annals of Glaciology, Vol. 26, 1998.
- [88] H. Saruwatari, S. Kajita, K. Takeda, and F. Itakura, "Speech enhancement using nonlinear microphone array under nonstationary noise conditions," Proc. of 6th European Conference on Speech Communication and Technology, vol.6, pp. 2567-2570, Sept. 1999.
- [89] H. Saruwatari, S. Kajita, K. Takeda and F. Itakura, "Speech enhancement using nonlinear microphone array with complementary beamforming," Proc. of ICASSP, Phoenix, Arizona USA, vol. 1, pp. 69-72, March 1999.
- [90] K. Scarbrough, N. Ahmed, and G.C. Carter, "On the simulation of a class of time delay estimation algorithms," IEEE Trans. on Acoustics, Speech and Signal Processing, vol. 29, no. 3, pp. 534-540, June 1981.
- [91] K. Scarbrough, R.J. Tremblay, and G.C. Carter, "Performance Predictions for Coherent and Incoherent Processing Techniques of Time Delay Estimation," IEEE Trans. on Acoustics, Speech and Signal Processing, vol. 31, no. 5, pp. 1191-1196, 1983.
- [92] H.F. Silverman and S.E. Kirtman, "A two-stage algorithm for determining talker location from linear microphone-array data," Computer, Speech, and Language, vol. 6, no. 2, pp. 129-152, April 1992.
- [93] H.F. Silverman, W.R. Patterson III, and J.L. Flanagan, "The huge microphone array (HMA)," LEMS Technical Report 156, LEMS, Division of Engineering, Brown University, Providence, RI 02912, Nov. 1996.
- [94] K.U. Simmer, S. Fischer, and A. Wasiljeff, "Suppression of coherent and incoherent noise using a microphone array," Annals of telecommunications, vol. 49, no. 7/8, pp. 439-446, 1994.
- [95] E. Skudrzyk, "The Foundations of Acoustics, Basic Mathematics and Basic Acoustics," Springer-Verlag New-York, 1971.
- [96] R. Smith, "Constant beamwidth receiving arrays for broad band sonar systems," Acustica, vol. 23, pp. 21-26, 1970.
- [97] R.A. Sommerfeld and H. Gubler, "Snow Avalanches and acoustic emissions", Annals of Glaciology of the International Glaciological Society, vol. 4, pp. 271-276, 1983.
- [98] R.B. Stoughton, "SAIC Sentinel acoustic counter-sniper system," SPIE, vol. 2938, no. 39, pp. 276-284, 1997.
- [99] N. Strobel and R. Rabenstein, "Classification of time delay estimates for robust speaker localization," Proc. of ICASSP, Phoenix, Arizona USA, vol. 6, pp. 3081-3084, March 1999.
- [100] N. Strobel and R. Rabenstein, "Robust Speaker Localization using a Microphone Array," Proc. European Signal Proc. Conf., Tampere, Finland, Sept. 2000.
- [101] N. Strobel, T. Meier, and R. Rabenstein, "Speaker localization using steered filtered-and-sum beamformers," Proc. Erlangen Workshop on Vision, Modeling, and Visualization, Erlangen, 1999.
- [102] D.E. Sturim, M.S. Brandstein, and H.F. Silverman, "Tracking multiple talkers using microphone array measurements," Proc. of ICASSP, Munich, Germany, vol. 1, pp. 371-375, April 1997.
- [103] P. Svaizer, M. Matassoni, and M. Omologo, "Acoustic Source Location in a Three-dimensional Space using Cross-power Spectrum Phase," Proc. of ICASSP, Munich, Germany, vol. 1, pp. 231-235, April 1997.
- [104] J.D. Sullivan, "The Comprehensive Test Ban Treaty," Physic Today, pp. 24-39, March 1998.

- [105] E. Van Lancker and M. Rossi, "*Acoustic Goniometry Antennas and Algorithms*," SSA, DAGA 98, Zurich, Switzerland, pp. 142-143, 1998.
- [106] E. Van Lancker and M. Rossi, "*Optimization of Microphone Arrays*," Proc. of the 104th Convention of AES, vol. 4693, Amsterdam, Holland, May 1998.
- [107] E. Van Lancker, "*Localization of Reflections in Auditoriums using Time Delay Estimation*," Proc. of the 108th Convention of AES, vol. 5168, Paris, France, Feb. 2000.
- [108] E. Van Lancker, "*Goniométrie acoustique et estimation des différences de temps de propagation*," Proc. of the 5th French Congress on Acoustic, Presses Polytechniques et Universitaires Romandes ed., Lausanne, Switzerland, vol. 1, pp. 603-606, Sept. 2000.
- [109] A. Swami, J.M. Mendel, and C.L. Nikias, "*Higher-Order Spectral Analysis Toolbox*," Mathworks Inc, 1998.
- [110] B.D. Van Veen and K.M. Buckley, "*Beamforming: A versatile approach to spatial filtering*," IEEE ASSP-Magazine, pp. 4-24, April 1988.
- [111] M. Wax and Y. Anu, "*Performance Analysis of the Minimum Variance Beamformer in the Presence of Steering Vector Errors*," IEEE Transactions on Signal Processing, vol. 44, no. 4, pp. 938-947, April 1996.
- [112] D.B. Ward and M.S. Brandstein, "*Grid-based beamformer design for room-environment microphone arrays*," Proc. of IEEE Workshop on Applications of Signal Processing to Audio and Acoustics, New Paltz, New York USA, pp. 23 -26, Oct. 1999.
- [113] E. Weinstein and A. J. Weiss, "*Fundamental limitations in passive time-delay estimation - Part II: Wide-band systems*," IEEE Trans. ASSP, vol. 32, no. 5, pp. 1064-1078, Dec. 1982.
- [114] J.R. Wright, "*Fundamentals of Diffraction*," J. Audio. Eng. Soc., vol. 45, no. 5, pp. 347-356, May 1997.
- [115] T. Yamada, S. Nakamura, and K. Shikano, "*Robust Speech Recognition with Speaker Localization by a Microphone Array - Performance Evaluation in Real Environments -*," Proc. of ICSLP, Philadelphia, PA USA, vol. 3, pp. 1317-1320, Oct. 1996.
- [116] Y. Yamasaki and T. Itow, "*Measurement of spatial information in sound field by closely locate four microphone method*," J. Acoust. Soc. Jpn. (E), vol. 10, pp. 101-110, 1989.
- [117] P.A. Yansouni and R.J. Inkol, "*The use of linear constraints to reduce the variance of the time of arrival difference estimates for source location*," IEEE Trans. on Acoustics, Speech and Signal Processing, vol. 32, no. 4, pp. 907-912, Aug. 1984.
- [118] D.H. Youn, S.N. Chiou, and V.J. Mathews, "*Adaptive Phase Transform Processors for Time Delay Estimation*," J. Acoust. Soc. America, vol. 80, no. 1, pp. 188-194, July 1986.

Curriculum Vitae

Van Lancker Eric

6, Grand Rue - 1268 Begnins Phone : + 41 22 366 1089 Email : eric.vanlancker@epfl.ch	Born on the 28th of January 1972 in Tournai French and Belgian Nationalities Free of military duties
--	--

Background

- 1996 – 2001: PhD on **Acoustic Goniometry** in the Laboratory of Electromagnetics and Acoustics – Swiss Federal Institute of Technology – Lausanne (CH)
- 2 – 6.1996: Dissertation on **Sensors Array Optimization** in the Laboratory of Electromagnetics and Acoustics – Swiss Federal Institute of Technology – Lausanne (CH)
- 1990 - 1996: Civil Engineering in Electricity (Automation) - Faculty Polytechnic of Mons (B).
- 1984 - 1990: Secondary studies - Collège St-Stanislas in Mons
- 1978 - 1984: Primary education - Notre-Dame de Messines in Mons

Training Periods

- Aug 1995: Training period in the Arjo Wiggins Appelton Papers firm in Nivelles on the level closed loop control of a collector.

Languages

- French: mother tongue
- English: good knowledge (linguistics stays, trips to Great-Britain and US)
- Dutch: academic knowledge

Computer Studies

Matlab, Windows, Office

Miscellaneous

- Monitor assistant ADEPS in Olympic Gymnastic
- Emergency assistance certificate Red Cross
- Driving licence B + car

Hobbies

- Olympic Gymnastic, ski, skydiving.Computers, cinema.
- Training and supervision of sports activities.

